

Charge carrier defect chemistry of nanoscopic SrTiO₃

Von der Fakultät Chemie der Universität Stuttgart
Zur Erlangung der Würde eines Doktors der
Naturwissenschaft (Dr. rer. nat.) genehmigte Abhandlung

Vorgelegt von

Piero Lupetin

aus Trieste, Italien

Hauptberichter:	Prof. Dr. Joachim Maier
Mitberichter:	Prof. Dr. Joachim Bill
Prüfungsvorsitzeder:	Prof. Dr. Emil Roduner
Tag der Einreichung:	29.03.2012
Tag der mündlichen Prüfung:	10.05.2012

Max-Planck-Institut für Festkörperforschung
Universität Stuttgart
2012

To my parents

Erklärung

Die vorliegende Doktorarbeit wurde vom Autor selbst in der Abteilung von Prof. Maier am Max-Planck-Institut für Festkörperforschung, im Zeitraum von September 2008 bis März 2012 angefertigt. Der Inhalt ist die eigene Arbeit des Autors, Ausnahmen sind gekennzeichnet, und wurde noch nicht zur Erlangung einer Qualifizierung oder eines Titels an einer akademischen Institution eingereicht.

Stuttgart, den 29 März 2012

Piero Lupetin

Declaration

The work described in this thesis was carried out by the author in the Department of Prof. Maier at the Max Planck Institute for Solid State Research from September 2008 to March 2012. The contents are the original work of the author except where indicated otherwise and have not been previously submitted for any other degree or qualification at any academic institution.

Stuttgart, 29th March 2012

Piero Lupetin

Contents

Abbreviations and symbols.....	ix
Zusammenfassung	xiii
Abstract	xvii
1. Introduction and motivation	1
1.1 Strontium titanate (SrTiO ₃) as model material.....	6
1.2 Motivation of the study	8
2. Theoretical background	11
2.1 Introduction to strontium titanate	11
2.2 Defect chemistry of SrTiO ₃	12
2.1.1 Undoped and acceptor doped SrTiO ₃	12
2.1.2 Donor doped SrTiO ₃	18
2.3 Space charge model	22
2.3.1 Gouy-Chapman profiles	23
2.3.2 Mott-Schottky profiles	25
2.4 Brick layer model	27
2.5 The conductivity minimum	29
3. Experimental methods	31
3.1 Synthesis of the nanopowders	31
3.2 Spark plasma sintering: technique and improvements	32
3.3 Characterization techniques.....	35
3.3.1 AC electrochemical impedance spectroscopy.....	35
3.3.2 X-ray diffraction (XRD).....	41
3.3.3 Electron microscopy.....	41
3.3.4 Extended X-ray Absorption Fine Structure (EXAFS)	41
3.3.5 Inductive coupled plasma - optical emission spectroscopy (ICP-OES).....	42
3.3.6 Thermogravimetical analysis (TGA)	42

4. Results and discussion	43
4.1 Synthesis and characterization of nanocrystalline SrTiO ₃	43
4.1.1 Method A: modified peroxide-based method	43
4.1.2 Method B: polymeric precursor method.....	45
4.1.3 Method C: Solvothermal method.....	47
4.1.4 Section conclusions	54
4.2 Size effects on the conductivity of undoped SrTiO ₃	55
4.3 Space charge conductivity and space charge density	63
4.4 Grain boundary defect chemistry of Fe-doped SrTiO ₃	73
4.5 Electrical conduction properties of nanocrystalline donor doped SrTiO ₃	97
Conclusions.....	107
Appendix.....	111
A.1 Effect of grain boundary decoration on the electrical conduction of nanocrystalline CeO ₂	111
A.2 Derivation of Eq. 4.10 and Eq. 4.14.....	122
References.....	123
Acknowledgements	137
Curriculum vitae	139

Abbreviations and symbols

List of abbreviations

AC	Alternating current
BLM	Brick layer model
DC	Direct current
EIS	Electrochemical impedance spectroscopy
ENC	Electroneutrality condition
EXAFS	Extended X-ray absorption fine structure
FAST	Field assisted sintering technology
GB	Grain boundary
ICP-OES	Ion coupled plasma – optical emission spectroscopy
SCL	Space charge layer
SOFC	Solid oxide fuel cell
SEM	Scanning electron microscopy
SPS	Spark plasma sintering
TEM	Transmission electron microscopy
TGA	Thermogravimetical analysis
XRD	X-ray diffraction

List of symbols

a	Unit cell parameter
A'	Acceptor according to the Kröger-Vink notation
c_j	Concentration of the defect j
C	Capacitance
C_{bulk}	Bulk capacitance
C_{GB}	Grain boundary capacitance
d_g	Average grain size
D^\bullet	Donor according to the Kröger-Vink notation
ΔE_{bulk}	Activation energy of the bulk electrical conductivity
ΔE_{GB}	Activation energy of the grain boundary electrical conductivity
ΔE_m	Activation energy of the measured electrical conductivity
e	Elementary charge
e'	Electron according to the Kröger-Vink notation
F	Faraday constant
h^\bullet	Electron hole according to the Kröger-Vink notation
$I(t)$	Alternating current
k	Boltzmann constant
m	Acceptor concentration
M	Dielectric modulus
M'	Real part of the dielectric modulus
M''	Imaginary part of the dielectric modulus
n	Electron concentration
p	Electron hole concentration
P	Oxygen partial pressure
P_{min}	Oxygen partial pressure at the conductivity minimum
$P_{min}(L \rightarrow \infty)$	Oxygen partial pressure at the minimum of the bulk conductivity
$P_{min}(L \rightarrow 0)$	Oxygen partial pressure at the minimum of the GB conductivity
Q	Constant phase element
Q_{CD}	Local charge density
R	Resistance
R_{bulk}	Bulk resistance
R_{GB}	Grain boundary resistance
T	Absolute temperature
u_n	Electron mobility
u_p	Electron hole mobility
u_v	Oxygen vacancy mobility

$U(t)$	Alternating voltage
v	Oxygen vacancy concentration
$V_O^{\bullet\bullet}$	Oxygen vacancy according to the Kröger-Vink notation
V_{Sr}^{\bullet}	Strontium vacancy according to the Kröger-Vink notation
z_j	Effective charge number of a defect j
Y	Conductance
Z	Impedance
Z'	Real part of impedance
Z''	Imaginary part of impedance
α	Fitting parameter for impedance spectra
δ	Average grain boundary thickness
ϵ_0	Vacuum dielectric constant
ϵ_r	Relative dielectric constant
ϵ_{bulk}	Bulk dielectric constant
ϵ_{GB}	Grain boundary dielectric constant
λ	Debye length
λ^*	Space charge layer width for Mott-Schottky profiles
$\tilde{\mu}$	Electrochemical potential
μ^0	Standard chemical potential
ρ	Resistivity
Σ	Surface charge density on the grain boundary core
σ	Electrical conductivity
σ_{bulk}	Bulk electrical conductivity
σ_{GB}	Grain boundary electrical conductivity
σ_{ion}	Ionic conductivity
σ_m	Measured electrical conductivity
σ_{min}	Electrical conductivity minimum
σ_n	Electron conductivity
σ_p	Electron hole conductivity
σ_{tot}	Total conductivity
τ	Relaxation time constant
τ_{bulk}	Bulk relaxation time constant
τ_{GB}	Grain boundary relaxation time constant
ϕ	Electrostatic potential
$\Delta\phi(x)$	Electrostatic potential in relation to the bulk
$\Delta\phi_0 = \Delta\phi(0)$	Space charge potential at the interface ($x = 0$)
ω	Angular frequency

Zusammenfassung

Die Untersuchung von ionischen und elektronischen Leitungseigenschaften in nanokristallinen Materialien hat in den letzten Jahren viele faszinierende Effekte hervorgebracht, die darauf beruhen, dass die Transporteigenschaften dieser Materialien von den Korngrenzen dominiert, wenn nicht sogar vollständig gesteuert, werden. Die Grundlage für das Verständnis dieser Effekte gehört zum Gebiet *Nanoionics*, das die Aufklärung der Defektchemie nicht nur für getrennte Raumladungszonen, sondern auch im besonders interessanten Fall einer mesoskopischen Situation ermöglicht, in welcher der Abstand zwischen den Grenzflächen (Korngrenzen) vergleichbar oder kleiner als die charakteristischen Abklinglängen der halbunendlichen Grenzflächen ist.

In der vorliegenden Doktorarbeit wird Strontiumtitanat (SrTiO_3) als Modellmaterial betrachtet, um diese Aspekte tiefergehend zu untersuchen. SrTiO_3 ist dank seiner ausgeprägten Stabilität und seiner ausführlich untersuchten Defektchemie auf der Makroskala ein hervorragendes Beispiel für elektrokeramische Oxide. Darüber hinaus hat dieser Perowskit eine große technische Relevanz für verschiedene Anwendungen, wie zum Beispiel als Anode für Festoxidbrennstoffzellen, als Varistor, sowie als Substrat für Hochtemperatur-Supraleiter. Im Rahmen der Festkörperionik stellt SrTiO_3 ein ideales Modell-System dar, weil drei unterschiedliche Ladungsträger, nämlich Elektronenlöcher, Sauerstoff-Leerstelle und Überschusselektronen, je nach experimentellen Bedingungen zum elektrischen Transport beitragen.

In dieser Arbeit werden die elektrischen Eigenschaften von nanokristallinem SrTiO_3 untersucht, bei welchem keine ungestörte Volumenphase vorhanden ist und der gesamte elektrische Transport ausschließlich durch die Korngrenzen dominiert wird.

Die Dotierung mit Akzeptoren (Eisen) sowie mit Donatoren (Niob) wurde verwendet, um die Eigenschaften des Materials (Leitfähigkeit und Raumladungspotenzial) auch im mesoskopischen Bereich einstellen zu können.

Um den Einfluss der Korngröße auf die Leitungseigenschaften untersuchen zu können, ist es von besonderer Bedeutung, nanostrukturierte SrTiO_3 -Keramiken mit einer durchschnittlichen Korngröße kleiner als 100 nm herstellen zu können. Dies impliziert die Optimierung des Syntheseverfahrens und des Sinterprozesses bei niedrigen Temperaturen.

Was die Synthese angeht, werden drei unterschiedliche Verfahren getestet: (i) Co-Präzipitation, (ii) Verbrennung und (iii) solvothermale Methode. Es wird beobachtet, dass Letztere die besten Ergebnisse bezüglich Reinheit, Korngröße und Partikelmorphologie liefert. Diese Methode gibt auch die Möglichkeit, das Nanopulver mit einer durchschnittlichen Korngröße von ungefähr 20 nm mit Akzeptoren und Donatoren zu dotieren.

Neben der Synthese ist auch der Verdichtungsprozess von Nanomaterialien ein wichtiges Thema. Feld aktiviertes Sintern, auch als *Spark-Plasma-Sintering* bekannt, hat sich in diesem Zusammenhang in den letzten Jahren als eine sehr wirkungsvolle Technik zur Herstellung von nanostrukturierten Keramiken erwiesen. Bemerkenswerterweise bietet das Verfahren die Möglichkeit, das Kornwachstum beim Sintern zu begrenzen; der Grund hierfür liegt in der hohen Heizrate, dem hohen Druck und der extrem kurzen Verweilzeit. In dieser Arbeit wurde das kommerzielle System so modifiziert, dass ein deutlich höherer Druck während des Sinterverfahrens ausgeübt werden kann.

Im Anschluss an die Herstellung der nanostrukturierten Keramiken ist es, die Charakterisierung der elektrischen Eigenschaften gelegt, die in Vordergrund steht.

In diesem Zusammenhang ist die Sauerstoff-Stöchiometrie der entscheidende Parameter, der bestimmt, ob das synthetisierte SrTiO_3 als p-, n- oder ionischer Leiter vorliegt. Daher wurden die Leitungseigenschaften über einen breiten Bereich von Sauerstoffpartialdrücken und Temperaturen mit Impedanzspektroskopie untersucht.

Im Falle des undotierten SrTiO_3 (gekennzeichnet durch intrinsische Akzeptor-Verunreinigungen) zeigt die Variation der Stöchiometrie in der mesoskopischen Situation, in der sich die Raumladungszonen überlappen, im Vergleich zu der makroskopischen Fall mehrere spannende größenbedingte Phänomene: die Erhöhung

der n-Typ-Leitfähigkeit um mehrere Größenordnungen, eine entsprechend große Verringerung der p-Typ-Leitfähigkeit und eine noch stärkere Absenkung der Sauerstoffleerstellen-Leitfähigkeit. Dies erzeugt eine riesige Verschiebung des Leitfähigkeitsminimums um viele Größenordnungen in Bezug auf den Sauerstoffpartialdruck. Die Ergebnisse werden im Lichte der Raumladungseffekte quantitativ als Folge einer positiven Überschussladung im Korngrenzkern interpretiert.

Eine systematische Analyse der Änderung der Korngrenzkern-Ladungsdichte als Funktion des Sauerstoffpartialdrucks zeigt, dass bei sinkendem Sauerstoffpartialdruck die Kernladung steigt. Dies kann über zusätzliche Sauerstoff-Ionen, die den Korngrenzkern verlassen, sobald die Bedingungen stärker reduzierend werden, erklärt werden.

Ein signifikanter Größeneinfluss wird auch in Akzeptor-dotiertem nanokristallinen Strontiumtitanat beobachtet. Wie erwartet, weisen die Akzeptor-dotierten Proben eine höhere elektrische Leitfähigkeit auf, die durch das höhere Dotierungsniveau erklärt werden kann. Bemerkenswerterweise erzeugt die Anwesenheit der Eisen-Dotieratome einen Abfall der Aktivierungsenergie des Korngrenzenbeitrags, was einer Verringerung des Raumladungspotentials zugeschrieben wird.

Ein weiterer Aspekt, der in dieser Arbeit verfolgt wurde, betrifft die Möglichkeit, die Transporteigenschaften der Korngrenzen gezielt einzustellen. Dieser Punkt ist besonders relevant in mesoskopischen Situationen, in denen die Korngrenzen den gesamten Ladungstransport bestimmen. Für diesen Zweck werden aliovalente Kationen direkt an den Korngrenzen eingefügt (Korngrenzen-Dekorierung), um nur lokal die Stöchiometrie zu ändern. Insbesondere kann die Dotierstoffverteilung stark die Raumladungseigenschaften und folglich den Ladungstransport beeinflussen.

Interessanterweise wird beobachtet, dass die Zugabe von Akzeptoren (Eisen) an den Korngrenzen eine Kern-Schale-Situation innerhalb des Korns generiert. Eine Analyse mit EXAFS zeigt, dass Eisen-Kationen nur partiell in die Volumenphase diffundieren, während der Rest im Kern der Korngrenzen verbleibt. Daher entsteht eine hochleitfähige Grenzfläche, die die Volumenphase kurzschließt und die Gesamtleitungseigenschaft des Materials bestimmt. Ähnliche Ergebnisse (die im Anhang näher beschrieben werden) wurden in einer entsprechenden Studie, die ein anderes ausführlich untersuchtes Oxid, nämlich Ceroxid (CeO_2), betrifft, erhalten. Die

Gegenwart von Eisen in den Korngrenzenkernen erhöht das Raumladungspotenzial der korngrenzdekorierten Probe im Vergleich zu der homogen dotierten Probe.

Besonders bemerkenswert sind die Ergebnisse bei mit Niob-dotiertem SrTiO_3 , das ein bekannter Elektronenleiter von n-Typ ist. Überraschenderweise zeigte das nanokristalline Material p-Typ-Leitfähigkeit unter oxidierenden Bedingungen (550°C) und eine Sperrwirkung der Korngrenzen unter reduzierenden Bedingungen wenn n-Leitfähigkeit überwiegt. Diese Ergebnisse weisen auf das Vorhandensein eines negativen Raumladungspotentials hin, das die Anreicherung von Löchern und die Verarmung von Elektronen in der Raumladungszone zur Folge hat.

Alle diese Ergebnisse machen nanokristallines Strontiumtitanat zu einem hervorragenden Beispiel in Bezug auf die Bedeutung der Defektchemie im mesoskopischen Bereich und demonstrieren die enorme Auswirkung der Korngröße als zusätzlichen Freiheitsgrad in der modernen Materialforschung.

Abstract

The study of ionic and electronic conduction properties of nanosized objects has revealed, in the last years, a variety of fascinating effects as the conduction properties of nanocrystalline materials are dominated if not fully controlled by the grain boundaries. The basis for the understanding of such effects is provided by the field of nanoionics, which allows the elucidation of defect chemistry not only for well separated boundary zones but also in the more exciting mesoscopic range where the distance of the interfaces (grain size) is on the order or below the characteristic decay length of a semi-infinite interface.

In the present study, strontium titanate (SrTiO_3) has been taken as a model system to investigate these aspects. Notably, SrTiO_3 is an excellent example for electroceramic oxides in general and for the family of perovskites in particular, thanks to its pronounced stability and its well studied defect chemistry at the macroscale. Furthermore, it exhibits a great technological relevance for several different applications such as anode for solid oxides fuel cells, varistors as well as substrate for high temperature superconductors. In the field of solid state ionics its importance is due to the fact that it is a mixed ionic and electronic conductor, with characteristic variations in the typical window of experimental conditions.

In this contribution the electrical properties of SrTiO_3 are investigated at the nanoscale, when no unperturbed bulk is present and the overall electrical properties are clearly dominated by the grain boundaries. Acceptor (iron) as well as donor (niobium)

doping has been used to adjust the properties of the material (conductivity, space charge potential) even in the mesoscopic regime.

In order to investigate size effects on the conduction properties the preparation of nanostructured SrTiO₃ with a grain size smaller than 100 nm comes to the fore. This implies the optimization of the synthesis procedure at low temperature as well as of the sintering process.

For the synthesis procedure three different methods are considered, namely coprecipitation, combustion and solvothermal. It is observed that the latter gives the best results in terms of purity, dimension of the grains and particle morphology. Furthermore, the solvothermal synthesis discloses the possibility of doping the nanopowders with grain size of approximately 20 nm with acceptors and donors.

The densification process is also a crucial issue in the context of nanomaterials. High pressure field assisted sintering, also known as spark plasma sintering, has recently emerged as a very powerful technique for the preparation of nanostructured oxides. Notably, it offers the possibility to limit the grain growth during the sintering procedure, thanks to the high heating rates, the high pressures and the short dwell time that can be used. In this study, a modified set up is employed in order to increase the pressure applied during the sintering and, consequently, offering the chance to decrease the holding temperature during the process.

Once the preparation of the nanostructured material is achieved, the attention is focused on the characterization of the electrical properties.

In this context, the oxygen non-stoichiometry is considered as a key element, since it plays a crucial role in determining whether SrTiO₃ is a p-type, n-type or ionic conductor. Therefore, the conduction properties have been investigated over a broad range of oxygen partial pressures and temperatures by means of impedance spectroscopy.

In the case of undoped SrTiO₃ (characterized by intrinsic acceptor impurities), the stoichiometry variation of the mesoscopic situation, in which the space charge zones overlap, reveals several exciting size-induced phenomena such as: increase of n-type conductivity by several orders of magnitude, an equally great depression of p-type conductivity and an even stronger drop of the oxygen vacancy conductivity when compared to the macroscopic situation. This generates a giant shift of the conductivity minimum by several orders of magnitude in terms of partial pressure. The results can be

explained in the light of space charge effects occurring as a consequence of a positive charge excess in the grain boundary core.

A systematic analysis of the variation of the grain boundary core charge density reveals that, irrespective of the grain size, the core charge increases while decreasing the oxygen partial pressure. This can be ascribed to oxygen ions, which leave the grain boundary core, when the conditions become more reducing, and validates the hypothesis of the presence of oxygen vacancies in the grain boundary core.

Huge size effects are observed also in intentionally acceptor doped nanocrystalline SrTiO_3 and the difference with respect to the nominally pure case can be explained by the higher doping level. In addition the presence of Fe generates a drop in the activation energy of the grain boundary contribution, which is ascribed to a reduction of the space charge potential.

Another aspect, considered in this study concerns the possibility of tuning the grain boundary properties. This point is particularly relevant in mesoscopic materials, in which the grain boundaries control the overall charge transport. This goal is achieved by adding the dopant at the grain boundaries in order to modify only locally the stoichiometry. Notably, the dopant distribution can strongly affect the space charge properties and, consequently, the charge transport in the material.

In particular, in SrTiO_3 it is observed that the addition of acceptors, namely iron at the grain boundaries yields to a core-shell situation within the grain. EXAFS analysis shows that iron partially diffuses into the bulk, whereas the rest remains inside the grain boundary core. This gives origin to a highly conductive shell, which short-circuits the bulk and determines the overall conduction properties of the material. Similar results (reported in the appendix) are obtained in a parallel study on cerium oxide (CeO_2), which another extensively studied mixed ionic and electronic oxide, namely. The presence of iron in the GB core increases the space charge potential compared to the homogeneously doped sample.

Particularly intriguing are the studies on donor (niobium) doped SrTiO_3 , which is a well known n-type conductor at relatively high temperatures in the high oxygen partial pressure range. Surprisingly, the nanocrystalline material showed p-type conductivity in oxidizing conditions at 550°C and a blocking effect of the grain boundaries with respect of the electron transport when the material switches to the n-type regime. These results can be ascribed to the presence of a negative space charge

potential, which generates the enrichment of holes and the depletion of electrons in the space charge region.

The whole set of results make nanocrystalline SrTiO₃ a formidable master example of defect chemistry in the nanocrystalline regime and demonstrate the enormous power of size as degree of freedom in modern materials research.

Introduction and motivation

Defect chemistry is the key to the understanding of the ionic and electronic transport properties of solids. The study of these aspects in nanosized objects has become crucial, since their electrical conduction properties may drastically change due to the fact that boundary properties prevail over the bulk. The basis for the understanding of such effects is provided by the field of nanoionics, which allows the elucidation of defect chemistry not only for well separated boundary zones but also in the more exciting mesoscopic range where the distance of the interfaces (grain size) is on the order or below the characteristic decay length of a semi-infinite interface.^[1-11]

Notably, in contrast with the bulk, where electroneutrality must be respected, at the interfaces a narrow charged zone, called space charge region is thermodynamically necessary. In the nanometric range, interfaces are so closely spaced that their influence on the overall properties of the material can be significant, if not predominant.^[1]

As a matter of fact, if one considers the ideal transition from a single crystal to an amorphous material while reducing the grain size (d_g), the appearance of the interfaces modifies the equilibrium situation in the material. In a single crystal (Figure 1a) the material is only composed by the bulk (represented in yellow in Figure 1). In a polycrystalline material the interfaces, namely the grain boundaries (GBs) also play a role, by influencing the charge distribution in the region close to them (pink layers in Figure 1b).

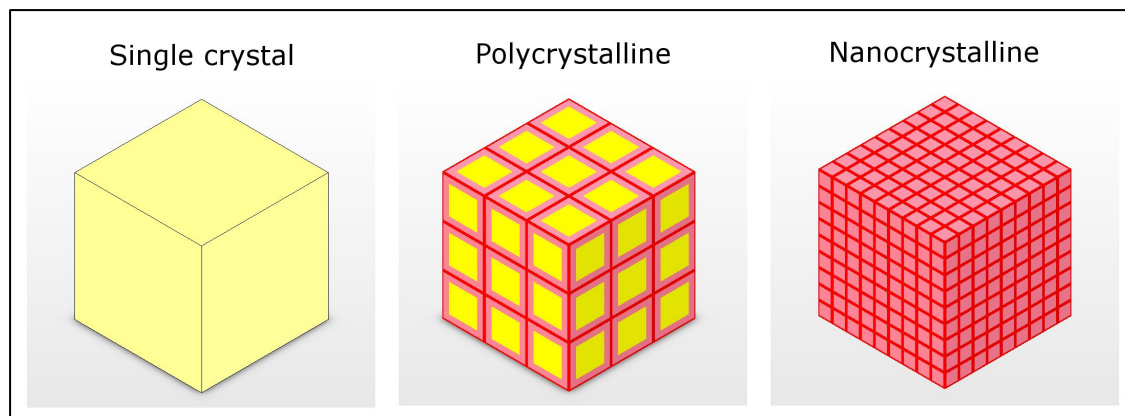


Figure 1 Schematic rendering of the ideal transition from a single crystal to a polycrystalline ensemble (differently oriented grains in contact) and to an ensemble of nano-domains. The bulk is represented in yellow, whereas pink refers to the space charge regions.

When the material is downsized to the nanoscale (Figure 1c) the GB density becomes so high that no unperturbed bulk is present any more. Consequently, in this situation the conduction properties are controlled by the interfaces. If the grain size is ideally shrunk to zero, formally only the GB core remains, ending up in an amorphous situation, due to the fact that there would be a lack of long-range order.

As electrons and ions perceive confinements with different sensitivities, particularly intriguing in this context is the investigation of mixed conducting solids, which exhibit simultaneously electronic and ionic conductivity.^[7]

Let us assume the formation of a Frenkel defect to be favourable. This consists of the transfer of the cation M^+ from the regular site to an interstitial site M'_i , leaving behind a vacancy V'_M and can be written as follows, according to the Kröger-Vink notation:^[12]



It represents an ionic excitation from the valence band to the conduction band in the energy-level diagram (which is commonly used for electrons excitations) (Figure 2a). When a homo-phase contact is created (e.g. grain boundaries), the chemical situation at the interface differs from the bulk. The main effect is a charging due to the segregation as a consequence of different structure in the interfacial core, which yields to the bending of the energy levels (Figure 2b). In this way the Fermi-levels of ions and electrons are kept constant,^[1,6,13,14] leading to predictable consequences on the ionic and electronic charge concentrations. Thus, the creation of the interface provokes an ionic charge transfer and, consequently, excess ions are

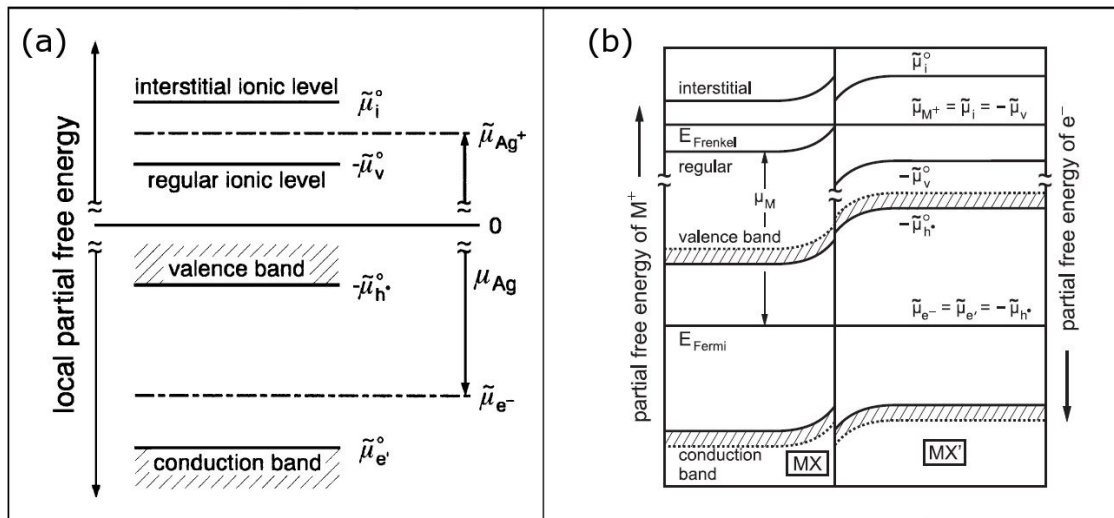


Figure 2 (a) Frenkel disorder and electron generation for a typical silver halide (reprinted from ref. [4] with permission of Elsevier); (b) Bending of energy levels at the interface between two mixed conductors (reprinted from ref. [6] with permission of Elsevier).

formed in the interface at the expense of a deficiency in the space charge zones of the phase under regard. In the case of a hetero-contact such a charge transfer can also occur from the phase under regard to the space charge zones of the neighbouring phase. A remarkable example is represented by the interface between silver halides (i.e. AgCl/AgBr systems), with a net silver ion transfer from one phase to the other.^[7,15,16]

When materials are downsized, the interfacial effect may lead to the modification of the overall electrical properties. These phenomena are known as size effects.

However, size effects may have different origins and one has to distinguish between trivial and true size effects.^[5,7,10] Trivial size effects are defined as the case in which the local interfacial situation is unchanged and the local influence is identical or comparable with the isolated interfaces. On the other hand, one refers to true size effects, when the modification of the electrical properties of materials is due to the fact that interfaces perceive each other. The size regime where this occurs is also referred as mesoscopic regime.

An example of trivial size effects is nanocrystalline undoped cerium dioxide* (CeO₂), whose bulk defect chemistry is dominated by oxygen vacancies and excess electrons. Weakly acceptor doped CeO₂ is an ionic conductor due to the fact that the oxygen vacancy concentration is much higher than the electrons one. In this system, GBs have been found to be blocking for the ion transport, since they are positively

* It is worth noting here that undoped CeO₂ is intrinsically slightly acceptor doped, since it usually contains trivalent cations as intrinsic impurities.

charged.^[17-19] It has been observed that undoped CeO₂ changes its conduction mechanism from ionic to electronic when the grain size is reduced below 30 nm.^[18,20-26] This is due to the fact that electrons are accumulated at the positively charged grain boundaries and the current finds a preferential pathway along the space charge regions generated beside them, short-circuiting the ionic bulk. At very low grain sizes (e.g. in polycrystalline thin films grown at room temperature with $d_g \sim 10$ nm) the electronic contribution can even be dominating the overall properties of heavily doped CeO₂.^[27]

On the other hand, a master example of true size effects is represented by epitaxially grown ionic heterolayers of CaF₂/BaF₂.^[28-31] Here, the ionic conductivity measured parallel to the interfaces increases with the decreasing of the layer thickness, yielding to the generation of an artificial ionic mesoscopic conductor. Notably, CaF₂ and BaF₂ are anionic conductors with F^- as mobile carriers. If the two materials are brought into contact, F^- is redistributed in the region close the interface, involving the transfer of fluoride ions from BaF₂ to CaF₂, in order to keep constant the electrochemical potential.

Consequently, fluorine interstitials (F_i') in the bulk of BaF₂ are compensated by the impurities (mainly boron). At the interface with CaF₂, due to the ion transfer across the boundary, fluoride vacancies (V_F^\bullet) are enriched, whereas F_i' are the depleted. As a consequence, to satisfy the electroneutrality on the other side of the interface, in CaF₂ F_i' are enriched, whereas V_F^\bullet are depleted. In parallel measurements, as performed by Sata *et al.*,^[28] the more conductive part, namely BaF₂, determines the conduction properties. When the layer thickness becomes comparable or even smaller than the charge screening length, the interfaces (in the vicinity of which the V_F^\bullet concentration is enriched and V_F^\bullet control the conduction) prevail and this leads to the increase of the total conductivity up to two orders of magnitude (see Figure 3a). Owing to the similar mobilities of interstitials and vacancies in BaF₂,^[28] the latter effect is due only to the V_F^\bullet accumulation at the interface. On the other hand, the more resistive CaF₂ parts of the heterostructure (and hence F_i' in CaF₂) dominate the transport perpendicular to the interfaces.^[29] These results can be explained in light of a modified Mott-Schottky approximation of the space charge model, taking into account a realistic impurity profile at the interfaces on the BaF₂ side. (Figure 3b).^[30]

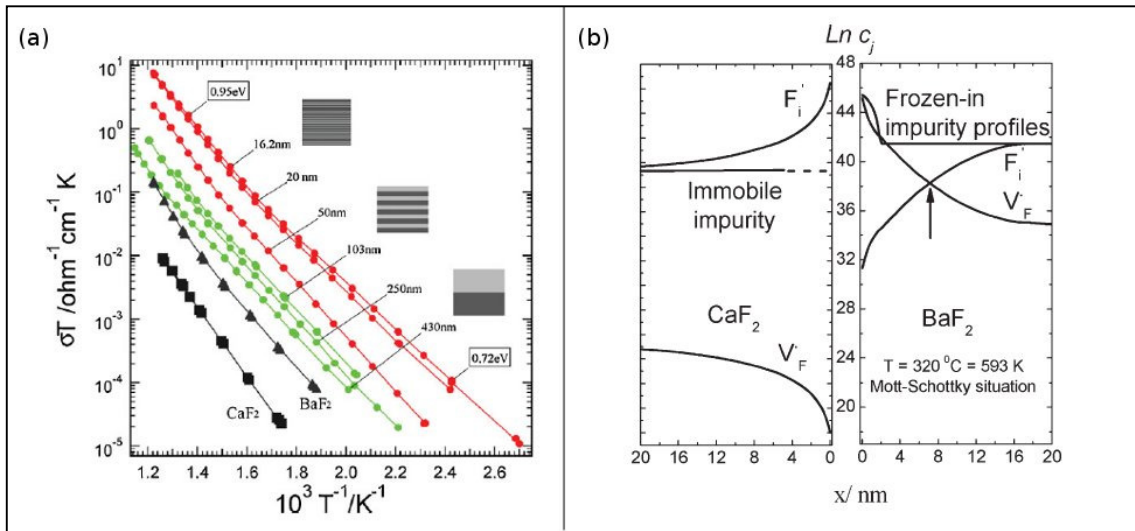


Figure 3 (a) Ionic conductivity of the $\text{CaF}_2/\text{BaF}_2$ heterostructures as a function of temperature (Reproduced from ref. [28] with permission of Nature Publishing Group). (b) Defect concentration profiles at 320°C for semi-infinite $\text{CaF}_2/\text{BaF}_2$ layers. (Reprinted from ref. [31] with permission of John Wiley & Sons, Inc..)

Such fundamental understanding of the mechanisms on the nanoscale opened new frontiers for the use of nanostructured materials in several applications. The most striking results in the field of electrochemical devices have been obtained in the context of lithium-ion batteries. A space charge storage phenomenon was observed in $\text{Li}_2\text{O}/\text{Ru}$ nanocomposites. In this system, the interfaces between lithium oxide (Li_2O) and ruthenium offer the possibility of an extra storage of Li^+ , although neither Li_2O nor Ru can store Li^+ themselves. Notably, Li_2O offers plenty of interstitial sites in which Li^+ can be accommodated but does not exhibit a redox-active element that could take up electrons. On the other hand, ruthenium has no accessible sites for the Li-ion but can absorb electrons. The combination of these two systems, e.g. when a $\text{Li}_2\text{O}/\text{Ru}$ interface is created, offers the possibility of heterogeneously storing lithium right at the interface, since Li^+ occupies interstitial sites in Li_2O close to the boundary, which are compensated by electrons sitting on the surface of metallic Ru. Therefore, if the interface density is increased by downsizing the material to the nanoscale, the excess of storage increases accordingly. This mechanism has come to the fore since it offers an excellent compromise between storage capacity and storage rate.^[32,33]

Defect engineering is also used to tailor the electrical properties of materials.^[34] In particular, when the interfaces are predominant, the modification of their properties may lead to the creation of materials characterized by a completely different behaviour

if compared to the bulk ones. It turned out, for example, that GB properties can be modified via locally decorating the GBs. This has been observed by the addition of insulating Al_2O_3 particles in AgCl. Notably, in AgCl the conductivity is low since the defect concentration is small. However, the defect mobility is significant. If artificial interfaces between the particles of AgCl and Al_2O_3 are created, the Al_2O_3 particles adsorb the mobile cation, i.e. Ag^+ , leaving cation vacancies V'_{Ag} in the AgCl matrix adjacent to the contact (space charge regions), whose ionic conductivity is then increased.^[35] Another example, which was also part of the current work and is elucidated in the appendix, focused on undoped nanocrystalline CeO_2 , whose behaviour is very well understood, as described above. In this case, the grains of the undoped powders were decorated with trivalent cations which act as acceptors with the goal of reducing their blocking effects. During the sintering at low temperatures and for short time the dopants did not have sufficient energy to diffuse completely throughout the grains, yielding to the creation of a highly doped zone close to the GBs, which acts as a preferential pathway for the ionic transport. In this way the conduction mechanism of undoped nanocrystalline CeO_2 switches from electronic to ionic.

1.1 Strontium titanate (SrTiO_3) as model material

Strontium titanate (SrTiO_3) is an excellent model material for electroceramic oxides, thanks to its pronounced chemical and thermal stability and its well explored defect chemistry. Its defect structure is similar to that of other ABO_3 perovskites (e.g. BaTiO_3), which are of high technological relevance as capacitors, positive temperature coefficient resistors and dielectrics in microelectronics devices. Thus it is used to understand these more complex systems.^[36-42]

SrTiO_3 itself finds its applications as varistor,^[43] substrate for high-temperature superconductors and anode in solid oxide fuel cells (SOFCs).^[44,45] Apart from that, it emerged also as perspective material to replace TiO_2 as photoelectrode in dye-sensitized solar cells, with the goal of increasing their efficiency.^[46,47]

Recently, SrTiO_3 has raised also interest in the field of gas sensors.^[48,49] Notably, Rothschild *et al.* observed that within 750°C and 950°C with the oxygen partial pressure ranging between 1 and 10^{-5} bar, the resistance of the solid solution $\text{SrTi}_{0.65}\text{Fe}_{0.35}\text{O}_{3-\delta}$ is independent from the temperature and it varies only with the

oxygen partial pressure.^[50] Therefore, this material is a good candidate for the development of temperature insensitive sensors,^[51,52] whose operation temperature could then be lower compared to the traditional ZrO_2 -based electrochemical sensors, decreasing in this way the power consumption and enhancing the life-time.

Strontium titanate has emerged also as excellent model material for perovskites in the field of thermoelectrics.^[53-55] As demonstrated by Poudel *et al.*^[56], size effects can play an important role also in this context and SrTiO_3 is a very interesting system to understand these aspects with a great technological potential.^[57]

In the field of solid state ionics, SrTiO_3 has raised interest due to the fact that it is a mixed conductor, which can display ionic conductivity (due to oxygen vacancies), n-type or p-type electronic conductivity depending on the temperature and oxygen partial pressure considered (see e.g. results by De Souza *et al.* in Figure 4).^[42] For this reason, it has become important for the understanding of mixed conductors and their applications, and a large number of fundamental studies have been focused on it.

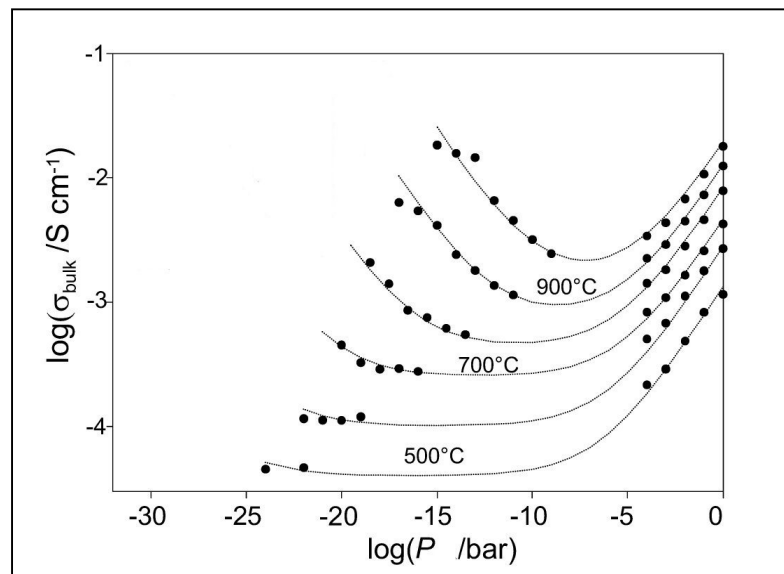


Figure 4 Bulk conductivity of a polycrystalline slightly Fe-doped SrTiO_3 sample (reproduced from ref. [42] with permission of Carl Hanser Verlag, München).

As the bulk defect chemistry of SrTiO_3 is very well known,^[36-42] this compound has been largely used to better understand the electrical conduction properties at the GBs.^[58-68] Notably, it has been demonstrated that the grain boundary core in SrTiO_3 is typically positively charged due to an excess of oxygen vacancies ($V_{\text{O}}^{\bullet\bullet}$).^[69-71] This excess is compensated by a redistribution of the charge carriers in the adjacent space

charge regions, in which positive charges, namely oxygen vacancies $V_o^{\bullet\bullet}$ and electron holes h^\bullet , are depleted, whereas electrons e' are enriched, as shown in Figure 5.^[4,58,60,65,66,68,72] For this reason, the ion transport (i.e. oxygen vacancies) is severely blocked at the GBs.

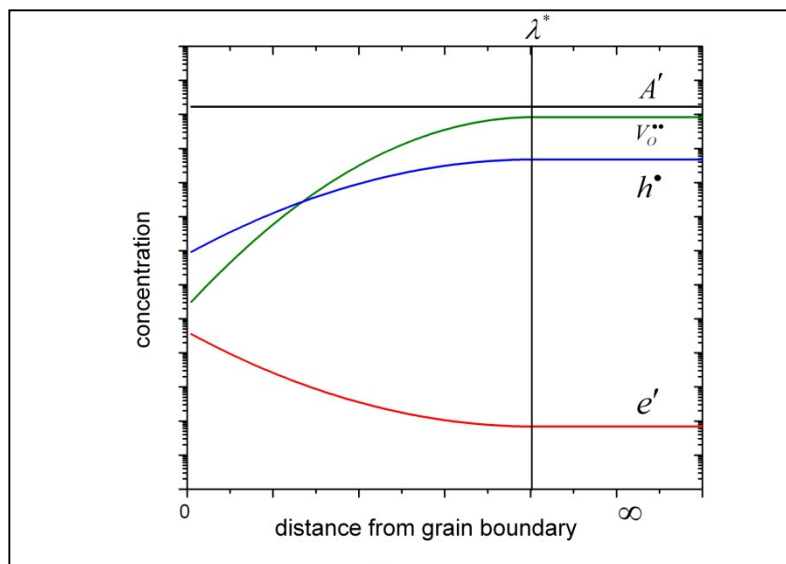


Figure 5 Concentration profiles (Mott–Schottky approximation) near a grain boundary valid for a variety of acceptor doped oxides, including SrTiO_3 , at sufficiently low temperatures.^[3] λ^* is the space charge layer width and defines the distance until which the charge carriers feel the influence of the GB core charge.

In SrTiO_3 the space charge region is relatively large compared to other mixed conductors (e.g. CeO_2), in light of the fact that the dielectric constant is high, corresponding to a small charge screening. As a consequence, in undoped SrTiO_3 the overlapping of the space charge regions (mesoscopic regime) appears when the grain size is reduced below 100 nm (depending on the doping content), making it the oxide counterpart of the $\text{CaF}_2/\text{BaF}_2$ heterostructures described above. This was first experimentally observed by Balaya *et al.*^[73-75]

1.2 Motivation of the study

The goal of this study is to deeply understand the GB electrical properties in terms of defect chemistry, with particular interest to the mesoscopic regime, in the occurrence of which a modification of the overall electrical properties takes place. Strontium titanate is taken as model system for the reasons described above and the grain size is reduced to the nanoscale, in order to make interfaces predominant.

In addition, this system offers the possibility of studying for the first time the dependence of the space charge chemistry as a function of the oxygen partial pressure. This study is a continuity of the variation of Ag-potential (Cl_2 -partial pressure) in the $\text{AgCl}:\text{Al}_2\text{O}_3$ system,^[76] but even allows us the verification of the Kröger-Vink diagrams in the mesoscopic situation.

The work involves the preparation of the nanostructured SrTiO_3 , including the synthesis of the nanopowders (undoped, acceptor and donor doped) and their sintering. In particular, the synthesis is a crucial part of this work, since the preparation of nanocrystalline SrTiO_3 is fundamental for the investigation of the properties in the mesoscopic regime. Three methods reported in literature have been reproduced and improved, in order to prepare powders with the smallest possible grain size. Particular attention is given to the aspects of the sample preparation with an effect on the final electrical properties (e.g. grain size, purity, etc.).

A further intriguing challenge consists in the possibility of modifying the GB properties of mixed conductors with the final goal of obtaining an enhancement of the ionic conductivity (beyond that one would be rewarded by a lower electronic contribution).

As explained in this chapter, heterogeneous doping is a powerful method for modifying the electrochemical properties of the materials and doping with acceptors at the GBs is chosen as a possible method in order to locally tailor the GB properties and to reduce their blocking effect. This approach has been used not only for SrTiO_3 , which is the main topic of this study, but also for CeO_2 , a material in which the increase of the ionic conductivity would have a huge impact from the application point of view. The results regarding CeO_2 are reported in the appendix of this work.

The electrical conduction properties of nanocrystalline SrTiO_3 are characterized by means of impedance spectroscopy and discussed in view of the macroscopic properties of the system. The results are explained in view of the space charge model.

Theoretical background

2.1 Introduction to strontium titanate

Strontium titanate is characterized by a perovskite structure of the type ABO_3 , which is illustrated in Figure 6. The Sr^{2+} and O^{2-} ions combine to form a close-packed cubic structure, with the smaller, more highly charged Ti^{4+} ions in octahedral interstices. Each O^{2-} is surrounded by four Sr^{2+} and eight O^{2-} , whereas each Sr^{2+} is surrounded by twelve O^{2-} . In the centre of the face centred cubic unit cell the small Ti^{4+} is octahedrally coordinated to six O^{2-} .^[77]

The peculiarity of $SrTiO_3$ consists in the symmetry of the unit cell in the three directions, giving rise to a cubic cell, whose parameter a is equal to 3.9056 \AA .^[78-80] This characteristic, together with the chemical stability, makes $SrTiO_3$ a material of great technological interest, since it is an elegant model for the whole family of perovskites, which includes $CaTiO_3$, $BaTiO_3$, $PbTiO_3$ and $PbZrO_3$. The theoretical density of synthetic $SrTiO_3$ is equal to 5.13 g/cm^3 .

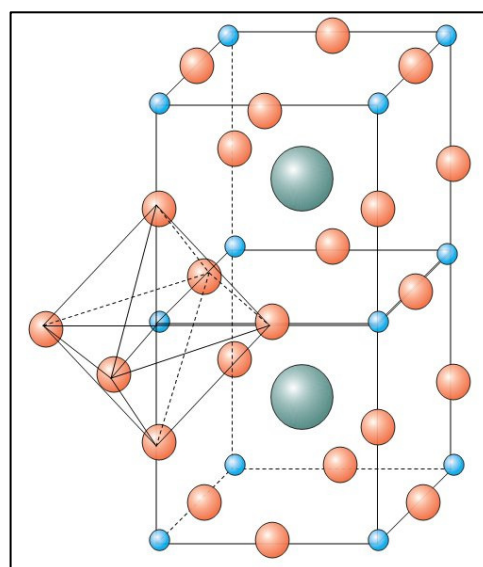


Figure 6 Perovskite structure of $SrTiO_3$. The colors of the spheres are assigned as follows: (red) oxygen; (green) A-site = strontium; (blue) B-site = titanium.

Doping can be used to modify the electrical properties of the material. Depending on their valence and ionic radii, dopants behave in different ways, yielding different final conditions. As dopants, lanthanum, niobium and iron have been chosen in this work. Fe^{3+} substitutes for Ti^{4+} and acts as acceptor^[39,42], whereas La^{3+} and Nb^{5+} behave as donors, since La^{3+} occupies the Sr^{2+} site^[81] and Nb^{5+} the Ti^{4+} site.^[82] The different behaviour of the cations is due to their ionic radii which are reported Table I according to ref. [83].

Table I Crystal and ionic radii of Sr, Ti and the most common dopants for SrTiO_3 according to ref. [83].

Ion	Coordination	Crystal radius [Å]	Ionic radius [Å]
Sr^{2+}	XII	1.58	1.44
Ti^{4+}	VI	0.75	0.61
La^{3+}	XII	1.50	1.36
Fe^{3+}	VI	Low spin	0.69
		High spin	0.79
Nb^{5+}	VI	0.78	0.64

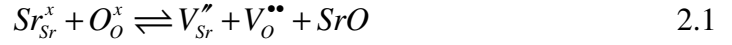
2.2 Defect chemistry of SrTiO_3

The interest for the electrical properties of titanates with perovskite structure (i.e. BaTiO_3 and SrTiO_3) has risen since the Seventies and a very reliable and well established model has been developed to describe their defect chemistry in details.^[36,37,39,41,59,72,82,84-91] In this chapter, the defect reactions which dominate the electrical conduction properties of undoped, acceptor and donor doped SrTiO_3 will be elucidated using the Kröger-Vink notation.^[12] As nominally undoped SrTiO_3 turns out to be almost always slightly acceptor doped, these two cases will be discussed together.

2.1.1 Undoped and acceptor doped SrTiO_3

Considerations on the perovskite structure suggest that the dominant ionic point defects in the bulk are vacancies rather than interstitials and Sr vacancies (V_{Sr}'') are compensated by oxygen vacancies ($V_{\text{O}}^{\bullet\bullet}$).

Indeed, the partial Schottky disorder reaction,



is found to be more favourable than the other Schottky disorder reactions and than all Frenkel disorder reactions.^[41,68]

Equation 2.1 results in a simplified mass action law, where the SrO concentration ($[SrO]$) is assumed to be constant:

$$K_S(T) = [V_{Sr}''] [V_O^{\bullet\bullet}] = K_S^0(T) \exp\left(-\frac{E_S}{kT}\right). \quad 2.2$$

The other intrinsic defect reaction of importance is the generation of electrons and holes by thermal excitation across the band gap (*band-band transfer*):

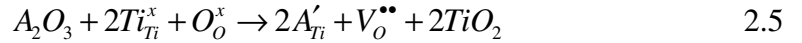


The corresponding mass action equation is given by

$$K_B = n \cdot p = K_B^0 \exp\left(-\frac{E_B - \beta_B T}{kT}\right) \quad 2.4$$

being n and p respectively the electron and hole concentration.

The incorporation of a trivalent acceptor A' in the Ti site and the subsequent formation of oxygen vacancies in $SrTiO_3$ can be described by the following reaction:^[92]

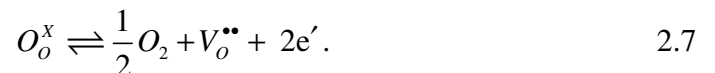


For undoped and acceptor doped $SrTiO_3$ below 1000°C the simplified expression for electroneutrality is:^[36]

$$2v + p = m + n \quad 2.6$$

being $m = [A'_{Ti}]$ and v the oxygen vacancy concentration.

The concentration of point defects is also highly dependent on the equilibrium with the surrounding atmosphere, i.e. with gaseous oxygen. Notably, at very low P the predominant mechanism is the loss of oxygen from the lattice to the atmosphere, which is determined by the reaction:



In this case the mass action law is given by:

$$K_{Red}(T) = v n^2 P^{1/2} = K_{Red}^0 \exp\left(-\frac{\Delta H_{Red}}{kT}\right). \quad 2.8$$

In this regime, the condition of electroneutrality can be simplified as:

$$n \approx 2\nu \quad 2.9$$

yielding

$$n = (2K_{Red}(T))^{1/3} \cdot P^{-1/6}. \quad 2.10$$

This means that if one plots n versus P in logarithmic scale, a straight line with slope equal to $-1/6$ is obtained. However, this regime appears at $P < 10^{-40}$ bar at 550°C (for 0.01at% impurities). For this reason, it does not appear in the Kröger-Vink diagram in Figure 7a and is not observed in the typical experimental conditions.

At higher P , the acceptors are compensated by oxygen vacancies and the electroneutrality requirement becomes:

$$2\nu \approx m. \quad 2.11$$

Now, by combining Eq.s 2.8 and 2.11,

$$n = \left(\frac{2K_{Red}(T)}{m} \right)^{1/2} \cdot P^{-1/4} \quad 2.12$$

results. It is represented by the black straight line with slope $-1/4$ in the defect diagram in Figure 7a.

Under oxidizing conditions, the stoichiometric excess of oxygen is compensated by the extrinsic $V_o^{\bullet\bullet}$ present because of a net excess of acceptor impurities (*oxygen incorporation reaction*):



The corresponding mass action law is:

$$K_{ox}(T) = \frac{p^2}{\nu \cdot P^{1/2}} = K_{ox}^0 \exp\left(-\frac{E_{ox}}{kT}\right) \quad 2.14$$

Knowing that ν is fixed by the impurity/acceptor content m , according to the electroneutrality condition $2\nu \approx m$,

$$p = \left(\frac{K_{ox}(T) \cdot m}{2} \right)^{1/2} \cdot P^{1/4} \quad 2.15$$

is obtained and it results in the green straight line of the Kröger-Vink diagram in Figure 7a.

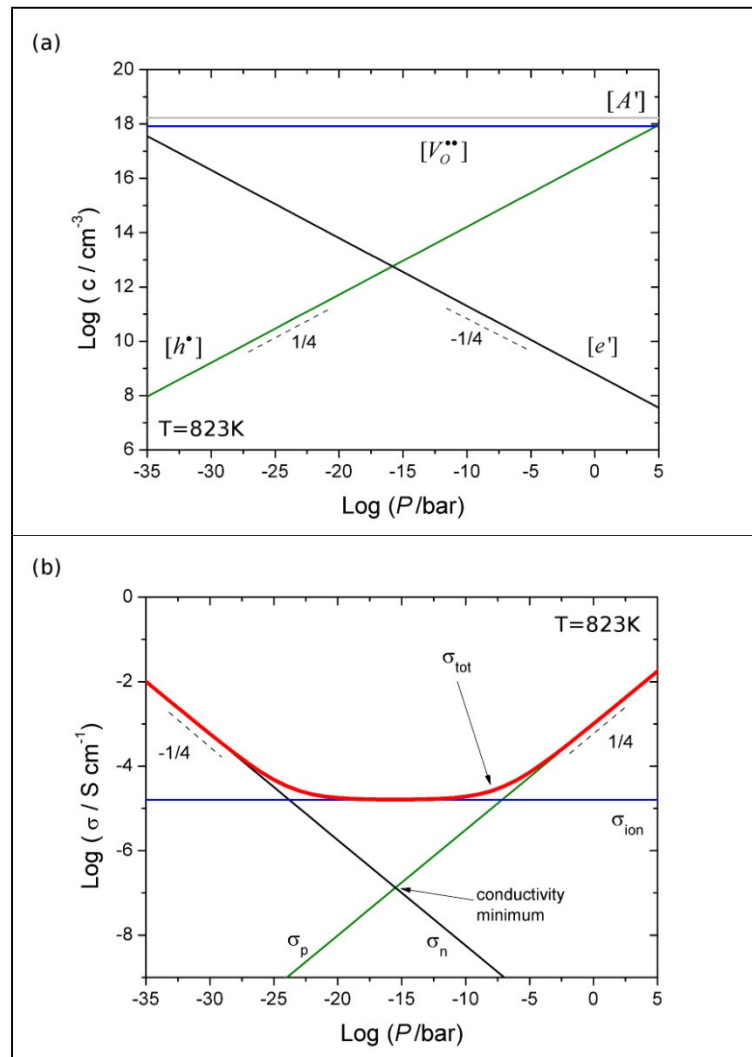


Figure 7 (a) Kröger-Vink diagram and (b) P -dependence of the electrical conductivity calculated for SrTiO₃ with 0.01at% acceptor impurities at 550°C according to the defect chemistry model reported in ref. [39]. In (b) the red line represents the total conductivity according to Eq. 2.20. Please note that in this case the acceptor species is not redox active.

If the acceptors or impurities are redox active species, the ionization reaction of such dopants must also be taken into account. This is, for example, the case of Fe, which is a widely used acceptor and a typical residual impurity in undoped SrTiO₃, and exhibits a mixture of oxidation states of +III and +IV. [39,93-97] It is worth noting here that, even though Fe⁴⁺ is rather unusual in aqueous chemistry, it occupies a site tailored for the Ti⁴⁺ cation in the SrTiO₃ lattice; this substitutional defect is denoted as Fe_{Ti}^x . [96]

The defect chemistry reaction related to the valence change of the Fe cation can be written as ^[39]



with the mass action

$$K_{Fe} = \frac{[Fe'_{Ti}] \cdot p}{[Fe^x_{Ti}]} = K_{Fe}^0 \exp\left(-\frac{E_{Fe} - \beta_{Fe} T}{kT}\right). \quad 2.17$$

The net sum of ionized and neutral acceptors is fixed by the initial doping content and must remain constant:

$$[A] = [A^x] + [A']. \quad 2.18$$

The mass action parameters used in this work for Eq.s 2.4, 2.14, 2.17 were taken from the defect chemistry model reported in ref. [39] and are listed in Table II.

Table II Mass action parameters for Eq.s 2.2 and 2.8 from ref. [41] and for Eq.s 2.4, 2.14, 2.17 from ref. [39].

Equation		K_i^0	E_i	β_i
Schottky defect formation	2.2	$3 \cdot 10^{44} \text{ cm}^{-6}$	2.5 eV	
Band-band transfer	2.4	$7.67 \cdot 10^{42} \text{ cm}^{-6}$	3.30 eV	$6.0 \cdot 10^{-4} \text{ eV / K}$
Reduction reaction	2.8	$5 \cdot 10^{71} \text{ cm}^{-9} \cdot \text{bar}^{1/2}$	6.1 eV	
Oxygen incorporation	2.14	$1.02 \cdot 10^{23} \text{ Pa}^{-1/2} \cdot \text{cm}^{-3}$	1.63 eV	
Fe ionization	2.17	$2.77 \cdot 10^{21} \text{ cm}^{-3}$	1.18 eV	$3.7 \cdot 10^{-4} \text{ eV / K}$

In the temperature regime considered in this work (400-700°C) the dominant charge carriers in SrTiO₃ are electrons e' , electron holes h^{\bullet} and oxygen vacancies $V_o^{\bullet\bullet}$, since the other defects, namely strontium and titanium vacancies can be considered immobile and they do not contribute to the electrical conduction.^[98]

The defect chemistry model elucidates the impact of the change of stoichiometry on the charge carrier concentrations c_j in the material and it is applicable

over a wide range of P and dopant concentration. However, in order to predict the electrical conductivity ($\sigma_j = z_j e c_j u_j(T)$), also the mobilities $u_j(T)$ of the charge carriers have to be taken into account.

Notably, the electrical conductivity in a solid is simply the sum of the partial conductivities σ_j associated with each type of charge carrier j and it is given by: ^[99]

$$\sigma = \sum_j \sigma_j. \quad 2.19$$

It turns out that the total conductivity σ_{tot} of acceptor doped SrTiO₃ is a function of P and T and can be expressed as follows:

$$\sigma_{tot}(P, T) = 2 \cdot e \cdot v(P, T) \cdot u_v(T) + e \cdot n(P, T) \cdot u_n(T) + e \cdot p(P, T) \cdot u_p(T). \quad 2.20$$

The mobilities $u_j(T)$ of the charge carriers used in this work were taken from the well established defect chemistry model and are calculated according to ref. [39]:

$$\begin{aligned} u_p(T) &= 8.9 \cdot 10^5 (T / K)^{-2.36} \text{ cm}^2 \cdot \text{V}^{-1} \cdot \text{s}^{-1} \\ u_n(T) &= 4.5 \cdot 10^5 (T / K)^{-2.2} \text{ cm}^2 \cdot \text{V}^{-1} \cdot \text{s}^{-1} \\ u_v(T) &= 1 \cdot 10^4 \text{ cm}^2 \cdot \text{V}^{-1} \cdot \text{s}^{-1} (T^{-1} / K)^{-2.2} \exp\left(-\frac{0.86 \text{ eV}}{kT}\right). \end{aligned} \quad 2.21$$

It is worth noting here that, at high P , the conduction is dominated by holes (*p-type regime*), although their concentration is lower than v . This is due to the fact that at 550°C u_p is almost four orders of magnitude higher than u_v , according to Eq. 2.21. In this regime ($P > 10^{-5} \text{ bar}$), the P -dependence of the total conductivity (red line in Figure 7b) follows from Eq.s 2.15 and 2.20 and it is equal to $1/4$ in the logarithmic plot as illustrated in Figure 7b (right hand side).

In the nominally undoped and acceptor doped SrTiO₃ σ_{tot} is constant in the middle P -range, because σ_{ion} becomes predominant (plateau region in Figure 7b). The conductivity is thus ionic and it is equal to $\sigma_{ion} = 2e\mu_v v$, since $v = m/2$ is fixed by the acceptor content. From the experimental value of σ_{ion} , it is also possible to determine either the acceptor content using the mobility in Eq. 2.21 or the $V_o^{\bullet\bullet}$ mobility knowing the exact acceptor concentration.

At low P , the conductivity of SrTiO₃ becomes n-type with a slope $-1/4$ (Eq. 2.12), as the electron concentration increases according to the band-band transfer and their mobility is orders of magnitude higher than the one of oxygen vacancies.

If one considers only the intrinsic electronic conductivity, there is a certain P value at which a transition from p- to n-type conductivity takes place (Figure 7b). At this point the overall electronic conductivity is at minimum. This transition point is particularly significant because it allows extracting important pieces of information regarding the conduction properties of this compound. These aspects will be discussed in detail in a following section of this chapter.

2.1.2 Donor doped SrTiO₃

The defect chemistry of donor doped SrTiO₃ has been also extensively studied.^[41,81,82,100-102] Surprisingly, the defect chemistry has been investigated only at high temperatures ($T > 1000$ K) and a model for low T is clearly missing. In the following, the main concepts are summarized and the corresponding Kröger-Vink diagrams according to ref. [41] are shown in Figure 8.

It is worth noting that here the concentration of donors is fixed by the initial composition and is assumed to remain constant in the investigated temperature and P range, as in ref. [41].

From this assumption, the following simplified electroneutrality condition results, which takes into account only the major charged defect species:

$$n + 2[V_{Sr}^{\prime\prime}] = 2v + [D^{\bullet}]. \quad 2.22$$

At low values of P , the reduction reaction (Eq. 2.7) is predominant as in the case of acceptor doping and leads to the formation of oxygen vacancies. Therefore the total electronic charge carrier density does not only depend on the donor content $[D^{\bullet}]$, but also on the concentration of the oxygen vacancies:

$$n = 2v + [D^{\bullet}]. \quad 2.23$$

At very low P it is reasonable to assume that $v \gg [D^{\bullet}]$ and the electroneutrality condition simplifies to:

$$n \approx 2v \quad 2.24$$

meaning that the oxygen vacancies are compensated by conduction electrons.

Combining Eq.s 2.8 and 2.24, one obtains:

$$n = (2K_{red}(T))^{1/3} \cdot P^{-1/6}. \quad 2.25$$

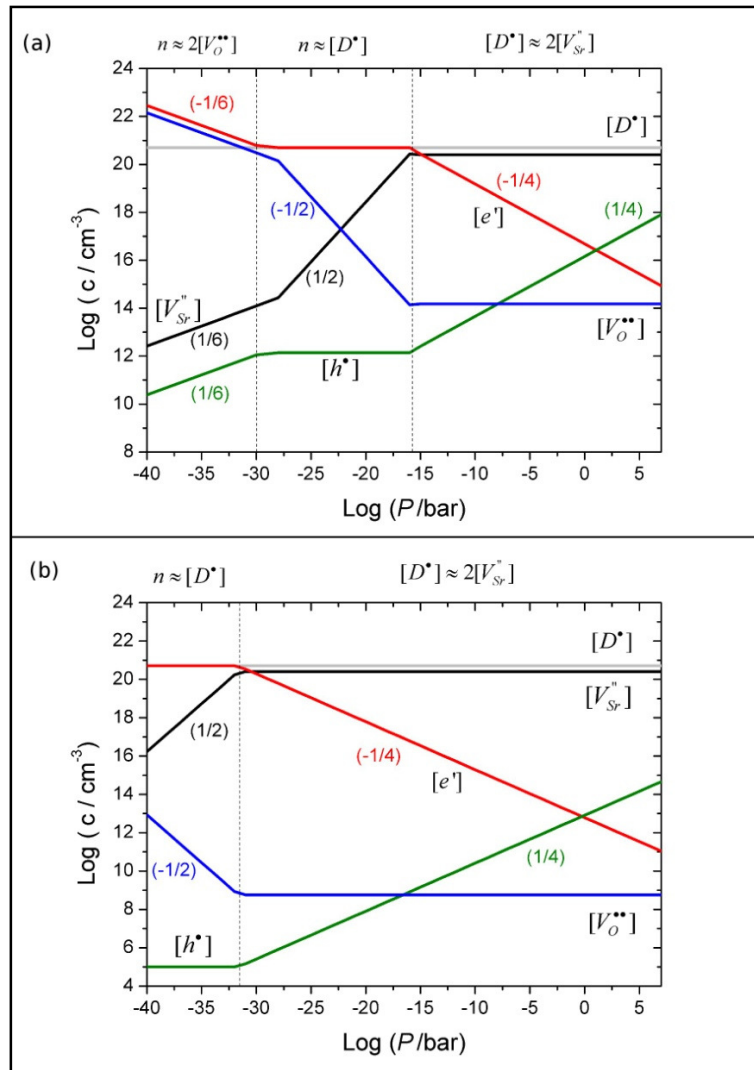


Figure 8 Calculated Kröger-Vink diagram for 3at% donor doped SrTiO₃ at (a) 1000°C and (b) at 550°C K, according to the defect chemistry model reported in ref. [41].

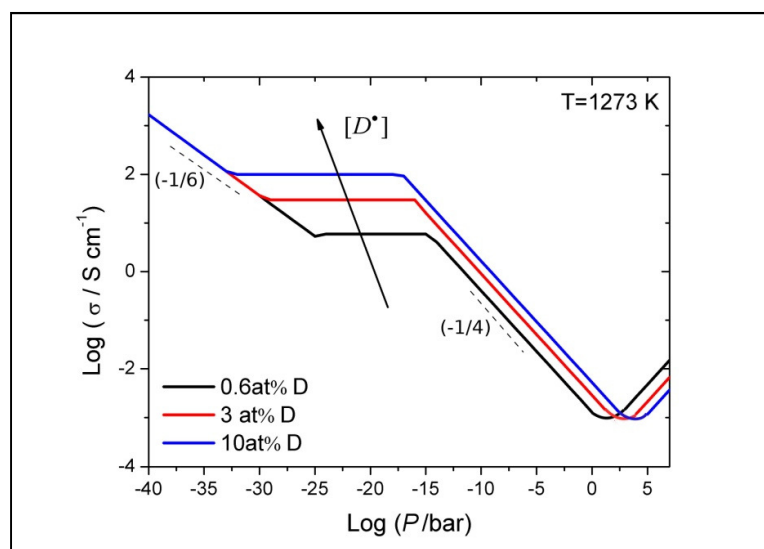


Figure 9 P-dependence of the theoretical conductivity of donor doped SrTiO₃ at 1000°C for different donor concentrations, according to ref. [41].

In intermediate P -range, the oxygen vacancy concentration has become small in comparison to the donor content ($v \ll [D^\bullet]$). The electroneutrality is, therefore, given by:

$$n \approx [D^\bullet]. \quad 2.26$$

This means that the electron concentration depends only on the donor content, which is fixed by the initial concentration and, therefore, it does not vary with P .

At high P , there is a further change in the defect structure of donor doped SrTiO₃. In this regime, intrinsic acceptors in the form of strontium vacancies compensate the donors. This means that the material switches from an electronic to an ionic compensation mechanism. The electroneutrality can be simplified as

$$[D^\bullet] \approx 2[V_{Sr}'''] \quad 2.27$$

which in combination with Eq.s 2.2, 2.8 results in

$$n = \left(K_{Red}(T) \cdot [D^\bullet] / (2K_S(T)) \right)^{1/2} \cdot P^{-1/4}. \quad 2.28$$

At even higher P , when according to Eq. 2.7 the electron concentration becomes lower than the hole contribution and the intrinsic electronic conductivity switches from n-type to p-type. Taking into account the band-band transfer (Eq. 2.4) and combining it with Eq. 2.28, one could predict the relationship:

$$p \propto P^{1/4}. \quad 2.29$$

The related defect diagram has been represented in Figure 8a for 3at% donor doped SrTiO₃ at 1000°C, temperature around which it was determined by Moos.^[41] The defect diagram has been determined also at 550°C (Figure 8b), the temperature at which the experiments in this work have been carried out. However, it has to be borne in mind that at low temperatures V_{Sr}''' may become immobile. This implies that the defect model proposed by Moos might not be practical anymore.^[103]

It has been observed that electrons and holes are the dominant charge carriers, since the concentration of $V_O^{\bullet\bullet}$ and the mobilities of D^\bullet and V_{Sr}''' are much lower. After these considerations, Eq. 2.20 can be rewritten as:

$$\sigma_{tot}(P, T) = e \cdot n(P, T) \cdot u_n(T) + e \cdot p(P, T) \cdot u_p(T). \quad 2.30$$

The theoretical total conductivity is represented in Figure 9 for different donor contents at 1000°C as a function of P . The material is expected to be n-type with a slope of $-1/6$ in strongly reducing atmospheres, in agreement with Eq. 2.25 (intrinsic

regime). In the middle range of P , in which the electron concentration is fixed by the donor content (Eq. 2.26), σ_{tot} is constant, giving rise to the plateau region of Figure 9. In this regime, the conductivity can be rewritten as:

$$\sigma_n(T) = e \cdot [D^\bullet] \cdot u_n(T). \quad 2.31$$

As the donor content is constant, from the value of σ_n in the plateau region one can determine the value of the mobility directly from the conductivity data.

Under oxidizing conditions, the conductivity is proportional to $P^{-1/4}$. Notably, the conductivity minimum is expected at $P > 1 \text{ bar}$ even for very low donor contents and, for this reason, it is normally not observed in the typical experimental conditions.

It is worth noting here that on increasing the donor content the conductivity minimum shifts towards higher values of P , the n-type conductivity increases, the p-type conductivity decreases and the plateau region becomes wider. In contrast to this, the intrinsic conductivity at low P is independent of the donor content.

If one carefully inspects the expressions of the electron mobilities reported in literature, it turns out that there is a discrepancy between the expression proposed by Denk *et al.*^[39] for acceptor doped SrTiO₃ and reported in Eq. 2.21 and the one proposed by Moos *et al.*^[41] for donor doped SrTiO₃, which is given by:

$$u_n(T) = 3.95 \cdot 10^4 (T / K)^{-1.62} \text{ cm}^2 \cdot \text{V}^{-1} \cdot \text{s}^{-1} \quad 2.32$$

It is worth noting here that the latter has been determined in the temperature range between 1000 and 1400°C. Therefore, it has been decided in this study to use the mobility defined by Eq. 2.21 for acceptor doped SrTiO₃ also for the donor doped material, since it seems to be more precise in the temperature range considered (550-450°C).

2.3 Space charge model

The defect chemistry models elucidated in the previous sessions are valid for the bulk of the material in equilibrium conditions. Notably, at the GBs, which, from a microstructural point of view, are crystallographic mismatch zones, the electrochemical situation is different compared to the bulk and the electrical properties may vary significantly in the regions close to the GBs (space charge layers). While in the bulk the electroneutrality condition gives a sufficient account of electrostatic, at the boundaries it has to be replaced by the more general Poisson's equation:^[1,6,62,104-107]

$$\nabla^2 \phi = -\frac{Q_{CD}}{\varepsilon_0 \varepsilon_r} \quad 2.33$$

being ϕ the electrostatic potential, Q_{CD} the local charge density, ε_0 the vacuum dielectric constant and ε_r the specific dielectric constant of the material.

The GB effects in SrTiO₃ can be explained according to the space charge model as described in the following.^[15] As the grain boundary core in SrTiO₃ is positively charged due to an excess of oxygen vacancies $V_O^{\bullet\bullet}$,^[69,70] the charge carriers are redistributed in the adjacent space charge regions.^[4,58,60,65,66,68,72,105] It is worth noting here that the concept of "crystallographic GB" is different from the "electrical GB". The "crystallographic GB" refers to the perfect structure, while the "electrical GB" includes the point defect structure in the surroundings. Hence, the latter consists of a GB core and two adjacent space charge regions.

The electrochemical potential $\tilde{\mu}$ of any mobile defect species j with an effective charge z_j in the position x is given by:^[1,4,6,13]

$$\tilde{\mu}_j(x) = \mu_j^0 + kT \ln c_j(x) + z_j e \phi(x) \quad 2.34$$

where $c_j(x)$ is the defect concentration in x , $\phi(x)$ the electrostatic potential and μ_j^0 the standard chemical potential. In equilibrium, $\tilde{\mu}_j(x)$ is equal to the electrochemical potential in the bulk ($\tilde{\mu}_j(x = \infty)$) and, consequently, the concentration profiles $c_j(x)$ in the space charge layer are described by the following law:^[1]

$$\frac{c_j(x)}{c_{j\infty}} = \exp\left(-\frac{z_j e (\phi(x) - \phi_\infty)}{kT}\right) \quad 2.35$$

* The segregation of interstitial cations can also be hypothesized as cause of the positive GB core.^[108-109]

where $c_{j\infty}$ and ϕ_∞ are respectively the concentration in the bulk of the defect j and the electrostatic potential in the bulk.

In Eq. 2.35 $\phi(x) - \phi_\infty = \Delta\phi(x)$ is the electrostatic potential in relation to the bulk, which can be determined by solving the Poisson's equation.

The combination of Eq. 2.35 and of the Poisson's equation 2.33 leads to the Poisson-Boltzmann differential equation: ^[18,107]

$$\frac{\partial^2 \phi(x)}{\partial x^2} = - \frac{\sum_j z_j e c_{j\infty}}{\epsilon_0 \epsilon_r} \exp\left(-\frac{z_j e}{kT} \Delta\phi(x)\right). \quad 2.36$$

The Gouy-Chapman and the Mott-Schottky approximations of Eq. 2.36 emerged as very powerful models for the description of the behaviour of the charge carriers at the interfaces in solids. The main difference between these two models is that in the former the dopant ions are mobile within the field, whereas in the latter they are assumed to be frozen and they remain spatially independent. In other words, in Eq. 2.36 j refers to all defects including the dopants/impurities in the case of Gouy-Chapman profiles and to the native defects only for the Mott-Schottky profiles, in which the dopant profile is considered to be flat. In the next subsections, they will be elucidated in detail.

2.3.1 Gouy-Chapman profiles

The Gouy-Chapman model is applied when the dopant cations are sufficiently mobile to contribute to the compensation of the core charge and they can be redistributed in the space charge region.

Solving Eq. 2.36 by applying the appropriate semi-infinite boundary conditions and using a reference point for the potential, commonly set as 0 in the bulk, the spatial variations of the electrostatic potential which specifies the redistribution of all charged defects can be written:

$$\phi(x) = \frac{2kT}{z_j e} \ln\left(\frac{1 + \Theta \exp(-x/\lambda)}{1 - \Theta \exp(-x/\lambda)}\right) \quad 2.37$$

being λ the Debye length defined as

$$\lambda = \sqrt{\frac{\epsilon_0 \epsilon_r kT}{2z_j^2 e^2 c_{j\infty}}} \quad 2.38$$

and Θ the profile parameter

$$\Theta = \tanh\left(\frac{z_j e \Delta \phi_0}{4kT}\right). \quad 2.39$$

The term Θ represents the “degree of influence” of the contact under consideration.^[104] It becomes zero if the boundary layer does not deviate from the bulk ($c_{j0} = c_{j\infty}$). On the other hand it approaches +1 for maximum enrichment ($c_{j0} \gg c_{j\infty}$) and -1 for maximum depletion effect ($c_{j0} \ll c_{j\infty}$).^[26]

Finally, by combining Eq.s 2.35 and 2.37 the Gouy-Chapman profiles in the space charge region (as represented with the blue dotted line in Figure 10), are obtained.^[18,104,107]

$$\frac{c_j(x)}{c_{j\infty}} = \left(\frac{1 + \Theta \exp(-x/\lambda)}{1 - \Theta \exp(-x/\lambda)}\right)^{2z_j}. \quad 2.40$$

According to the Gouy-Chapman model, the space charge region width is approximately 2λ .

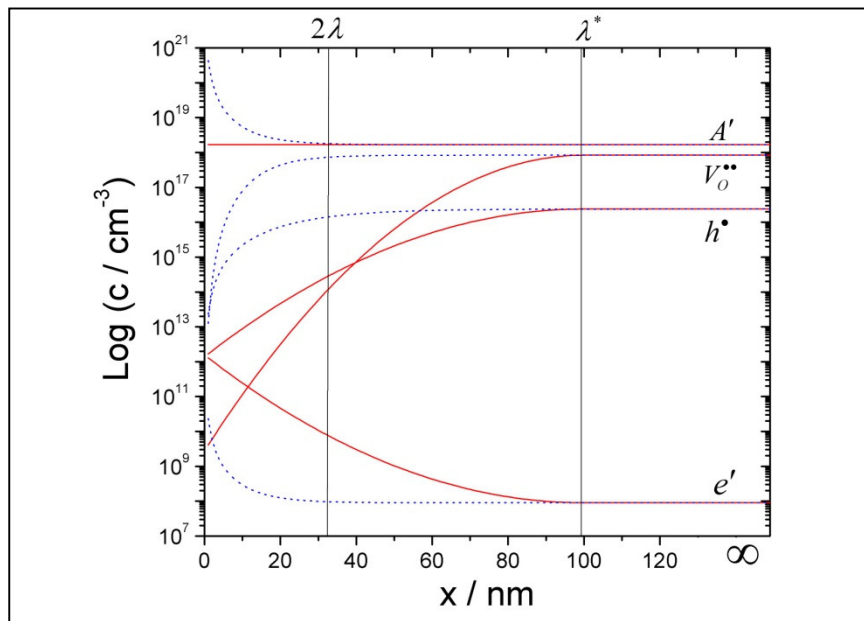


Figure 10 Space charge profiles calculated for acceptor doped SrTiO₃ assuming $T = 500^\circ\text{C}$, $P = 1$ bar, $m = 1.68 \cdot 10^{18} \text{ cm}^{-3}$ (0.01at%), $\Delta\phi_0 = 0.70 \text{ eV}$, according to the Gouy-Chapman model (blue dotted line) and to the Mott-Schottky model (red lines). Under this assumptions, for the Gouy-Chapman profiles the space charge layer width is given by $2\lambda = 32 \text{ nm}$, whereas for the Mott-Schottky case $\lambda^* = 100 \text{ nm}$.

The term $\Delta\phi_0 = \phi(0) - \phi(\infty)$ is the potential of the grain boundary core relative to the bulk, also known as space charge potential. It is related to the charge density in the GB core (Σ) by the following equation: ^[107]

$$\Sigma = \sqrt{8kTc_{j\infty}\epsilon_0\epsilon_r} \sinh\left(\frac{z_j e \Delta\phi_0}{2kT}\right). \quad 2.41$$

2.3.2 Mott-Schottky profiles

In the Mott-Schottky approximation of the Poisson's equation, ^[110,111] the concentration of the immobile acceptors A' is assumed as constant up to the boundary, but, nevertheless, determines the space charge at the interface. ^[8,58] This assumption is reasonable for acceptor doped SrTiO₃ at $T < 1000^\circ\text{C}$, ^[58,60] at which the material is investigated in this study. Since the space charge potential demands the depletion of the counter majority defect, the impurity profile governs the charge density. Consequently, the depleted carrier can be neglected and the charge density can be assumed constant as it is the second derivative of the electrostatic potential $\phi(x)$. Under these assumptions, Eq. 2.36 becomes: ^[26]

$$\frac{\partial^2 \phi(x)}{\partial x^2} = -\frac{z_j e c_{j\infty}}{\epsilon_0 \epsilon_r}. \quad 2.42$$

Eq. 2.42 can be integrated assuming the appropriate semi-infinite boundary conditions

$$\begin{aligned} \phi'(\lambda^*) &= 0 \\ \phi(\lambda^*) &= \phi_\infty \end{aligned} \quad 2.43$$

yielding

$$\phi(x) - \phi_\infty = \Delta\phi(x) = -\frac{z_j e c_{j\infty}}{2\epsilon_0 \epsilon_r} (x - \lambda^*)^2. \quad 2.44$$

The term λ^* is the space charge layer width in the Mott-Schottky case and is obtained rearranging Eq. 2.44 for $\Delta\phi(x=0) = \Delta\phi_0$, giving:

$$\lambda^* = \sqrt{\frac{2\epsilon_0 \epsilon_r \Delta\phi_0}{z_j e c_{j\infty}}} = \lambda \cdot \sqrt{\frac{4z_j e}{kT} \Delta\phi_0}. \quad 2.45$$

In Eq. 2.45, the space charge potential $\Delta\phi_0$ represents the Schottky barrier height when a back-to-back barrier model is assumed.

The concentration profiles in the space charge region are then obtained by combining Eq. 2.35 and Eq.2.44, yielding to.^[26,60,107]

$$\left(\frac{c_j(x)}{c_{j,\infty}} \right) = \exp \left(-z_j \left(\frac{x - \lambda^*}{2\lambda} \right)^2 \right). \quad 2.46$$

For SrTiO₃ in which oxygen vacancies $V_O^{\bullet\bullet}$, electrons e' and electron holes h^\bullet are the predominant mobile carriers, according to Eq. 2.35, the concentration profiles in the space charge layer are related as follows:

$$\left(\frac{c_{V_O^{\bullet\bullet}}(x)}{c_{V_O^{\bullet\bullet},\infty}} \right)^{1/2} = \left(\frac{c_{h^\bullet}(x)}{c_{h^\bullet,\infty}} \right) = \left(\frac{c_{e',\infty}}{c_{e'}(x)} \right). \quad 2.47$$

The concentration profiles calculated according to the Mott-Schottky approximation for SrTiO₃ (0.01at% acceptor doped) at 500°C and $P = 1$ bar are illustrated in Figure 10(red lines). Given a positively charged GB core in SrTiO₃, the oxygen vacancies $V_O^{\bullet\bullet}$ and the electron holes h^\bullet are depleted in the space charge layers, whereas the electrons e' are enriched there, according to Eq. 2.47. The main difference of the Mott-Schottky case from the Gouy-Chapman models consists in the fact that when the majority defects cannot redistribute, the space charge width is dependent on the space charge potential $\Delta\phi_0$ and the depletion width is greater in spatial extent due to a reduced screening ability (see Figure 10).^[107,110,111] Therefore, in the Gouy-Chapman case, there is a very large change in the carrier concentration within one Debye length from the GB, whereas in the Mott-Schottky case the concentration change is less severe.

As the core charge is compensated by the space charge of the two adjacent depletion layers ($\Sigma = 2c_{j,\infty}e\lambda^*$), the core charge density Σ can be related to the space charge potential $\Delta\phi_0$. In the Mott-Schottky approximation (Eq. 2.44), this results in the following equation:^[66]

$$\Sigma = \sqrt{8\varepsilon_r\varepsilon_0em\Delta\phi_0}. \quad 2.48$$

2.4 Brick layer model

If one now considers a polycrystalline material, the total resistivity is given by the contribution of bulk and GBs, according to the brick layer model represented in Figure 11, in which grains are modelled as cubes separated from each other by grain boundaries.^[15,112-114] This simplified description of the grains allows the deconvolution of the different conduction pathways followed by the different mobile charge carriers. The contribution of the boundaries on the overall conduction properties is different depending on whether the depletion situation (i.e. oxygen vacancies and electron holes in SrTiO₃) or the accumulation situation (electrons in SrTiO₃) is considered. This comes to the fore in undoped and acceptor doped SrTiO₃, in which the three regimes (p-type, ionic and n-type) are typically experimentally observed.

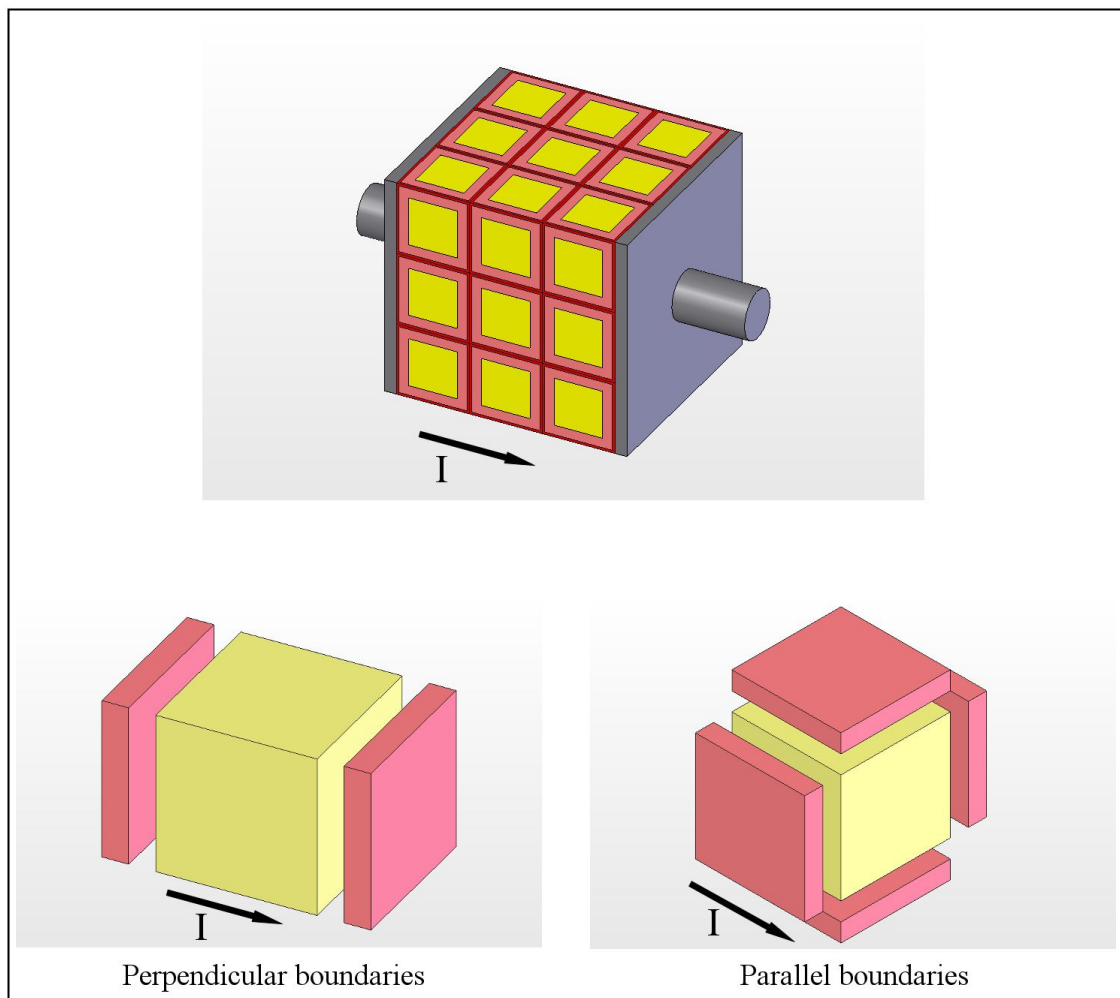


Figure 11 A schematic rendering of the brick layer model for a cubic crystal. The grains are modelled as cubes separated from each other by grain boundaries. The cases of perpendicular (blocking) and parallel boundaries are represented for a single grain.

In SrTiO₃, in the accumulation mode, the highly electron conductive GBs dominate the conduction. This takes place in the low P regime. In this case the current flows through the parallel boundaries and the total GB conductivity σ_{GB}^{\parallel} is given by:^[18]

$$\sigma_{GB}^{\parallel} = (\rho_{GB}^{\parallel})^{-1} = \sum_j (\rho_{GB,j}^{\parallel})^{-1} = \sum_j \frac{1}{\delta} \int_0^{\delta} \sigma_j(x) dx. \quad 2.49$$

On the other hand, in the depletion mode, the current is blocked by the perpendicular boundaries, whose resistances are placed in series and therefore:^[18]

$$\sigma_{GB}^{\perp} = (\rho_{GB}^{\perp})^{-1} = \left(\sum_j \rho_{GB,j}^{\perp} \right)^{-1} = \sum_j \left[\frac{1}{\delta} \int_0^{\delta} (\rho_j(x)) dx \right]^{-1}. \quad 2.50$$

In Eq.s 2.49 and 2.50 δ is the average thickness of the grain boundary, i.e. the space charge layer width, which e.g. is equal to λ^* in the Mott-Schottky approximation.

If only one carrier is dominant, the GB resistance perpendicular to the current R_{GB}^{\perp} is hence described by the following equation when a Mott-Schottky situation is assumed:^[63,115]

$$R_{GB}^{\perp} = \frac{1}{\sigma_{GB}^{\perp}} \cdot \frac{\lambda^*}{S} = \int_0^{\lambda^*} \frac{1}{\sigma(x)} \cdot \frac{dx}{S} \quad 2.51$$

where S is the area concerned. Now, taking into account Eq. 2.35 one obtains:

$$R_{GB}^{\perp} = \frac{1}{\sigma_{Bulk} \cdot S} \int_0^{\lambda^*} \exp\left(\frac{ze\Delta\phi(x)}{kT}\right) dx. \quad 2.52$$

Knowing that the resistance of the bulk of the same size is given by $R_{bulk}^* = (\lambda^* / (\sigma_{bulk} \cdot S))$,^[106] the resistance enhancement:

$$\frac{R_{GB}^{\perp}}{R_{bulk}^*} = \frac{1}{\lambda^*} \int_0^{\lambda^*} \exp\left(\frac{ze\Delta\phi(x)}{kT}\right) dx = \frac{\sigma_{bulk}}{\sigma_{GB}^{\perp}} \quad 2.53$$

which is approximately:^[63]

$$\frac{R_{GB}^{\perp}}{R_{bulk}^*} = \frac{\sigma_{bulk}}{\sigma_{GB}^{\perp}} = \frac{\exp(ze\Delta\phi_0 / RT)}{2ze\Delta\phi_0 / RT} \quad 2.54$$

Under the assumption of a brick layer situation the capacitance of the bulk is defined as $C_{Bulk} = \epsilon_0 \epsilon_{bulk} (A / nd_g)$, whereas the GB one is defined as

$C_{GB} = \epsilon_0 \epsilon_{GB} (A / n\delta)$, being A the cross section area of the sample, d_g the grain size and n the number of the grains.

Then, the GB thickness can be described as:^[106]

$$\delta = \frac{\epsilon_{Bulk}}{\epsilon_{GB}} \frac{C_{Bulk}}{C_{GB}} d_g \quad 2.55$$

Under the assumption that $\epsilon_{Bulk} \approx \epsilon_{GB}$ and knowing that $R_{Bulk} = (1 / \sigma_{bulk})(nd_g / A)$ and $R_{GB} = (1 / \sigma_{GB})(n\delta / A)$, the specific GB conductivity σ_{GB}^\perp is determined as follows:

$$\sigma_{GB}^\perp = \sigma_{bulk} \cdot \frac{C_{Bulk} R_{Bulk}}{C_{GB} R_{GB}}. \quad 2.56$$

The activation energy ΔE_{GB}^\perp of the grain boundary conductivity σ_{GB}^\perp , defined by^[64]

$$\Delta E_{GB}^\perp = - \frac{\partial \ln \sigma_{GB}^\perp}{\partial (1/kT)}. \quad 2.57$$

follows from Eq. 2.54 and 2.57, as^[64]

$$\Delta E_{GB}^\perp = \Delta E_{bulk} + e\Delta\phi_0 - kT + \frac{\partial \Delta\phi_0}{\partial (1/kT)} \left(\frac{e}{kT} - \frac{1}{\Delta\phi_0} \right). \quad 2.58$$

2.5 The conductivity minimum

The conductivity minimum corresponds to the p - n transition where the electron and hole contributions to the conductivity are equal (see Figure 7b and Figure 9). This can be expressed by:

$$\frac{1}{2} \sigma_{min} = ne u_n = np u_p. \quad 2.59$$

Combining 2.59 with the band-band transfer (Eq. 2.4), the conductivity at P_{min} results to be independent from the impurity/dopant content and can be written as:

$$\sigma_{min} = 2F \sqrt{u_n u_p K_B}. \quad 2.60$$

The temperature dependence of the minimum is primarily determined by the band-gap energy of the material, which is represented by the term E_B in Eq. 2.4; The contribution of the T dependence of the mobility has been found to be small.^[36]

Now, considering the band-band transfer (Eq.2.4), the electroneutrality (Eq. 2.11), the oxygen incorporation reaction (Eq. 2.14) and the condition of the minimum (Eq. 2.59), the P at which the bulk conductivity minimum appears ($P_{min}(L \rightarrow \infty)$) can be estimated to be:

$$P_{min} = \left(\frac{K_B}{K_{ox}} \right)^2 \cdot \frac{4}{m^2} \cdot \left(\frac{u_n}{u_p} \right)^2. \quad 2.61$$

If one considers now the GB contribution, in light of the space charge model, the charge carrier concentrations at a given distance x from the grain boundaries are given as follows:

$$\begin{aligned} n(x) &= n_\infty \cdot \kappa(x) \\ p(x) &= p_\infty \cdot [\kappa(x)]^{-1} \\ v(x) &= v_\infty \cdot [\kappa(x)]^{-2} \end{aligned} \quad 2.62$$

being $\kappa(x) = \exp(e\Delta\phi(x)/RT)$.

From Eq.s 2.4, 2.14, 2.59

$$P_{min}(x) = \left(\frac{K_B}{K_{ox}} \right)^2 \cdot [v(x)]^{-2} \cdot \left(\frac{u_n}{u_p} \right)^2 \quad 2.63$$

is obtained, which, by taking into account 2.62, can also be written as

$$P_{min}(x) = \left(\frac{K_B}{K_{ox}} \right)^2 \cdot \frac{1}{v_\infty^2} \cdot \left(\frac{u_n}{u_p} \right)^2 \cdot [\kappa(x)]^4 = \left(\frac{K_B}{K_{ox}} \right)^2 \cdot \frac{4}{m^2} \cdot \left(\frac{u_n}{u_p} \right)^2 \cdot [\kappa(x)]^4 \quad 2.64$$

being $m = 2v_\infty$ the acceptor concentration in the bulk.

If the sample width is becoming so small that the assumption of flat profiles that now $v(x) \approx v(x=0) \equiv v_0$, we obtain for $P_{min}(L \rightarrow 0)$, i. e. P_{min} in the mesoscopic limit:

$$P_{min}(L \rightarrow 0) = \left(\frac{K_B}{K_{ox}} \right)^2 \cdot v_0^{-2} \cdot \left(\frac{u_n}{u_p} \right)^2 = \left(\frac{K_B}{K_{ox}} \right)^2 \cdot \frac{4}{m^2} \cdot \left(\frac{u_n}{u_p} \right)^2 \cdot \kappa_0^4. \quad 2.65$$

Experimental methods

In order to investigate the size effects on the conductivity of nanocrystalline materials the preparation of the samples becomes a crucial step. This involves the synthesis of the nanopowders, as well as the subsequent sintering process. Different synthesis procedures have been employed, while spark plasma sintering has emerged to be very powerful in the field of nanomaterials and it was largely used in this work. These aspects as well as the other experimental methods employed are described in this chapter.

3.1 Synthesis of the nanopowders

The synthesis of the nanopowders is a crucial part for the preparation of nanocrystalline SrTiO₃ samples. A broad variety of wet chemical methods has been reported in literature for the preparation of nanocrystalline titanates, such as different sol-gel methods,^[116-119] combustion synthesis,^[120] hydrothermal synthesis,^[121,122] solid state reaction synthesis^[123] and, recently, microwave synthesis.^[124]

In this work, three different routes have been considered for the synthesis of nanocrystalline SrTiO₃, namely co-precipitation (method A),^[74] combustion (method B),^[118] solvothermal (method C)^[125] methods. Starting from the procedures described in literature, these methods have been improved with the purpose of (i) reducing the resulting grain size and (ii) enhance the reproducibility of the synthesis.

In addition, since a detailed characterization of the as-synthesized powders was missing, this was carried out in this study. Particular attention was given to those aspects, which affect the grain size (e.g. the calcination temperature) and which

influence the final electrical properties of the material (e.g. stoichiometry and dopant distribution). The synthesis procedures are described thoroughly in chapter 4, together with the discussion of the powders characterization.

3.2 Spark plasma sintering: technique and improvements

Spark plasma sintering (SPS) has emerged as one of the most significant and effective techniques for the densification of ceramic materials.^[126-132] Although the definition spark plasma sintering is widely used, it is worth noting here that it might be misleading in light of recent studies, which excluded plasma generation, sparking or arcing during the whole sintering process.^[133] Therefore, other definitions have been suggested, such as pulsed electric current sintering (PECS),^[134] field assisted sintering technology (FAST),^[135] electric current activated/assisted sintering technique (ECAS),^[131] current-activated pressure-assisted densification (CAPAD).^[132] However, for the sake of simplicity, in this work I will refer to this technique as spark plasma sintering (SPS), since this is still the most used acronym in literature.

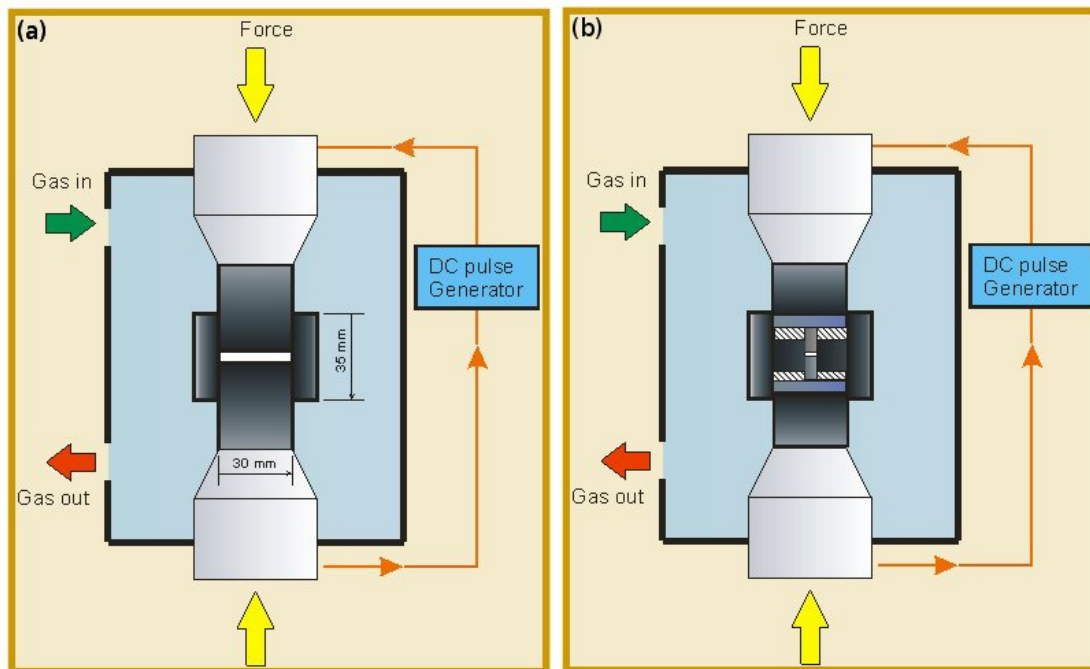


Figure 12 Spark plasma sintering set up. (a) commercial; (b) modified. The commercial set up was modified with the introduction of an internal die made of graphite in which the powders are placed. The additional small pistons are made of SiC and the discs between them and the graphite are made of WC.

The SPS process consists in the densification of powders under the simultaneous application of a DC electric current and a mechanical pressure, but, despite over 40 years of research and development, a large gap exists between the fundamental understanding of the SPS process and the technological advances of the process.

In this project, the SPS press HP D 5 supplied by FCT Systems GmbH (Germany) was employed. The commercial set up is schematically illustrated in Figure 12a. The apparatus consists of a vacuum chamber, two pistons made of steel for the application of the load (light gray parts in Figure 12a-b) and a die with two pistons with diameter of 30 mm, in which the powders are placed. The latter are made of highly pure and dense graphite, because it exhibits mechanical strength up to very high temperatures, as well as high thermal and electrical conductivity.

Compared to the typical hot press (HP) techniques in which the mold in which the powders are placed is heated by radiation from the enclosing furnace, in the SPS method the die is heated by Joule effect from the current (DC or pulsed DC) flowing through it. Thanks to the simultaneous application of the load and of the current, the advantages offered by the SPS technique consist in the possibility of employing lower sintering temperatures, high heating and cooling rate and shorter holding times. This makes it possible to significantly reduce the sintering times, while obtaining densities very close to the theoretical ones. These aspects are advantageous for the fabrication of nanocrystalline materials as they allow to limit the grain growth.

Apart from temperature, holding time and pressure, whose influence on the densification process is very well understood,^[77] in the SPS process also the role of heating rate and pulses has come to the fore. Moreover, Anselmi-Tamburini *et al.*,^[126,127,136-138] Munir *et al.*^[128] and Garay^[132] investigated deeply the role of the current and the densification mechanism involved in the SPS process. In particular, it has been observed that high heating rates tend to favour densification over coarsening because surface diffusion has a low activation energy and it is more active at lower temperature regimes compared to grain boundary or volume diffusion.^[132] Thus, by bringing the powders to the sintering temperature in a shorter time, one can minimize coarsening, and also obtain dense pellets.

On the other hand the current has an influence on mass transport.^[138] Electromigration or current-enhanced mass transport is a well known effect^[139,140] and

through systematic investigations it was demonstrated that it may be active at the current density used in SPS.^[141-143] If current does indeed increase diffusivity, then all the densification mechanism (namely surface diffusion, lattice diffusion and GB diffusion)^[77] are enhanced.^[132,144]

In order to prepare the pellets investigated in this project, the commercial set up was modified as suggested in ref. [145], with the aim of reducing the effective area on which the force is applied (Figure 12b). This approach revealed to be very successful for the densification of nanocrystalline materials. Notably, by inserting an internal die with a diameter of 5 mm into the commercial die, pressures up 500 MPa may be reached. In this way, the sintering temperature can be strongly decreased, since the pressure itself supplies a huge amount of energy to the system for the densification. Nonetheless, as the graphite parts cannot withstand pressures above 60-80 MPa, materials with better mechanical properties were employed. The small pistons of the internal die have been made of Silicon carbide (SiC) and a disc of tungsten carbide (WC) was placed between the small SiC pistons and the commercial graphite ones. The temperature was controlled with a thermocouple inserted in the external die, very close to the powder.

Typical sintering conditions used in this work for the densification of nanocrystalline SrTiO₃ included a sintering temperature of 750-850°C, reached with a heating rate of 300°C/min, holding time of 5 minutes and a pressure of 350 MPa. Pulsed DC current, with patterns composed by a sequence of 12 pulses (3 ms each) with a break of 3 ms between each sequence was employed.

3.3 Characterization techniques

3.3.1 AC electrochemical impedance spectroscopy

Alternating current (AC) electrochemical impedance spectroscopy (EIS) is a very powerful method for the characterization of the electrical properties of the materials and of their interfaces. It may be used to investigate the dynamics of bound or mobile charges in the bulk and in the interfacial regions of any kind of solid and liquid material, namely ionic, semiconducting, mixed ionic-electronic and even insulators.^[8,34,146]

In particular, in polycrystalline materials, its importance arises from the fact that it is possible to distinguish the contributions to the electrical resistance and capacitance due to the transport across grains, across GBs and at the electrode. This was first observed by Bauerle in 1969 in Y-doped ZrO₂.^[147]

EIS consists of the application of an alternating voltage $U(t) = U_0 \cos(\omega t + \theta)$ across the sample and in measuring the current response, $I(t) = I_0 \cos \omega t$, as a function of the angular frequency ω . Here, θ is the phase difference between the voltage and the current: it is zero for purely resistive behaviour, -90° for purely capacitive behaviour and $+90^\circ$ for purely inductive behaviour. For example a single crystal with predominant ion conduction exhibits a resistance due to the ohmic losses associated with ionic drift and a capacitance due to the dielectric (ionic and electronic) polarization of the material given by the dielectric constant. The impedance Z^* associated with this behaviour is expressed by the following equation, taking into account the Euler's formula:^{*}

$$Z^* = \frac{U(t)}{I(t)} = \frac{U_0}{I_0} \exp(-i\theta) = Z(\cos \theta - j \sin \theta). \quad 3.1$$

Z^* can be plotted in the complex plane with the real part $Z' = Z \cos \theta$ on the x axis and the imaginary part $Z'' = Z \sin \theta$ on the y axis (Nyquist plot). This results in a semicircular arc, which can be modelled using an equivalent circuit containing a resistor R and a capacitor C in parallel, over the whole frequency range.^[147]

In the Nyquist plot of Z^* , the low frequency intercept of the arc with the x axis corresponds to the resistance R , since, when $\omega \rightarrow 0$, the influence of the capacitance

^{*} Given a sinusoidal quantity $A(t) = A_0 \cos(\omega t + \theta)$, using the Euler's formula it can be written as $a(t) = A_0 \cdot e^{j(\omega t + \theta)}$.

vanishes and the DC resistance is obtained. The inverse of the frequency at the peak gives the relaxation time constant $\tau = \omega_{max}^{-1} = RC$.

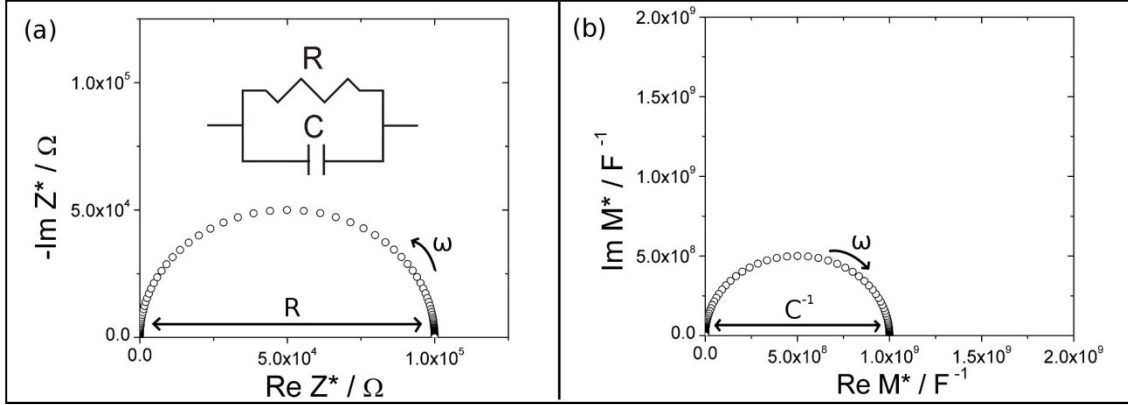


Figure 13 Simulated (a) impedance and (b) dielectric modulus Nyquist plots for a single contribution, assuming $R = 10^5 \Omega$ and $C = 10^{-9} F$. The frequency varies from 2MHz to 0.1 Hz, which is the range considered in this work. The equivalent circuit composed by one RC element is represented.

In the case of a single contribution associated with a simple parallel RC circuit, the corresponding impedance is given by:^[8]

$$Z_{RC}^* = \frac{R}{1 + j\omega^2\tau^2} + j \left(-\frac{R\omega\tau}{1 + j\omega^2\tau^2} \right) = Z' + jZ'' \quad 3.2$$

This results for example in the simulated spectra represented in Figure 13a and it can describe for example the behaviour of a single crystal, when reversible electrodes are assumed.

In addition, there are several other derived quantities of importance in EIS: (i) the complex admittance, which is defined as the inverse of the impedance, $Y^* = (Z^*)^{-1}$; (ii) the complex capacitance, which is given by $C^* = Y^* / j\omega$; (iii) the dielectric modulus, which is the reciprocal of the complex capacitance ($M^* = j\omega Z^*$).^[146]

With respect to the current work, the latter is particularly relevant. It can be expressed as:^[148]

$$\begin{aligned} (M^* / C_c) &= (\epsilon^*)^{-1} = (\epsilon' - j\epsilon'')^{-1} \\ &= \frac{\epsilon'}{(\epsilon')^2 + (\epsilon'')^2} + j \frac{\epsilon''}{(\epsilon')^2 + (\epsilon'')^2} \\ &= (M' + jM'') / C_c \end{aligned} \quad 3.3$$

with $C_c = \epsilon_0 A_c / l$ being the capacitance of the empty measuring cell of electrode area A_c and electrode separation length l and ϵ' and ϵ'' being the real and imaginary part

of the dielectric constant. Plotted in the complex plane the intercept on the x axis is the reciprocal of the capacitance.^[8]

The power of EIS shows when resistive interfaces are present in the system. Notably, the impedance response of a polycrystalline material is composed by bulk, GB and electrode contributions, resulting in three RC circuits placed in series.

If we first consider only the bulk and GB contributions and we ignore the electrode, the total impedance is given by:^[8]

$$Z_{tot}^* = Z_{bulk}^* + Z_{GB}^* . \quad 3.4$$

and hence $Z'_{tot} = Z'_{bulk} + Z'_{GB}$ and $Z''_{tot} = Z''_{bulk} + Z''_{GB}$. As $Z^* = M^* / j\omega$ it also holds that $M'_{tot} = M'_{bulk} + M'_{GB}$ and $M''_{tot} = M''_{bulk} + M''_{GB}$.

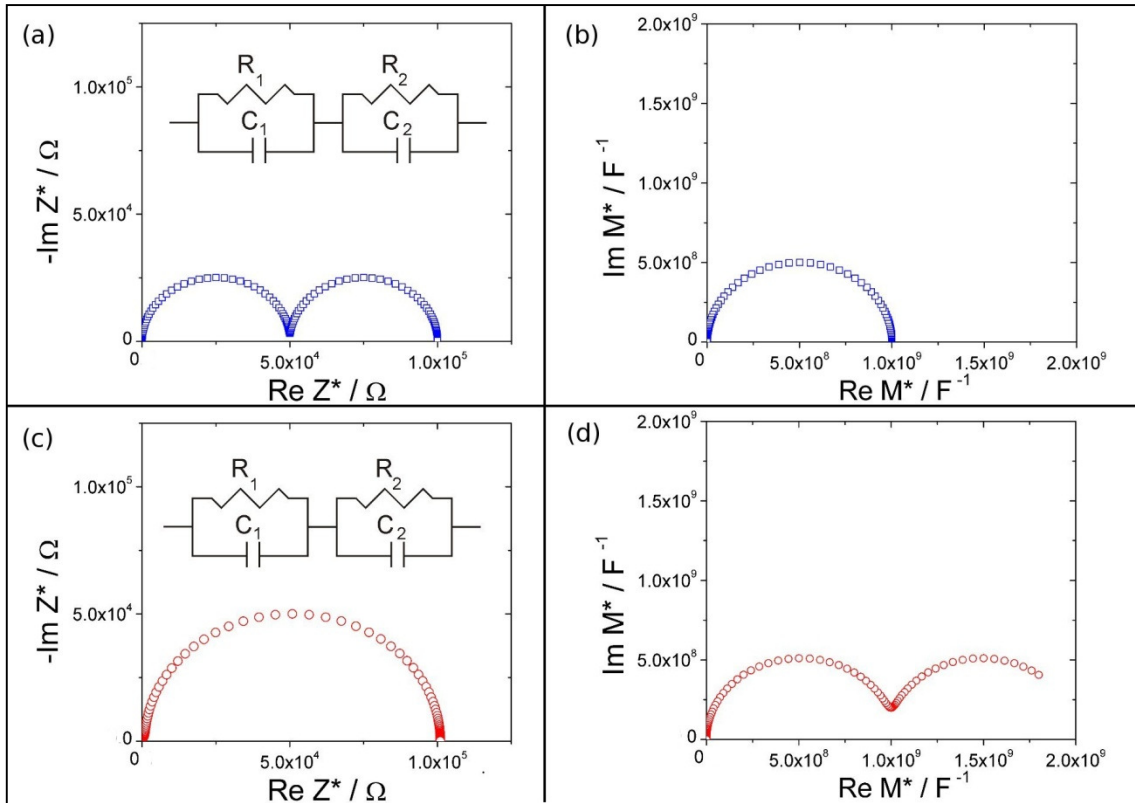


Figure 14 Simulated impedance ((a) and (c)) and dielectric modulus ((b) and (d)) Nyquist plots for a system with two contributions, assuming: (a) and (b) $R_1 = R_2 = 5 \cdot 10^4 \Omega$, $C_1 = 10^{-9} \text{ F}$ and $C_2 = 10^{-6} \text{ F}$; (c) and (d) $R_1 = 10^3 \Omega$, $R_2 = 10^5 \Omega$ and $C_1 = C_2 = 10^{-9} \text{ F}$. The frequency varies from 2 MHz to 0.1 Hz. The equivalent circuit composed by 2 RC elements placed in series is represented. It turns out that when the resistances are similar and the capacitances different, the two contributions can be clearly distinguished in the Z^* -plot. On the other hand, when the capacitances are the same but the resistances are different, the two contributions are clearly visible in the M^* -plot.

If the relaxation times (τ) are sufficiently different, two semicircles are observed. However, there might be cases (see i.e. Figure 14), in which the Nyquist plot

of the impedance is not sufficient to resolve the spectra. Notably, in the complex modulus plane (M'' vs. M') semicircles occur for each RC element in a series array and these are resolvable if (i) the RC relaxation times of the elements differ sufficiently and (ii) this difference is due to R rather than C. On the contrary, in the Z^* -plot two separate semicircles are observed only if the relaxation times of the elements differ as a result of different capacitances rather than different resistances.^[148-149] This can be clearly demonstrated through the simulation of the impedance responses reported in Figure 14. It is worth noting here that the Z^* -plots in Figure 13a and in Figure 14c, at first sight, look exactly the same. However, the analysis of the M^* -plot convincingly demonstrates the presence of a second contribution at high frequencies in the second case.

For these reasons, in polycrystalline materials, it is advantageous to use the dielectric modulus formalism to complement the broadly used impedance formalism. In particular, the M^* -plot is suitable for analysis of capacitances.^[8]

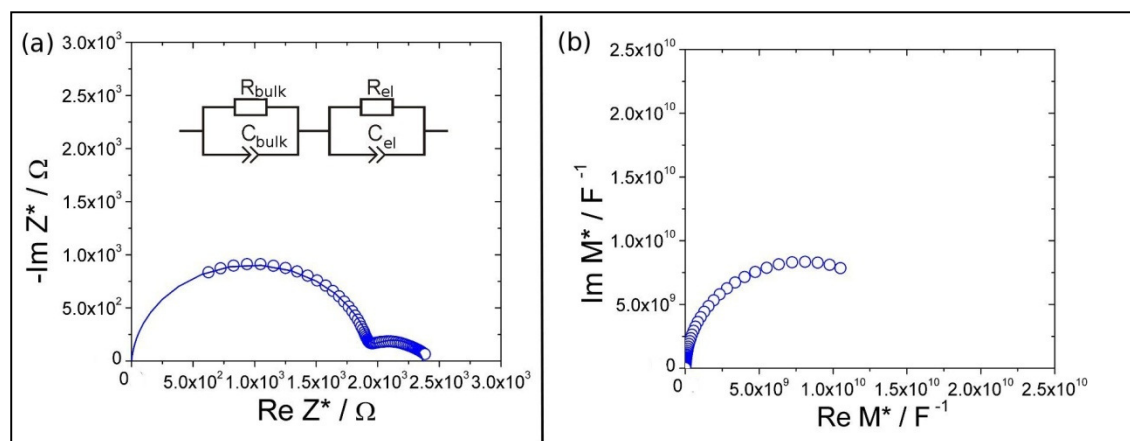


Figure 15 Nyquist plots of impedance (a) and dielectric modulus (b) of a nominally pure SrTiO₃ single crystal with sputtered Pt electrodes. The blue line in (a) refers to the fitting obtained with the equivalent circuit composed by 2 RC elements placed in series. The two contributions are assigned to the bulk (high frequency) and to the electrode (low frequency).

Another contribution, which often appears in the impedance analysis, is the one of the electrode. The combination of impedance and dielectric modulus plot is also useful to identify this contribution. Notably, the electrode capacitance C_{el} is placed in series with the other RC elements of the equivalent circuit and it does not appear in the modulus plot since $C_{el} \gg C_{GB} > C_{bulk}$.^[148] This means that the electrode contribution might be seen in the Z^* -plot but not in the M^* -plot. This is the case of the SrTiO₃ single crystal with Pt sputtered electrodes, whose spectra are shown in Figure 15.

It is worth noting here that the semicircles experimentally observed in the EIS spectra are typically depressed. This non-ideal behaviour originates from the effect of the materials inhomogeneity on the distribution of the current density. This makes it difficult to approximate the impedance with an ideal RC circuit and, consequently, the capacitor C has to be replaced by a constant phase element Q . The capacitance of the contribution is then best calculated from the fitting parameters Q and n according to the following equation:^[150]

$$C = (R^{1-\alpha}Q)^{1/\alpha} \quad 3.5$$

where α indicates the depression of the semicircle, and it must range between 1 (ideal capacitor) and 0.7 for a sensible fitting.

Despite the great advantages that EIS provides for the characterization of polycrystalline materials, one must be aware also that the main difficulty consists in the fact that sometimes the assignment of the arcs to the corresponding contribution may be ambiguous. Therefore, the interpretation of the spectra should be based not only on the Nyquist plot of the impedance and the dielectric modulus, but also on Bode plots, in which Z' , Z'' , M' , M'' and θ are plotted as a function of the frequency ω .^[151,152] In addition, a critical analysis of the values of the activation energy of the conductivity is a very effective mean to assign a semicircle to the bulk or to the GBs contribution. The same can be said for the values of the capacitance, dielectric constants and the absolute values of the electrical conductivity.

In this work, impedance spectroscopy measurements were performed using an Alpha-A high resolution dielectric analyzer (Novocontrol) in the frequency range from 2 MHz to 1 Hz and applying a AC voltage of 0.3 V.

The electrical conductivity and the dielectric constant of the bulk were determined from the experimental data, taking into account the geometry of the sample.

It follows:

$$\sigma_{bulk} = \frac{1}{R_{bulk}} \cdot \frac{h}{A} \quad 3.6$$

$$\epsilon_{bulk} = \frac{C_{bulk} \cdot h}{\epsilon_0 \cdot A} \quad 3.7$$

being h and A the sample thickness and area, respectively.

The calculation of the respective values or the boundaries must take into account their geometrical parameters

The Nernst-Einstein equation can be used to determine the activation energy ΔE of the electrical conductivity from its temperature dependence. Notably, the conductivity can be expressed as:

$$\sigma = \frac{const}{T} \cdot \exp\left(-\frac{\Delta E}{kT}\right) \quad 3.8$$

which can be rewritten as:

$$\ln(T\sigma) = -\left(\frac{\Delta E}{k}\right) \cdot \frac{1}{T} + \ln const. \quad 3.9$$

Hence, if one plots $\ln T\sigma$ versus $1/T$ (Arrhenius plot), the slope is proportional to the activation energy ΔE .

In this work, the activation energy of the conductivity was determined from the impedance spectra acquired every 10°C between 550°C and 400°C at the desired P .

The P -dependence of the conductivity was determined with oxygen partial pressure P ranging between 10^{-5} and 1 bar and, using CO-CO₂ mixtures, between 10^{-19} and 10^{-22} bar. The samples were equilibrated at the desired P for 20 hours before acquiring the final spectrum.

The impedance spectra were analyzed with the software Z-View (Scribner Associates).

3.3.2 X-ray diffraction (XRD)

X-ray diffraction (XRD) using a XRD diffractometer (Xpert, Philips, 3710 HTK, Cu K_{α} =1.54056 Å) was employed on both powders and grinded sintered pellets, in order to (i) check the presence of secondary phases, (ii) determine the grain size, the lattice parameter, and the strain. Rietveld refinement was applied on the XRD patterns using GSAS.^[153] The peak profiles were modelled using a modified pseudo-Voigt function (CW function #3). Instrumental broadening and peak asymmetry were determined with LaB₆ and fixed during the refinements.

3.3.3 Electron microscopy

Electron microscopy was employed for the characterization of the powders as well as of the pellets.

In particular, field emission scanning electron microscopy (FESEM) was used to analyze the microstructure of the sintered specimens with grain size larger than 50 nm powders.

On the other hand, transmission electron microscopy (TEM – ZEISS EM 912 Omega) was employed for the characterization of the nanopowders as well as of the sintered pellets with grain size smaller than 50 nm.

The distribution of the dopant cations within the samples was investigated by EDXS (Energy Dispersive X-Ray Spectroscopy) using a dedicated scanning TEM (VG HB 501UX equipped with a Noran Voyager EDX system)

3.3.4 Extended X-ray Absorption Fine Structure (EXAFS)

X-ray absorption spectra (XAS) experiments were carried out at the XAFS beamline of the Synchrotron Light Laboratory Elettra (Trieste, Italy) on both powders and sintered pellets. Spectra were collected in transmission mode at 80 K. The extended X-ray absorption fine structure (EXAFS) spectra were analyzed using Feff 8.4^[154] and Viper.^[155] The EXAFS experiments and data analysis were performed in collaboration with Dr. Francesco Giannici from the University of Palermo (Italy).

3.3.5 Inductive coupled plasma - optical emission spectroscopy (ICP-OES)

The concentration of metal traces was measured by Inductive coupled plasma - optical emission spectroscopy (ICP-OES - Spectro Ciros CCD, Spectro Analytical Instruments, Germany) at the analytical chemistry laboratory of the Max Planck Institute for Intelligent Systems. The measurements were carried out on the solutions obtained by high pressure microwave assisted decomposition in HCl (37%) at 200°C for 1.5 hours.

3.3.6 Thermogravimetric analysis (TGA)

Thermogravimetric analysis (TGA - STA449, Netsch, Germany) was employed to determine the mass loss of the dried precipitates and, consequently, to decide the suitable calcination temperature for the as-synthesised powders. The samples were heated with a heating rate of 5°C/min in an atmosphere which reproduced synthetic air (mixture of 20% O₂ and 80% N₂) from room temperature to 1100°C.

Results and discussion

4.1 Synthesis and characterization of nanocrystalline SrTiO₃

As already anticipated in chapter 3, in this work, nanocrystalline SrTiO₃ has been synthesized according to three different procedures, namely co-precipitation (method A),^[74] combustion (method B),^[118] solvothermal (method C)^[125] methods, which are described in details in this section. The powders were characterized as follows. X-ray diffraction was used to identify the phase and to verify whether secondary phases formed during the synthesis; thermogravimetric analysis was used to determine the calcination temperature; the final grain size and the shape of the grains were investigated via TEM; ICP-OES was used to establish the impurity and the dopant content; EXAFS was used to investigate the average local environment of host cation as well as the one of the dopant.

4.1.1 Method A: modified peroxide-based method

Balaya *et al.*^[74] developed a modified peroxide-based route to prepare nanocrystalline SrTiO₃, using Ti metal foil and Sr(NO₃)₂ as precursors. The whole process is schematically illustrated in the flow chart in Figure 16.

Titanium (metal foil from Aldrich: h=0.127mm; purity=99.7%) was dissolved in a solution of H₂O₂ (30mol%) and NH₃ (25mol% in water), characterized by a pH of 11. Here, the procedure of ref. [74] was modified and, for the synthesis, a homemade cell, in which refrigerated ethylene glycol was let flow, was used in order to maintain

the temperature of the solution at 5°C during the whole procedure. This was necessary in order to minimize the evaporation of NH₃ and the subsequent reduction of the pH. The solution was stirred vigorously at 5°C for about 30 hours until the total dissolution of Ti. At this point an equal amount of moles of ethylenediaminetetraacetic acid (EDTA) was added and the solution was stirred for 20 minutes. Then, 40 ml of bidistilled H₂O were added and the solution was stirred for another 10 minutes, before adding again an equal amount of moles of EDTA.

Subsequently, the pH of the solution was reduced to 8 with the addition of HNO₃ and stirring was kept for another 30 minutes.

Meanwhile, an equal amount of moles of Sr(NO₃)₂ was dissolved in another beaker and was added dropwise to the Ti solution. After that a few drops of HNO₃ were added to reduce the pH to 7 and the resulting pale green solution was left under stirring for 15 hours at 1°C in order to let the reaction complete.

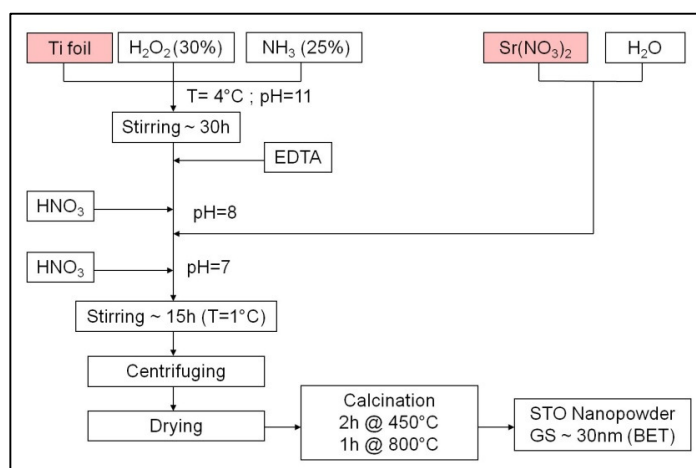


Figure 16 Flow chart representing the procedure of the co-precipitation synthesis (method A).

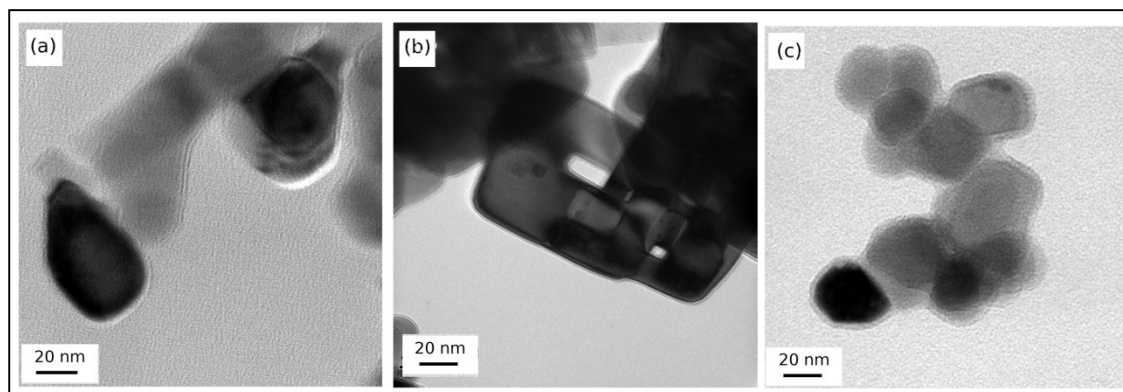


Figure 17 TEM micrographs of the final SrTiO₃ powders prepared via (a) and (b) co-precipitation, (c) combustion method.

Afterwards, it was centrifuged and washed with bidistilled H₂O and then dried in vacuum at 80°C overnight. Alternatively, spray drying was also used and it was observed that it reduced the agglomeration. The as-synthesized powder was calcined at 400°C for 1 hour and 700°C for 2 hours, in order to avoid the formation of SrCO₃ and to remove other undesired compounds formed during the process (e.g. nitrate groups). The final grain size was approximately 30 nm, as shown in Figure 17a.

Several attempts to dope the powders with the co-precipitation method were performed. Iron (III) nitrate in stoichiometric ratio was added to the Ti solution before the addition of the Sr solution. However, ICP-OES measurements could detect in the final powders only a small amount of Fe, ascribed to the intrinsic impurity content. This means that Fe did not take part in the reaction. Moreover, these powders were characterized by intergranular porosity as it can be seen from the TEM micrographs (Figure 17b). This fact, already observed by Hennings *et al.* [156], reduces the final effective grain size of the powders.

4.1.2 Method B: polymeric precursor method

The polymeric precursor method was introduced by Pechini [118] and later analyzed by Kakihana [119]. In the last years it has been often used to prepare ultrafine BaTiO₃ particles [157-159]. Here, the method was adapted for the synthesis of the similar SrTiO₃ perovskite. As illustrated in the flow chart of Figure 18, citric acid was dissolved in ethylene glycol (mixed in molar ratio 1:4) at around 100°C until complete dissolution. Ti-isopropoxide was added and the solution was left stirring until no precipitates were present. In the meanwhile, Sr(NO₃)₂ (Ti:Sr = 1) was dissolved in water and added into the Ti solution. At this point some precipitates appeared. However, the solution must be stirred at 100°C until they dissolved completely and a yellowish clear solution was obtained.

This solution was slowly heated from 100°C to 250°C. At around 150°C the reaction started and a white glassy resin started forming. The beaker with the intermediate compound was then put into the furnace at 300°C for 2 hours. At this stage the combustion took place and the result was a black burned mass. TGA performed on this mass and shown in Figure 19 revealed that all the organics (approximately 60% of the total initial mass) had completely disappeared above 650°C. Therefore, after grinding in the mortar, the black powder was calcined at 650°C for 2 hours and a white SrTiO₃ powder was obtained.

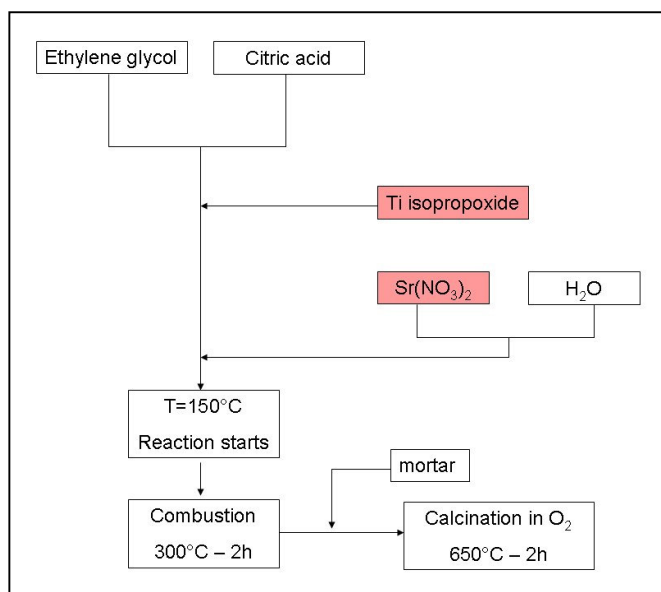


Figure 18 Flow chart representing the procedure of the combustion synthesis (method B).

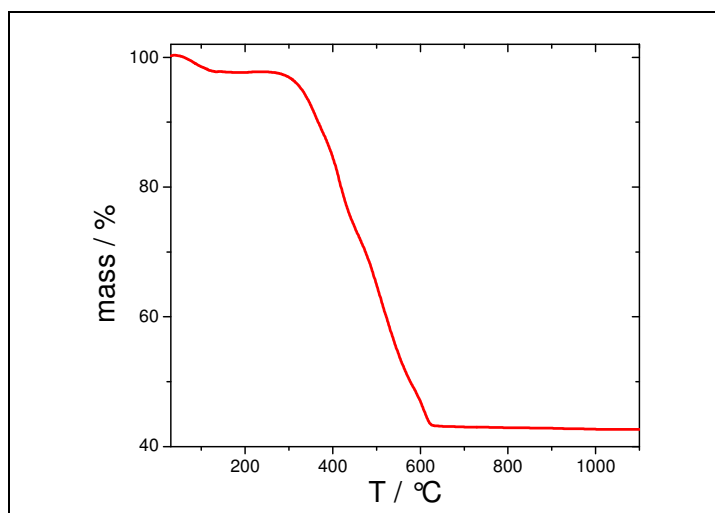


Figure 19 TGA performed on the powder prepared according to the method B (heating rate: 5°C/min; Atmosphere: 20%O₂ and 80%N₂)

X-Ray diffraction patterns (Figure 20) showed that the atmosphere in which the calcination takes place is a crucial parameter to avoid the formation of a secondary phase, namely SrCO₃. As already mentioned in ref. [74], it was observed that the formation of SrCO₃ occurs in air between room temperature and 400°C, due to the reaction of the powder with the CO₂ present in the atmosphere. The formation of SrCO₃ can be avoided if the powder is calcined in pure O₂ or in air, in a furnace already pre-heated at 650°C.

The final grain size of the single phase powder is about 20 nm (see micrograph in Figure 17b).

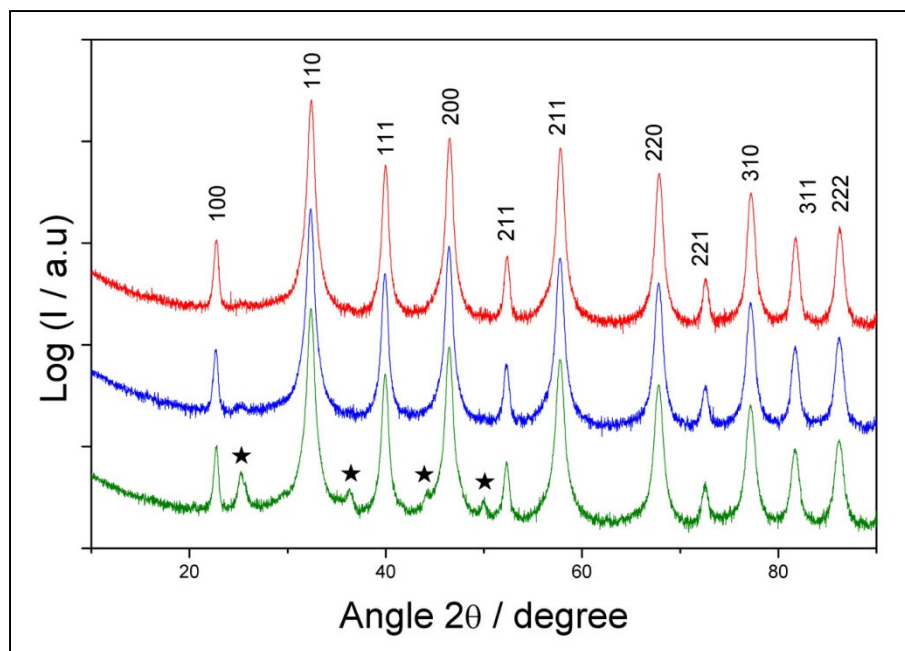


Figure 20 XRD patterns of SrTiO₃ prepared via combustion synthesis upon different calcination processes: (**red line**) in O₂ without pre-heat; (**blue line**) in air with pre-heat at 650°C; (**green line**) in air without pre-heat. The star indicates the peaks of SrCO₃.

4.1.3 Method C: Solvothermal method

Surfactant-free nonaqueous sol-gel routes are one of the most effective synthesis processes for nanocrystalline metal oxides and it has been used to obtain a large number of compounds^[160]. Nanocrystalline SrTiO₃ was synthesized according to ref. [125], as schematically illustrated in Figure 21.

This method has revealed also the most promising route for the synthesis of acceptor and donor doped SrTiO₃. Titanium (IV) isopropoxide (99.999%), strontium metal (99.99%) and anhydrous benzyl alcohol (99.8%) ordered by Aldrich were used as precursors. Inside the glovebox, strontium metal (12.4 mmol) was stirred in 125 ml of benzyl alcohol at 120°C until complete dissolution (~12 hours). The resulting yellowish clear solution was then cooled down to room temperature.

Alternatively, a mixture of benzyl alcohol and pentanol (3:1 volumetric ratio) was used to investigate whether a different solvent could affect the grain size of the nanocrystalline powders.

At this point Ti-isopropoxide was added, the solution was left stirring for some minutes and then poured into two autoclaves (Parr acid digestion vessel, 125 ml), which

were then taken out of the glovebox and put into a furnace at 200°C for 48 hours. The resulting suspension was subsequently centrifuged and the precipitates were washed with ethanol and dimethyl ether and finally dried at 80°C for 12 hours in vacuum.

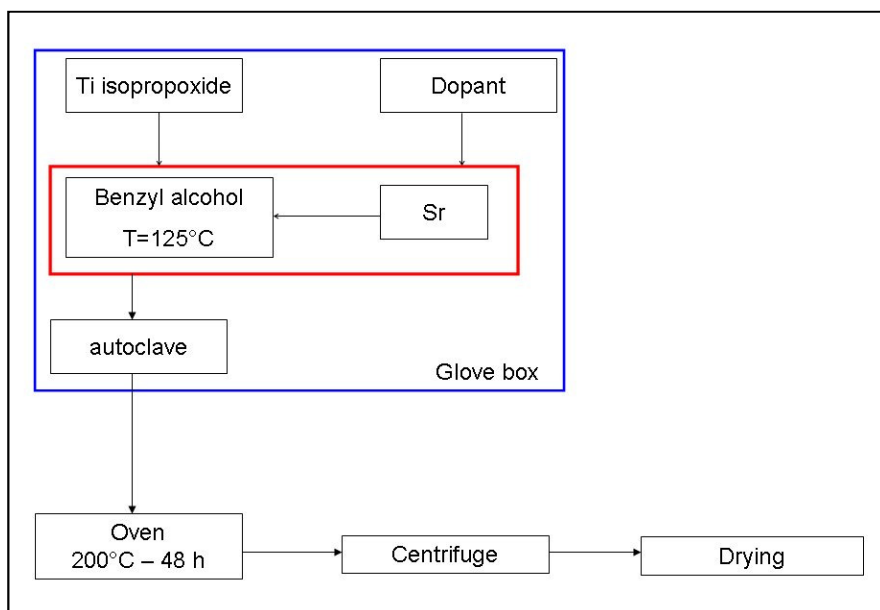


Figure 21 Flow chart of the synthesis procedure of the solvothermal method (method C)

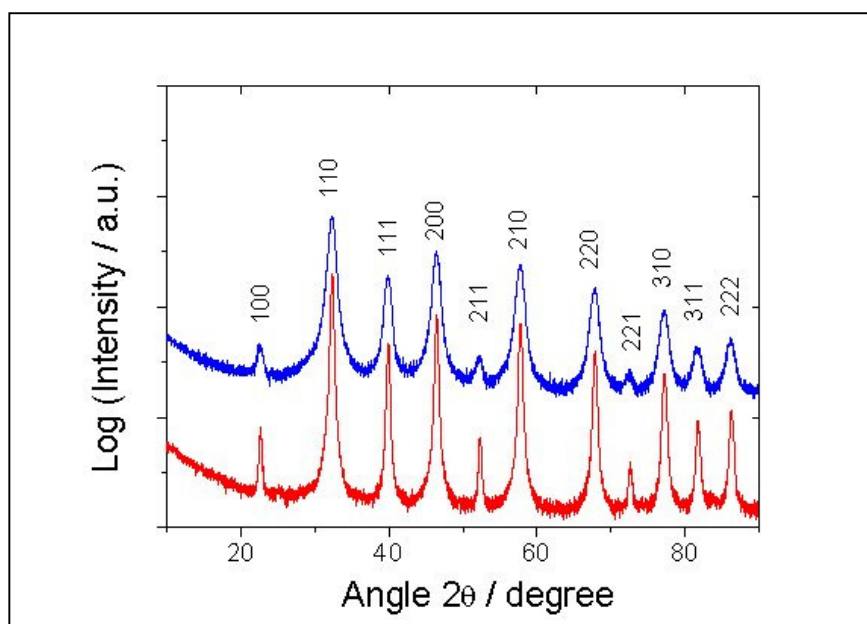


Figure 22 XRD patterns of undoped SrTiO₃, prepared according to method C, before (**blue**) and after (**red**) the calcination process. The broad peaks of the not-calcined powder indicate a much smaller grain size.

In order to dope the material with aliovalent cations, lanthanum isopropoxide, niobium ethoxide and iron (III) acetylacetonate were used as precursors and they were added at the same time of the Ti isopropoxide. In the case of La and Fe, the dopant

precursor was solid and it was thus first dissolved in benzyl alcohol. For our studies we chose a nominal doping of 0.6at% and 3at%. No pentanol was used for the synthesis of the doped powders.

The TEM analysis of the as-synthesized undoped powders (Figure 23) showed that the grain size is on average 5 nm, in agreement with ref. [125], irrespective of the solvent used (benzyl alcohol or a mixture of pentanol and benzyl alcohol). Although, the addition of pentanol does not affect the grain size, the TEM inspection suggests that the presence of pentanol can favour the agglomeration of the particles (see Figure 23b). In light of these findings the use of pentanol in the synthesis process was discarded.

The TGA plot shown in Figure 24 indicates that the powders contain organics up to about 600°C. The total mass loss is 14% for all samples, but the powders synthesized with pentanol are characterized by a further mass loss occurring between 500 and 700°C (red line in Figure 24). Therefore, the calcination temperature was set at 700°C for the powders synthesized only with benzyl alcohol and 800°C for the one synthesized with pentanol.

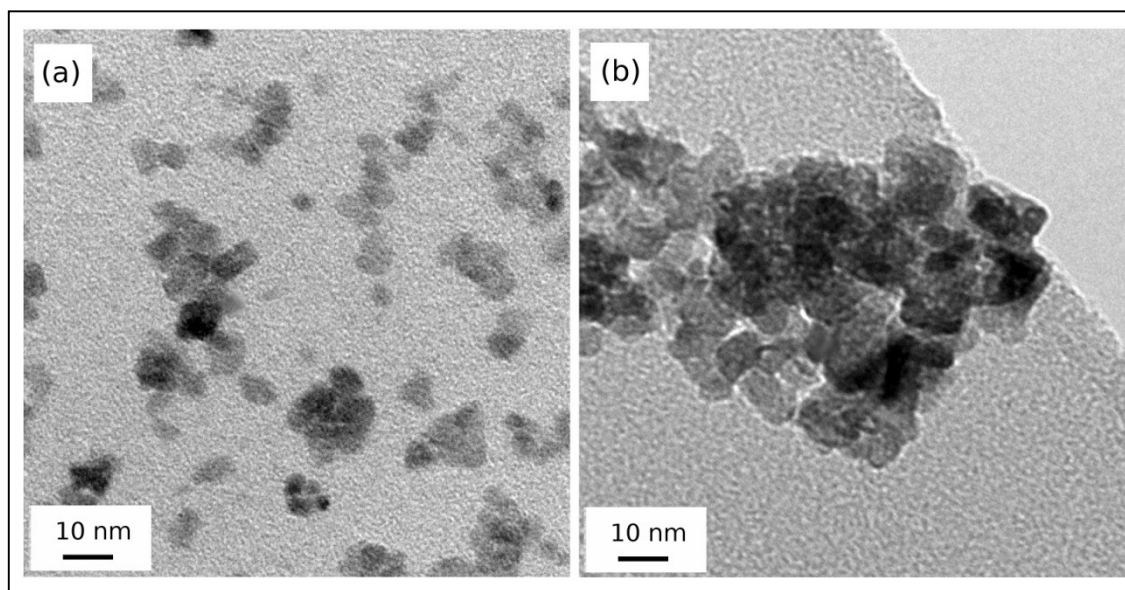


Figure 23 TEM micrographs of the as-synthesized powders (method C) before calcination. (a) synthesis with benzyl alcohol; (b) synthesis with benzyl alcohol and pentanol. The amorphous background of the micrographs is the carbon film of the TEM grid.

In Figure 24 also the TGA plot of the Fe-doped SrTiO₃ powder is illustrated. Notably, also in this case the major weight loss takes place below 600°C (although the overall mass loss is a bit less pronounced than for the other compositions). For this reason, also for the doped powders the calcination temperature was set at 700°C.

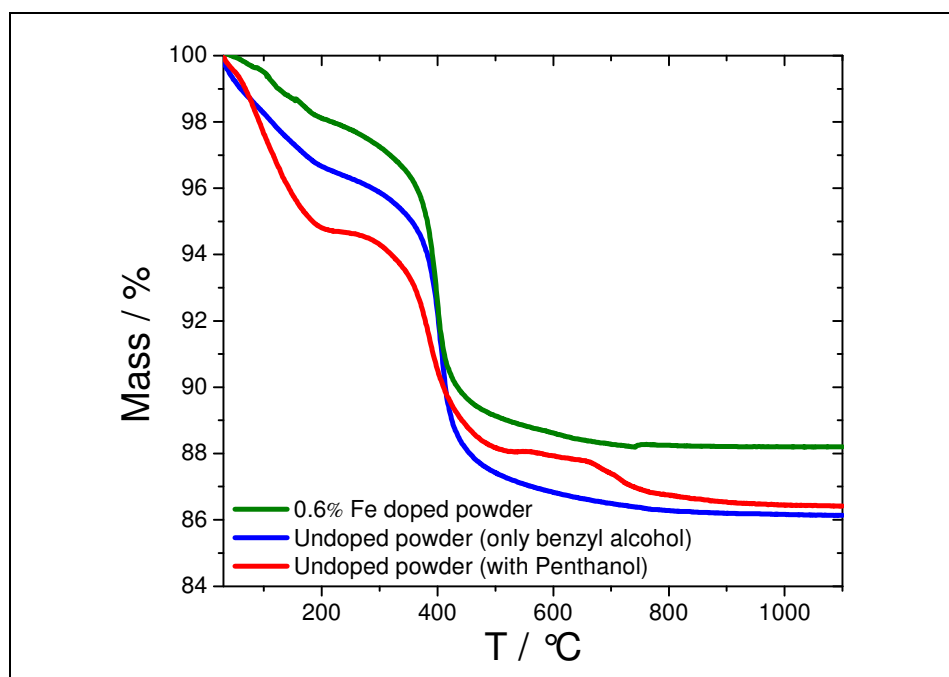


Figure 24 Thermogravimetric analysis of different samples prepared according to the solvothermal method: **(blue line)** undoped SrTiO_3 synthesized in benzyl alcohol; **(red line)** undoped SrTiO_3 synthesized in a solution of benzyl alcohol and pentanol; **(green line)** 0.6at% Fe-doped SrTiO_3 synthesized in benzyl alcohol. (heating rate: $5^\circ\text{C}/\text{min}$; Atmosphere: $20\%\text{O}_2$ and $80\%\text{N}_2$).

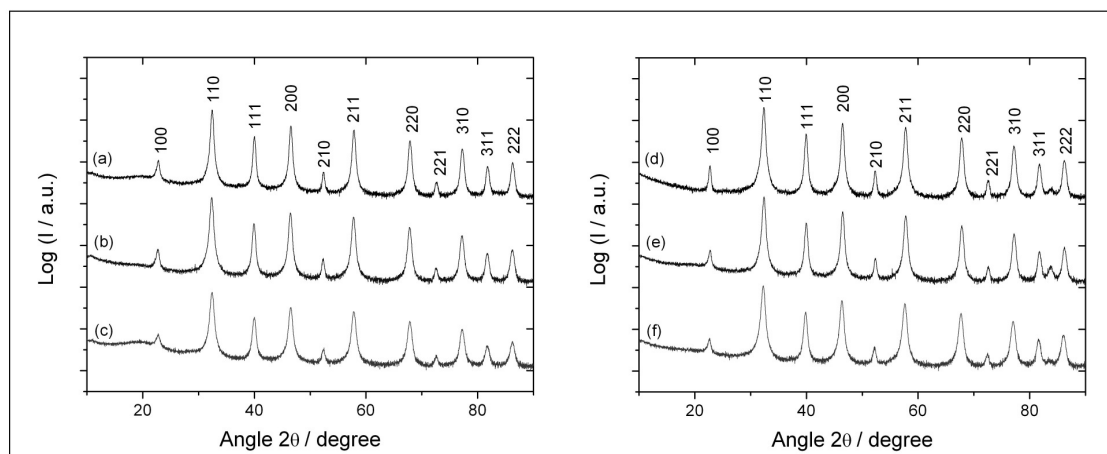


Figure 25 XRD patterns on the SrTiO_3 powders upon calcination: **(a)** undoped; **(b)** 0.6% Fe-doped; **(c)** 3% Fe-doped; **(d)** 0.6% La-doped; **(e)** 0.6% Nb-doped; **(f)** 3% Nb-doped. The weak signal between the directions (311) and (222) is an artifact due to the sample holder.

Table III Results of the Rietveld refinement on the XRD data: unit cell parameter (a), strain, grain size and residual ($R(F^2)$). Uncertainty is on the last digit for unit cell parameter; uncertainty for size and strain is around 10%.

Dopant	Nominal content	a	Grain size	Strain	$R(F^2)$
	[at%]	[Å]	[nm]	[%]	[%]
---	---	3.9056	18	0.02	1.9
La	0.6	3.9095	19	0.06	2.3
Nb	0.6	3.90972	17	0.04	2.1
Nb	3.0	3.9139	14	0.11	3.6
Fe	0.6	3.909	15	0.03	2.1
Fe	3.0	3.9105	13	0.15	2.2

Table IV Dopant content determined via ICP-OES of doped SrTiO₃ powders.

Dopant	Nominal content	Actual content
	[at%]	[at%]
La	0.6	0.62
Nb	0.6	0.56
Nb	3.0	2.93
Fe	0.6	0.56
Fe	3.0	2.88

X-ray diffraction patterns acquired upon calcination (Figure 25) confirmed that all nanocrystalline powders (undoped as well as doped) are characterized by a single phase and no crystalline phases other than SrTiO₃ form either during the synthesis or during the thermal treatment.

The values determined via the Rietveld refinement of the XRD data are reported in Table III. The values of the unit cell parameter a obtained are in perfect agreement with the typical values for undoped SrTiO₃ (3.9055 Å).^[78-80] Obviously, when the material is doped, the lattice parameter deviates from the original value of the undoped material as some cations of the original perovskite are substituted by the dopant. The variations in the lattice parameter are consistent with the relative ionic radii of dopant cations in the B-site ($Nb \approx Fe > Ti$).

The values of the average grain size calculated via Rietveld refinement range between 13 and 18 nm and are in good agreement with the TEM analysis upon

calcination (Figure 26). Furthermore, it was observed that the grain size becomes smaller on increasing the dopant content.

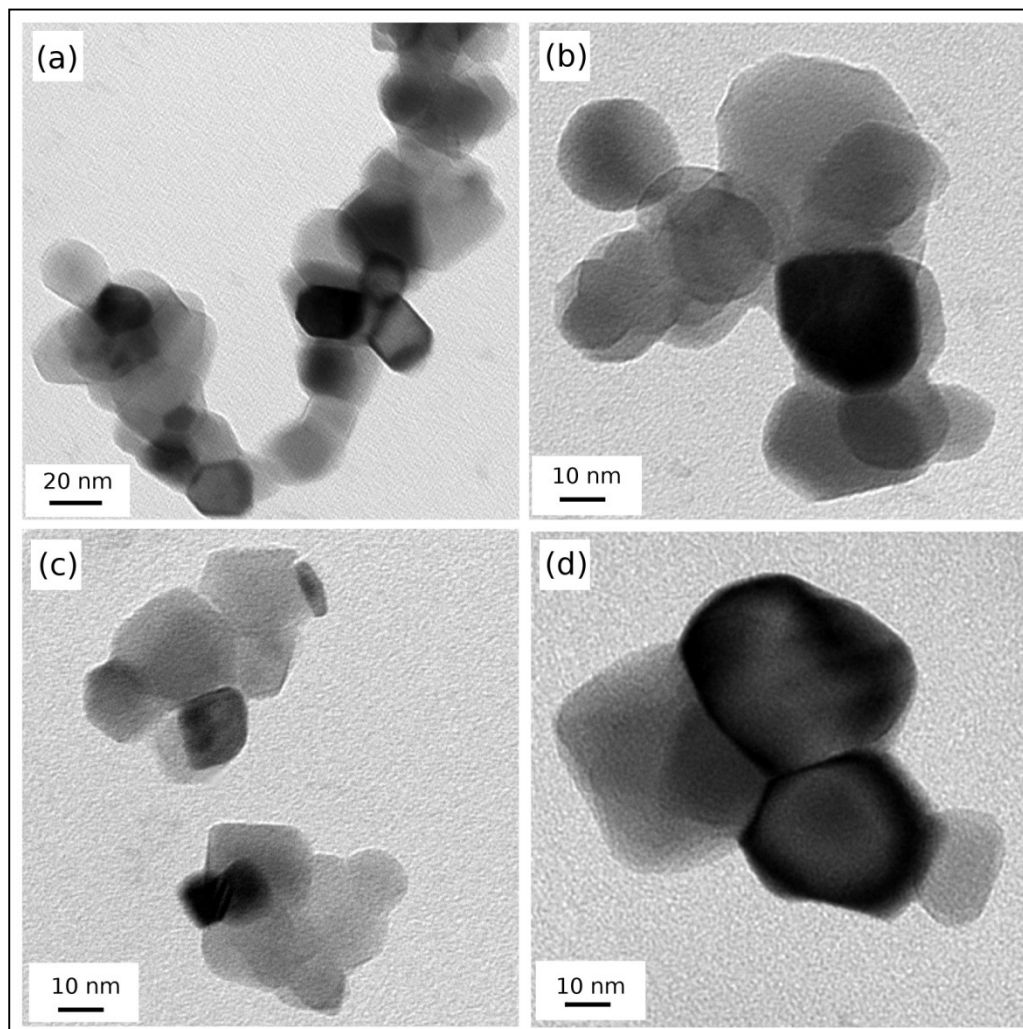


Figure 26 TEM micrographs of the nanocrystalline SrTiO_3 (a) undoped; (b) 0.6at% Nb-doped; (c) 0.6at% Fe-doped; (d) 0.6at% La-doped. The amorphous background of the micrographs is the carbon film of the TEM grid. Note that the magnification of (c) is different from the one of the other micrographs.

The concentration of the most abundant cations present in the undoped SrTiO_3 determined via ICP measurements are reported in Table V. It must be underlined here that Ba and Ca can substitute only Sr and since the valence of these three cations is the same, the presence of Ba and Ca does not affect the high temperature defect chemistry of the material. Thus, the only impurities observed which in principle could affect the effective dopant concentration are Al and B. These elements behave as acceptors in SrTiO_3 , but their amount is clearly negligible compared to the dopant amount.

EXAFS measurements performed on the Fe-doped samples confirmed the complete insertion of the Fe^{3+} cations in the B-site of the perovskite when the doping is homogenous. The detailed analysis of the EXAFS data is reported in section 4.4.

Table V Chemical analysis (ICP-OES) of most abundant cations present in SrTiO_3 prepared in the three different methods used in this work.

	Method A		Method B		Method C	
	[$\mu\text{g/g}$]	[at%]	[$\mu\text{g/g}$]	[at%]	[$\mu\text{g/g}$]	[at%]
Fe	< 25	0.0082	< 10	0.0033	< 10	0.0033
Ce	ca 125	0.0164	ca 150	0.0196	< 10	0.0013
Ba	ca 12	0.0016	ca 10	0.0013	ca 250	0.0334
Al	ca 25	0.0170	ca 30	0.0204	ca 10	0.0068
Ca	< 25	0.0115	ca 50	0.0229	ca 20	0.0092
Cr	< 30	0.0106	< 10	0.0035	< 10	0.0035
Mg	< 10	0.0076	< 2	0.0015	< 2	0.0015
Mn	< 5	0.0017	< 1	0.0003	< 5	0.0017
B					ca 5	0.0085

The actual dopant content (ICP measurements) of the doped powders is summarized in Table IV; the values are all very close to the nominal ones. Therefore, we can conclude that the dopants take part in the reaction and they sit in the perovskite structure, substituting either Sr or Ti.

Figure 26 shows the TEM micrographs of the different nanocrystalline SrTiO_3 powders upon calcination. The Fe-doped powders are characterized by a smaller grain size (~10 nm), whereas the other compositions exhibit an average grain size between 20 and 30 nm. This seems to suggest that the addition of Fe inhibits the grain growth during both the synthesis and the calcination. If one compares Figure 23a and Figure 26a (undoped powders), it is clear that the grains grow of about four times during the calcination process. No closed porosity was observed inside the grains.

ICP-OES measurements performed on the powder revealed a stoichiometry ratio Ti/Sr of 1.001 ± 0.025 .

4.1.4 Section conclusions

The solvothermal method (method C) has emerged to be the best synthesis technique for the preparation of nanocrystalline SrTiO₃. The main advantages related to this method concern the high reproducibility, the absence of intragranular porosity and the possibility of doping. Moreover the powders with the smallest grain size are indeed the ones produced according to this method.

On the other hand, it turned out that the co-precipitation and the combustion method are very difficult to reproduce on a routine basis. Apart from that, with the co-precipitation synthesis doping was not possible, since the dopant did not take part in the reaction.

4.2 Size effects on the conductivity of undoped SrTiO₃

In this section, the electrical properties of SrTiO₃ are described with particular emphasis on the conduction of the nanocrystalline material and how the grain size influences the transport of the charge carriers.

SrTiO₃ nanopowders were synthesized according to the co-precipitation method described in section 4.1.1 and sintered using the modified spark plasma sintering set up (Figure 12), which allowed to obtain pellets with a grain size between 50 nm (Figure 27a) and 80 nm (Figure 27b). As it can be seen in the inset of Figure 27b, due to the presence of intragranular closed porosity, the boundary spacing and, hence, the effective average grain size in the second sample is clearly lower and it lies in the range of 30 nm. According to ICP-OES analysis, these samples were found to contain ~0.02 at% of acceptor impurities (see Table V). Assuming a Mott-Schottky situation, for such an impurity content, $\lambda^* \cong 50$ nm at 544 °C according to Eq. 2.45 and, therefore, $2\lambda^*$ exceeds the average grain size.

The spectra of the nanocrystalline sample with the smallest effective grain size as well as the subsequently coarsened (microcrystalline) ceramic ($d_g \sim 1\mu\text{m}$) are represented in Figure 28.

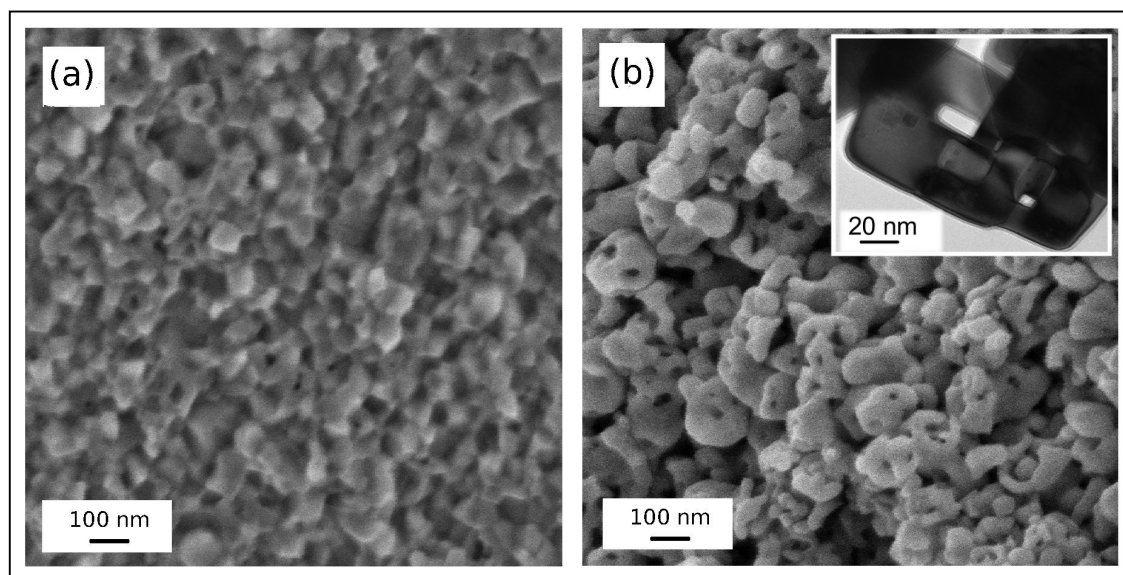


Figure 27 SEM micrographs of (a) nanocrystalline dense SrTiO₃ and (b) nanocrystalline SrTiO₃ with residual intragranular porosity. The TEM micrograph in the inset illustrates the presence of nanosized pores. Reprinted from ref. [161] with permission of John Wiley & Sons, Inc.

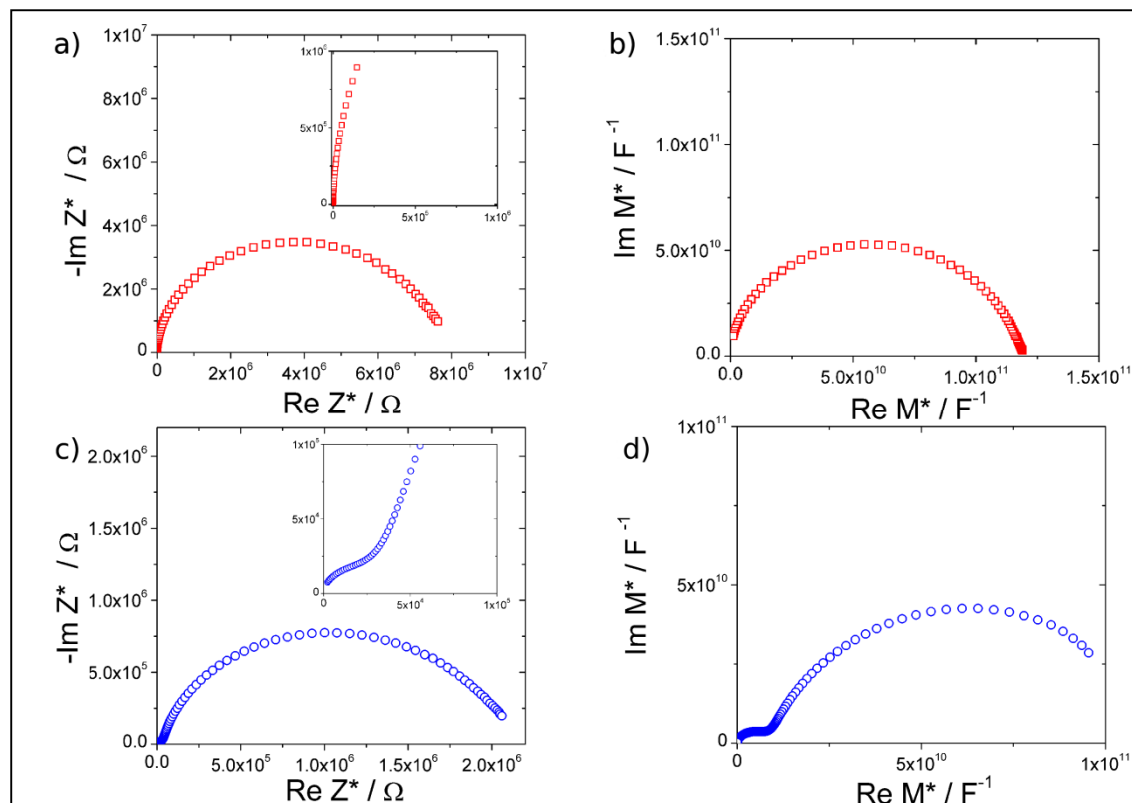


Figure 28 Impedance (Z^*) and Modulus (M^*) spectra acquired at 544°C and $P = 10^{-5}$ bar of the SrTiO_3 sample. (a) and (b) refer to the nanocrystalline material with effective grain size 30 nm whereas (c) and (d) refer to the coarsened sample. Note that the bulk contribution can be clearly recognized in (c) and (d), while (a) and (b) are characterized by one single semi-circle.

While the nanocrystalline material for which the grain size is smaller than $2\lambda^*$ is characterized by a single semi-circle (Figure 28a), a bulk arc in addition to the grain boundary signal can be observed in the microcrystalline one (Figure 28c). In the dielectric modulus plot, the high frequencies contributions appear on the right hand side of the spectrum and can be easily resolved. The dielectric modulus spectrum for the nanocrystalline sample depicted in Figure 28b (one semicircle) indicates that the absence of a second semicircle at high frequencies in the Z^* spectrum is not due to a poor resolution in the high frequency range but rather to the fact that there is no separate bulk contribution in the nanocrystalline material. This feature is an unambiguous argument only in the depletion mode, because in the accumulation mode, the disappearance of the bulk contribution might be due to the short-circuiting of the highly conductive GBs as in the case of CeO_2 reported by Kim and Maier.^[18] Indeed, (see also Figure 29) the bulk contributions for the microcrystalline sample are only detected in the regime of sufficiently high P .

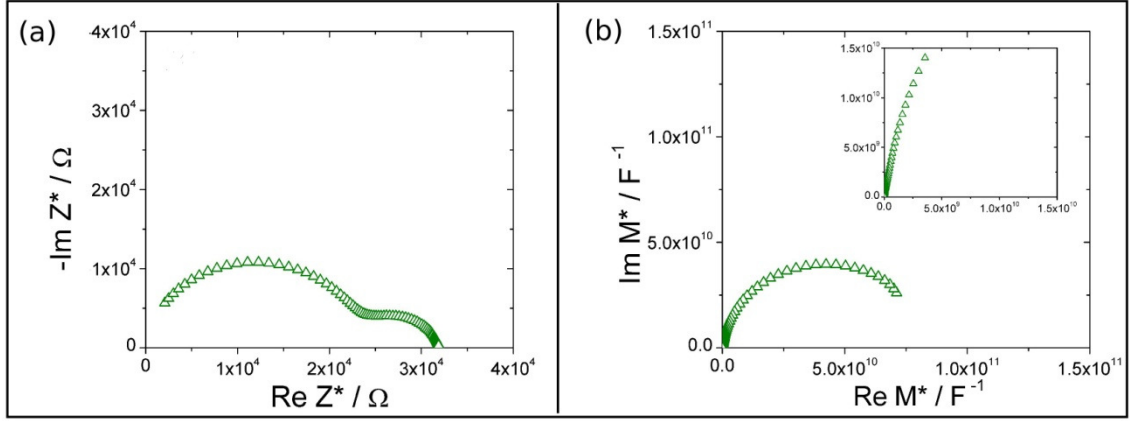


Figure 29 (a) Impedance Z^* and (b) dielectric modulus M^* spectra acquired from the microcrystalline sample at $T=544^\circ\text{C}$ and $P = 10^{-22}$ bar.

Figure 29 shows the impedance (Z^*) and dielectric modulus (M^*) spectra acquired from microcrystalline sample at $P = 10^{-22}$ bar. Notably, the spectra of the coarsened sample exhibit remarkable differences when acquired at high P ($P > 10^{-5}$ bar) or at low P ($P < 10^{-18}$ bar). At high P , the Z^* -spectrum is characterized by two semicircles assigned to the bulk ($\epsilon_R = 150$) and the GB contributions, respectively (capacitance ratio $C_{GB}/C_{bulk} \approx 10$). At low P , the Z^* -spectrum is characterized by an arc and a small semicircle, which are assigned to the parallel GB ($\epsilon_r \approx 150 \approx \epsilon_{bulk}$) and electrode contributions (capacitance ratio $C_e/C_{GB} \approx 200$), respectively (Figure 29). This latter assignment is supported also by the fact that the electrode contribution disappears in the dielectric modulus plot (Figure 29b), because its capacitance is much larger than the one of the GB and it is in series with it.^[148,149] This is exactly the same situation already observed in another n-type oxide,^[118] in which the highly conductive GBs short-circuit the bulk.

The activation energies of the conductivity were determined from the Arrhenius plot reported in Figure 30, according to Eq. 3.9. The values obtained for the nanostructured pellets at $P = 1$ bar are 1.20 eV for the sample with grain size 50 nm and 1.45 eV for the one with the smallest effective grain size. For the coarsened sample the activation energies determined for bulk and GBs were 0.8 eV and 1.53 eV respectively. These values are in agreement with previous studies on SrTiO_3 .^[38,60,73,162]

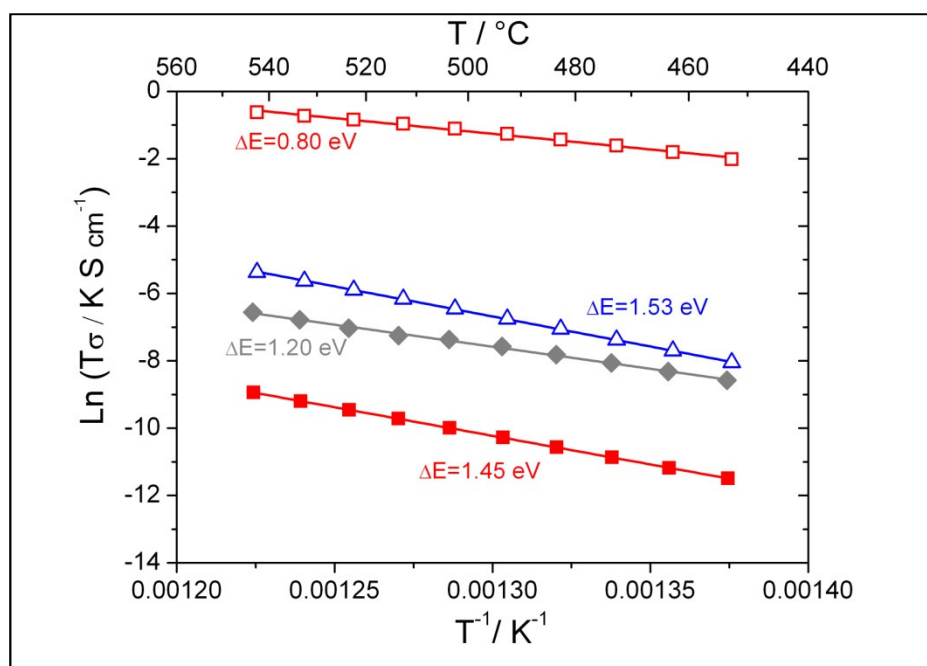


Figure 30 Arrhenius plot of the conductivity in the temperature range between 550 and 450°C. The symbols are assigned as follows: (**open red squares**) Bulk of the microcrystalline sample; (**open blue triangles**) GB contribution of the microcrystalline sample; (**grey diamonds**) nanocrystalline samples with average grain size of 50 nm; (**solid red squares**) nanocrystalline sample with effective grain size of 30 nm.

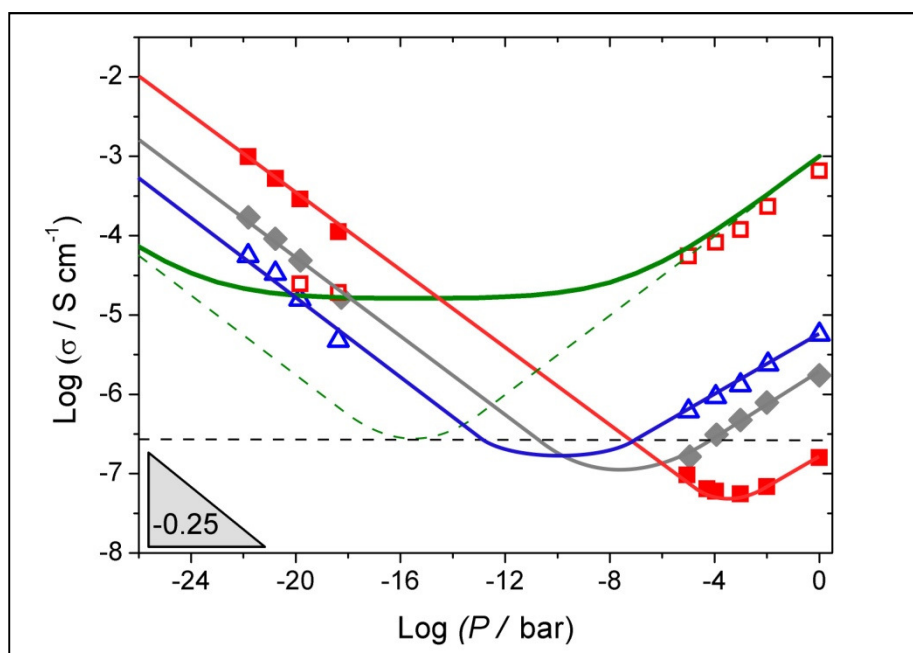


Figure 31 Oxygen partial pressure (P) dependence of the conductivity measured at 544°C. The symbols are assigned as follows: (**red open squares**) bulk of the microcrystalline SrTiO_3 obtained by coarsening the porous nanocrystalline sample; (**blue open triangles**) grain boundaries of the microcrystalline SrTiO_3 ; (**grey diamonds**) nanocrystalline SrTiO_3 ($d_g \sim 50$ nm); (**solid red squares**) nanocrystalline SrTiO_3 with the effective grain size of ~ 30 nm. The **continuous green line** illustrates the conductivity behaviour of the microcrystalline bulk calculated according to the defect chemistry of SrTiO_3 for $m = 0.01$ at% according to ref. [39]. The **dashed green line** shows the purely electronic conductivity, whose minimum corresponds to the value of the horizontal dashed line, defined by Eq. 2.60. Reproduced from ref. [161] with permission of John Wiley & Sons, Inc.

Figure 31 shows the oxygen partial pressure P dependence of the conductivity at 544°C. At high P , the power laws of the nanocrystalline samples are 0.20 and thus lower than the value of the microcrystalline bulk (0.22)^[23] indicating that $\Delta\phi_0$ is slightly P -dependent.^[68,163] A detailed analysis of the oxygen partial pressure dependence of the conductivity as a function of $\Delta\phi_0$ is presented in section 4.3.

The green line in Figure 31 represents the bulk conductivity at 544°C of SrTiO₃ with an acceptor content of 0.01 at%. It was determined according to the bulk defect chemistry model and the mobility data for the charge carriers of SrTiO₃ from ref. [39] reported in section 2.1.1. This curve describes very well the experimental data of the bulk of the coarsened sample (red open squares). The green line can be deconvoluted into an electronic conductivity itself (separately shown by the green dashed line) and a constant ionic conductivity σ_{ion} , which is predominant around the minimum. The electronic conductivity is composed of an n-type branch (σ_n) that is only seen at very low P and a p-type branch (σ_p) with a transition occurring at $\sim 10^{-16}$ bar. When the partial pressure is increased, then – in the n-type regime – the incorporated oxygen increasingly consumes electrons which contribute to the conduction (oxidation of Ti³⁺ to Ti⁴⁺). At higher P , the p-type conductivity dominates, which steeply increases with increasing P as the incorporated oxygen generates holes (oxidation of O²⁻ to O⁻).

At P_{min} , both n- and p-type conductivity assume the same value given by Eq. 2.60 ($\sigma = 2F\sqrt{\mu_n\mu_p K_B}$). It is worth noting here that this expression is independent of the impurity content and it is valid also in the fully mesoscopic range.

The bulk conductivity of the microcrystalline material obtained by coarsening the nanosized porous sample (open red squares in Figure 31) exhibits a behaviour very similar to the curve calculated according to the defect chemistry model (continuous green curve).

If one now considers the nanocrystalline sample with the smallest effective grain size, which exhibits the most remarkable results, it turns out that, compared to the coarsened sample, σ_p is depressed by more than 3 orders of magnitude while the n-type conductivity is enhanced by 2 orders of magnitude. The absence of any plateau region (the narrow smooth region around the minimum is due to summing σ_n and σ_p) in the nanocrystalline curves means that the ionic (oxygen vacancy) conductivity is depressed

by more than 3 orders of magnitude. Most impressive is the giant shift of the minimum towards higher partial pressures (by 12 orders of magnitude). All these features including this enormous shift of the minimum by 12 decades are a consequence of the grain size reduction and can be explained by the mesoscopic core-space charge model, described in section 2.3.

The behaviour in the space charge zone is completely different compared to the bulk. All the carrier concentrations are redistributed according to Eq. 2.35 and have to follow the space charge potential resulting from the positive core charge. Therefore, the hole concentration $p(x)$ is depressed by a factor $\kappa(x)$ (with $\kappa(x) = \exp(e\Delta\phi(x)/kT)$), $n(x)$ is enhanced by the same factor, while $v(x)$ is depressed even by $\kappa(x)^2$ (owing to the double charge of the oxygen vacancies).^[1] The situation is illustrated in Figure 32 (dashed lines) for the specific case of SrTiO₃.

As the material is in the mesoscopic regime, one can adopt the approximation of flat profiles in the space charge layer, which implies that $\Delta\phi(x) = \Delta\phi_0$ is constant within the space charge layer. Under this assumption, one can approximate the bulk concentrations with the concentrations directly adjacent to the core (i.e. at $x = 0$ and $\kappa_0 = \exp(e\Delta\phi_0/kT)$).^[9]

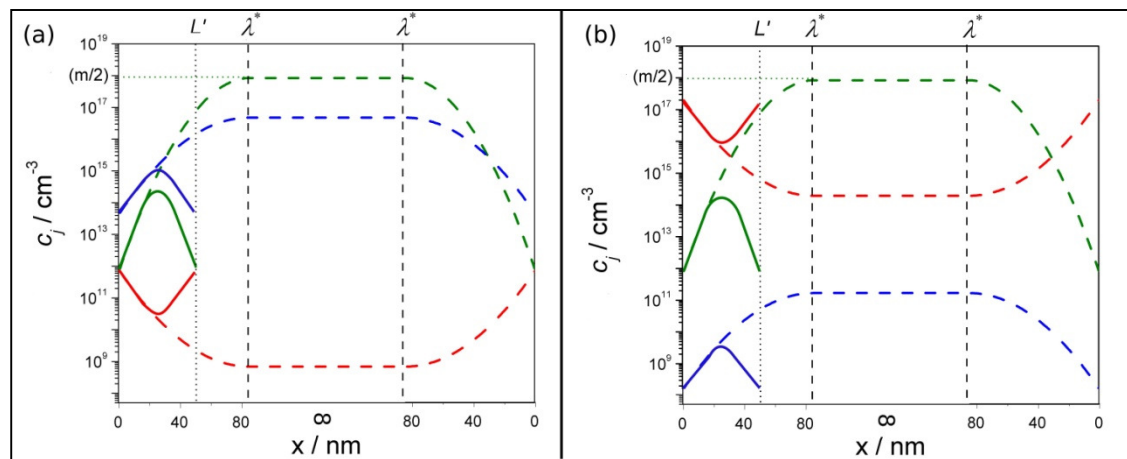


Figure 32 Calculated charge carrier profiles (a) in pure oxygen ($P = 1$ bar) and (b) for $P = 10^{-22}$ bar, for the 0.01 at% acceptor doped sample at $T = 544$ °C and $\Delta\phi_0 = 0.5$ V. Here the potential is assumed to be constant with grain size, although this may be only approximately correct, e.g. ref. [73]. The colours are assigned as follows: (blue) holes; (green) oxygen vacancies; (red) electrons. The dashed lines correspond to the coarsened sample ($d_g > \lambda^*$) while the solid lines represent the profiles of the nanocrystalline sample in the mesoscopic regime ($d_g < \lambda^*$) in which the space charge layers overlap. Reproduced from ref. [161] with permission of John Wiley & Sons, Inc.

The latter assumption is justified since it is known from the literature^[164] that the standard chemical potentials and, hence, the mass action constants in the space charge region are not perceptibly different from the bulk ones unless one approaches grain sizes of dimension of one or two lattice constants.

Notably, assuming flat concentration profiles in the SCL, from the combination of Eq.s 2.61 and 2.64,

$$P_{min}(L \rightarrow 0) = \kappa_0^A \cdot P_{min}(L \rightarrow \infty) \quad 4.1$$

results.

Therefore, $\Delta\phi_0$ can be determined from the ratio of P_{min} (nanocrystalline vs. bulk) yielding a value of 0.53 V for the nanocrystalline sample (30 nm effective grain size). This value is quite typical for SrTiO₃ ceramics and smaller than the one for the GB contribution in the coarsened sample (0.68 V, determined through Eq. 2.54).

In the mesoscopic situation, under the assumption of flat band profiles, Eq. 2.54 can be replaced by

$$\frac{\sigma_{bulk}}{\sigma_m} = \exp(ze\Delta\phi_0 / RT). \quad 4.2$$

with σ_m being the measured conductivity in the mesoscopic range.

Consequently, $\Delta\phi_0$ can be also determined from the ratio of the conductivities, yielding 0.58 V at $P = 1 \text{ bar}$, in the p-type regime ($z = 1$).

A further point of interest is the following: despite the huge variations of $\sigma_n(P)$ and $\sigma_p(P)$ on size reduction, the minimum conductivities should stay invariant and equal to $2F\sqrt{\mu_n\mu_p K_B}$ according to Eq. 2.60 (owing to the assumption $K_{B,\infty} = K_{B,0}$) This striking invariance, not only as far as size variation is concerned but also with respect to the impurity content, is approximately confirmed by Figure 31.

As already mentioned, this down-sizing effect is reversible as by coarsening the bulk defect chemistry is restored (red open symbols in Figure 31). Annihilation of grain boundaries leads to a homogenization of the charge carrier separation.

In the light of these considerations also the behaviour of the nanocrystalline sample with slightly larger grain size (50 nm) can be explained. As shown in Figure 31 (grey diamond symbols), for this sample the shift of P_{min} is not as large as (8 orders of magnitude instead of 12) in the sample with the smallest effective grain size. Also σ_p is

less depressed (2.5 orders of magnitude) while σ_n is enhanced only by half order of magnitude.

Section conclusions:

In this section, the conductivity of nanocrystalline SrTiO₃ was systematically studied as a function of oxygen partial pressure and compared with the properties of the coarsened material. Remarkably, the bulk contribution disappeared in the nanocrystalline material and the conduction properties were determined by the grain boundaries. The bulk properties can be restored by coarsening the sample, highlighting in this way that the effects observed are due to the different grain size. The modifications of n , p , and oxygen vacancy-type conduction, which were highlighted by the P -dependence of the conductivity, are due to the overlapping of the space charge layers when the grain size becomes smaller than the space charge layer width. These significant variations and in particular the shift of the p - n transition partial pressure by as many as 12 orders of magnitude can be understood in terms of the generalized ionic-electronic space charge model.

4.3 Space charge conductivity and space charge density

The P -dependence of the conductivity can be a very powerful way to determine the predominant conduction mechanism in a certain range of oxygen partial pressure P .^[165] SrTiO₃ is a particularly elegant example, since three different regimes (p-type, ionic and n-type) can be observed in the typical experimental conditions (P ranging between 1 and 10⁻²⁵ bar at 550°C), as reported in chapter 4.2.

In the p-type regime, the bulk conductivity is given by $\sigma(P,T) = p(P,T) \cdot e \cdot u_p(T)$. At a constant temperature, under the assumption that the migration enthalpy and therefore the charge carrier mobility is independent of P and taking into account Eq. 2.15, the P -dependence of the bulk conductivity can be written in the following form:

$$\frac{\partial \text{Log } \sigma_{bulk}}{\partial \text{Log } P} = \frac{1}{4} + \frac{1}{2} \frac{\partial \text{Log } m}{\partial \text{Log } P} \quad 4.3$$

with $m=2v$ being the acceptor concentration.^(*) If the acceptor is not redox-active $\partial \log m / \partial \log P$ vanishes, however is slightly negative if $m = [Fe_{Ti}'] < [Fe_{tot}] = \text{constant}$, as in the cases considered in this study.

Accordingly, in the n-type regime ($\sigma(P,T) = n(P,T) \cdot e \cdot \mu_n(T)$),

$$\frac{\partial \text{Log } \sigma_{bulk}}{\partial \text{Log } P} = -\frac{1}{4} - \frac{1}{2} \frac{\partial \text{Log } m}{\partial \text{Log } P} \quad 4.4$$

is obtained, by considering Eq. 2.12.

In the ionic range $\sigma(T) = 2 \cdot v \cdot e \cdot u_v(T) = m \cdot e \cdot u_v(T)$ is valid and, therefore, assuming that the mobility does not change with P ,

$$\frac{\partial \text{Log } \sigma_{bulk}}{\partial \text{Log } P} = 0 \quad 4.5$$

results.

For Fe-doped SrTiO₃, the term $(\partial \text{Log } m / \partial \text{Log } P)$ was calculated in the range $P = 1 - 10^{-5}$ bar from Eq.s 2.14 and 2.17 and it varies with T . Figure 33 illustrates how m varies as a function of temperature and the total dopant content in a few relevant cases. The term $(\partial \text{Log } m / \partial \text{Log } P)$ becomes more negative with increasing $[Fe]_{tot}$

^(*) Note that in the case of redox active dopants, m refers here only to the ionized acceptors ($[A_{Ti}']$) concentration at a certain P .

(Figure 33a). On the other hand, when $[Fe]_{tot}$ is kept constant, $[Fe'_T]$ increases with T but the slope does not change.

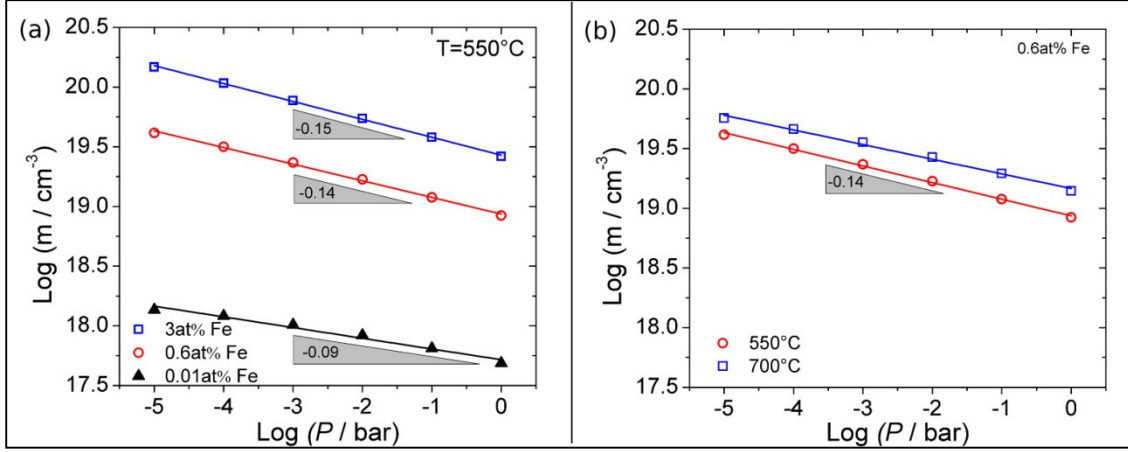


Figure 33 $Fe'_T(m)$ concentration as function of P (a) at constant T for different $[Fe]_{tot}$ and (b) at different T for $[Fe]_{tot} = 1.01 \cdot 10^{20} \text{ cm}^{-3}$ (0.6at% Fe).

The P -dependence in the space charge zones deserves a special consideration: According to the brick layer model of a polycrystalline material with grain size d_g , the conductivity in the space charge region is given by:^[26]

$$\sigma_{GB}^{\perp} = \frac{1}{2} \left(\frac{d_g}{Z_{GB}^{\perp}} \right) \quad 4.6$$

$$\sigma_{GB}^{\parallel} = 4 \left(\frac{Y_{GB}^{\parallel}}{d_g} \right) \quad 4.7$$

with Z_{GB}^{\perp} and Y_{GB}^{\parallel} being the resistance of the perpendicular boundaries and the conductance of the parallel ones, normalized with respect to the macroscopic coordinates. In the Mott-Schottky case, they are given by:^[26]

$$Z_{GB}^{\perp} = \frac{\lambda^*}{|z_j| e u_j} \frac{1}{2c_{j0} \ln(c_{j\infty} / c_{j0})} \quad 4.8$$

$$Y_{GB}^{\parallel} = \lambda^* |z_i| e u_i \frac{c_{i0}}{2 \ln(c_{i0} / c_{i\infty})}. \quad 4.9$$

For the determination of the P -dependence of the space charge conductivity, Eq.s 2.35 and 2.45 have to be used for the differentiation, yielding, for perpendicular boundaries in the p-type regime

$$\frac{\partial \text{Log} \sigma_{GB}^{\perp}}{\partial \text{Log} P} = \frac{1}{4} + \frac{\partial \text{Log} m}{\partial \text{Log} P} + \frac{1}{2} \frac{\partial \text{Log}(\Delta\phi_0)}{\partial \text{Log} P} - \frac{1}{2.303} \frac{\partial(e\Delta\phi_0/kT)}{\partial \text{Log} P}. \quad 4.10$$

On the other hand, for parallel boundaries, in which electrons are the dominating charge carriers, the P -dependence of the space charge conductivity is equal to:

$$\frac{\partial \text{Log} \sigma_{GB}^{\parallel}}{\partial \text{Log} P} = -\frac{1}{4} - \frac{\partial \text{Log} m}{\partial \text{Log} P} - \frac{1}{2} \frac{\partial \text{Log} \Delta\phi_0}{\partial \text{Log} P} + \frac{1}{2.303} \frac{\partial(e\Delta\phi_0/kT)}{\partial \text{Log} P}. \quad 4.11$$

In the latter equations, the term $(\partial \text{Log} \Delta\phi_0 / \partial \text{Log} P) = (\partial \Delta\phi_0 / \partial \text{Log} P) / \Delta\phi_0$ is negligible compared to $(\partial \Delta\phi_0 / \partial \text{Log} P) / kTe^{-1}$ as $|\Delta\phi_0| \gg kT / e$.

However, in order to understand the conduction properties in the space charge region, a more pertinent parameter to be considered is the surface density of the excess charge in the grain boundary core (Σ), which is directly determined by the defect concentration within the core of the grain boundaries and induces the charge carriers rearrangement in the space charge layers.

In the present section, we intend to consider the conductivity data presented in section 4.2 in order to examine (i) how Σ varies with P and (ii) whether the P dependence of Σ changes between the microcrystalline and nanocrystalline samples. Thus, the analysis presented in the following concerns undoped SrTiO₃ specimens with a net acceptor (Fe impurities) content of 0.01-0.02 at%. Please note also that the nanocrystalline sample has an average grain size of 50 nm (see grey diamonds in Figure 31 and Figure 34) and is in the mesoscopic situation (The space charge layer width is larger than half the grain size).

Taking into account the surface charge density in the GB core (Σ) in the Mott-Schottky approximation (Eq. 2.48) one can rewrite Eq.s 2.54, 4.2 and 4.11 as follows:

$$\frac{\sigma_{bulk}}{\sigma_{GB}^{\perp}} = \frac{\exp(z\Sigma^2 / 8\epsilon mRT)}{2z\Sigma^2 / 8\epsilon mRT}. \quad 4.12$$

In the case of flat band approximation, Eq. 4.2 becomes

$$\frac{\sigma_{bulk}}{\sigma_m} = \exp(z\Sigma^2 / 8\epsilon mRT). \quad 4.13$$

In addition, the P -dependence of the GB conductivity can be expressed with respect to the GB core charge density and Eq. 4.11 can be rewritten as

$$\frac{\partial \text{Log} \sigma_{GB}^{\perp}}{\partial \text{Log} P} \approx \frac{1}{4} + \frac{\partial \text{Log} m}{\partial \text{Log} P} - \frac{1}{18.4 \varepsilon_0 \varepsilon_r e k T} \cdot \left[\left(\frac{\partial \Sigma}{\partial \text{Log} P} \cdot \frac{2\Sigma}{m} \right) - \left(\frac{\partial m}{\partial \text{Log} P} \cdot \left(\frac{\Sigma}{m} \right)^2 \right) \right]. \quad 4.14$$

In the light of Eq. 4.12 and 4.13 one could directly determine the value of Σ from the conductivity value, if the acceptor content m is known.

It is important to note that Eq. 4.14 allows predicting the P dependence of the σ_{GB}^{\perp} in terms of Σ . Clearly, if the dopant content m is known, this is a rather easy task (under the Mott-Schottky approximation if the dopant is not redox active) that can be carried out by using Eq. 4.12 and 4.13).

However, the situation is more complex if the dopant is redox active as in the case of Fe-doped SrTiO₃ (see Eq. 2.16).

Hence, in such a situation, it is convenient to average Eq. 4.14 over the P -range considered:

$$\frac{\Delta \text{Log} \sigma_{GB}^{\perp}}{\Delta \text{Log} P} \approx \frac{1}{4} + \frac{\Delta \text{Log} m}{\Delta \text{Log} P} - \frac{1}{18.4 \varepsilon_0 \varepsilon_r e k T} \cdot \left[\left(\frac{\Delta \Sigma}{\Delta \text{Log} P} \cdot \frac{2\bar{\Sigma}}{\bar{m}} \right) - \left(\frac{\Delta m}{\Delta \text{Log} P} \cdot \left(\frac{\bar{\Sigma}}{\bar{m}} \right)^2 \right) \right]. \quad 4.15$$

where instead of considering the derivatives of the different quantities with respect to $\text{Log} P$, we take the finite changes of each quantity upon a finite variation of P and $\bar{\Sigma}$ as well as \bar{m} represent the average values within the P range considered.

Now, starting from (i) the iron concentration m in the samples (0.02 at%), (ii) the defect chemistry model by Denk and (iii) the characteristic value of $\Delta\phi_0$ for polycrystalline SrTiO₃ (which is approximately 0.70V[†] as determined in this study and according to previous studies^[64,73]) one can predict $\Delta \text{Log} \sigma_{GB}^{\perp} / \Delta \text{Log} P$.

For the case considered here, with P ranging between 1 and 10⁻⁵ bar, $\bar{\Sigma} = 3.28 \cdot 10^{-6} \text{ C} \cdot \text{cm}^{-2}$, $\bar{m} = 1.76 \cdot 10^{18} \text{ cm}^{-3}$ and $\partial \Sigma / \partial \text{Log} P = -3.55 \cdot 10^{-7}$ are obtained. By considering all the terms on the right side of Eq. 4.15,

$$\Delta \text{Log} \sigma_{GB}^{\perp} / \Delta \text{Log} P = 0.23 \quad 4.16$$

results.

[†] The variation of $\Delta\phi_0$ with P can be neglected.

On the other hand, in the n-type regime, the parallel boundaries are responsible of the conduction. At very low P , the variation of m can be neglected, since all Fe atoms are ionized. Therefore, considering Eq. 2.12, Eq. 4.15 can be reformulated as

$$\frac{\partial \log \sigma_{GB}^{\parallel}}{\partial \log P} = -\frac{1}{4} + \frac{2\Sigma}{18.4\varepsilon_0\varepsilon_r emkT} \frac{\partial \Sigma}{\partial \log P}. \quad 4.17$$

In the following, Eq. 4.15 and 4.17 are used (in the light of the conductivity data reported in section 4.2), in order to investigate the P -dependence of Σ for the microcrystalline and nanocrystalline ($d_g \sim 50nm$) samples.

Microcrystalline SrTiO₃

For the microcrystalline material, the P -dependence of σ_{bulk} determined experimentally is equal to 0.218 ± 0.012 (see Figure 34 and Table VI), which is very close to what is expected from theoretical consideration (Eq. 4.3). The deviation is due to the Fe ionization as expressed in Eq. 4.3. The actual P -dependence of the net acceptor content m , namely ionized Fe³⁺, can be determined from the experimental value of $\partial \log \sigma_{bulk} / \partial \log P$. In this case, $(\partial \log m / \partial \log P) = -0.06$ is obtained (Table VII). This value is slightly lower than the value predicted from the model developed by Denk *et al.* [39], which is equal to -0.10 (Table VII), and corresponds to a Fe content of 0.003 at%. This is clearly lower than what is indicated by the chemical analysis (0.02 at%). Notably, if we take into account also the standard deviation, $(\partial \log m / \partial \log P)$ varies between -0.04 and -0.08 , which still does not fit with the theoretical value of -0.10 . The remaining difference (which indicate that the Fe content in the grain interior is lower than 0.01-0.02 at%) can be explained with a slight Fe segregation at the GBs, which reduces the amount of m in the grain interior. Fe segregation is typical in microcrystalline SrTiO₃ due to the positive GB core and was already observed for example by Chiang *et al.* [72]

Table VI Values of the P -dependence of conductivity and of the surface charge density (in the high P -regime) at the GBs determined experimentally

		$\frac{\partial \text{Log } \sigma^{\perp}}{\partial \text{Log } P}$	$\frac{\partial \text{Log } \sigma^{\parallel}}{\partial \text{Log } P}$	$\frac{\partial \Sigma}{\partial \text{Log } P}$
Micro	Bulk	0.218±0.012		-3.68·10 ⁻⁷
	GB	0.196±0.007	-0.275±0.038	
Nano		0.205±0.011	-0.285±0.007	-2.64·10 ⁻⁷

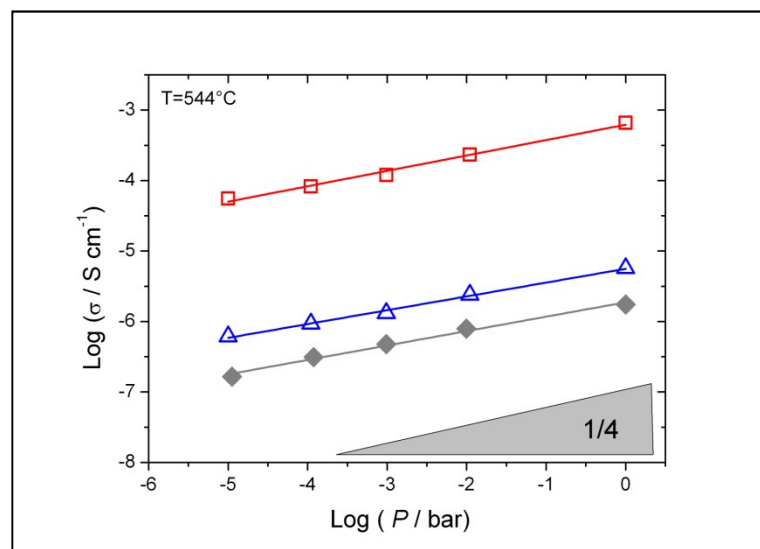


Figure 34 Detailed view of the P -dependence of the conductivity at $T=544^{\circ}\text{C}$ for oxidizing conditions given in Figure 31. The symbols are assigned as follows: **(grey diamonds)** nanocrystalline sample ($d_g \sim 50$ nm); **(open red squares)** bulk of the microcrystalline sample; **(blue triangles)** GB contribution of the microcrystalline sample. For the GB conductivity of the microcrystalline material, the conductivity was calculated considering the geometry of the sample. The values of the slopes are reported in Table VI.

Table VII P -dependence of m ; ^(a) from Eq.4.3 , ^(b) from Eq. 4.15.

		$\frac{\partial \text{Log } m}{\partial \text{Log } P}$
Denk <i>et al.</i> ^[39]		-0.10±0.01
Micro	Bulk	-0.06 ^(a)
	GB	-0.12 ^(b)

If we now consider the GB behaviour, we can determine $\Delta\phi_0$ by numerically solving Eq. 2.54 for the different P values, at which the conductivity was measured. At first, it is convenient to use Eq. 4.10, since Eq. 4.15 requires the knowledge of the exact value of m , which is actually not known. By plotting $\Delta\phi_0$ versus P (Figure 35), its P dependence can be determined, yielding to $\partial\Delta\phi_0/\partial\text{Log } P = -0.006 \text{ V}\cdot\text{bar}^{-1}$. This is consistent (at least qualitatively) with what was previously observed by Zhang *et al.* in slightly Fe-doped SrTiO_3 .^[163] By inserting the latter value in Eq. 4.10 and taking into consideration the experimental value $\partial\text{Log } \sigma_{GB}^{\perp} / \partial\text{Log } P = 0.196 \pm 0.007$ (Table VI), $\partial\text{Log } m / \partial\text{Log } P = -0.12$ (Table VII) is obtained. It is worth noting that this value is higher than the one calculated for the bulk, which corroborates the previous hypothesis of a slight Fe segregation at the grain boundaries, (under the assumption that Eq. 2.16 holds also in the boundary regions).

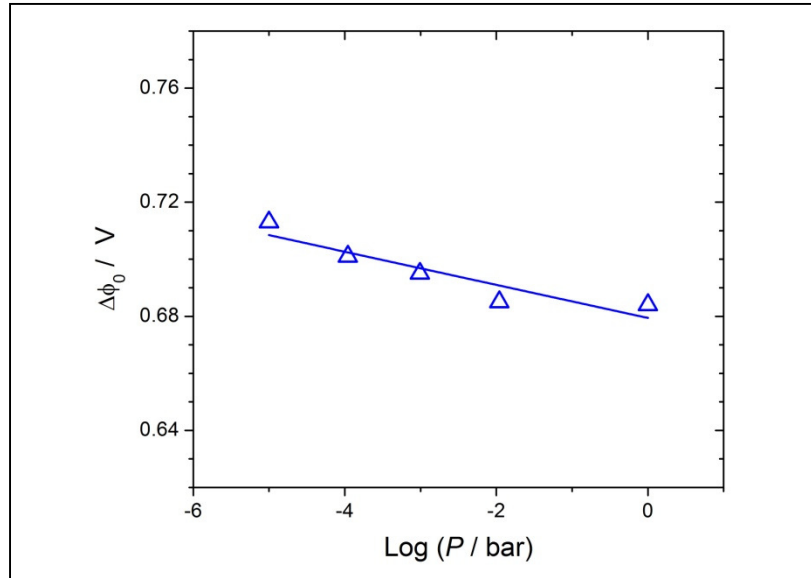


Figure 35 P -dependence of $\Delta\phi_0$ of the microcrystalline calculated according to Eq. 2.54.

From the experimental data, the surface charge density Σ at the GBs can be evaluated according to Eq. 2.48, considering a Fe content of 0.02 at%. The data are plotted in Figure 36. From these, one can recognize that $\partial\Sigma/\partial\text{Log}(P) < 0$ which indicates that the excess positive charge within the GB core diminishes with increasing P . If we now assign the excess positive charge to $V_o^{\bullet\bullet}$,^[68] then their surface density in the case of a core consisting of a single atomic layer varies from $6.99 \cdot 10^{12}$ to $1.27 \cdot 10^{13}$

cm^{-2} when P increases from 1 to 10^{-5} bar. This is consistent with oxygen ions leaving the grain boundary core when the environment becomes more reducing.

Nanocrystalline SrTiO_3

In this case, a flat concentration profile approximation can be assumed and thus Σ can be determined according to Eq. 4.13 for each P value considered. From this, it is possible to estimate Σ by taking into account the Fe ionization reaction, which in this case is assumed to be equal to the one obtained for the GBs of the microcrystalline material ($\partial \text{Log } m / \partial \text{Log } P = -0.12$). The resulting data are plotted in Figure 36, in which also the P dependence of Σ of the microcrystalline sample is shown for comparison.

It is evident that in both samples Σ decreases with increasing P . Notably, despite the similar tendency, two main differences can be recognized in the nanocrystalline sample compared with the microcrystalline one: (i) the charge density is lower, suggesting a lower excess positive charge (e.g. $V_{\text{O}}^{\bullet\bullet}$ concentration) in the GB core and (ii) the P dependence is less steep. Nonetheless it is instructive to consider the variation of Σ relative to the charge density in pure oxygen. Remarkably, although the starting values of Σ are clearly different ($1.74 \cdot 10^{-6}$ vs. $2.23 \cdot 10^{-6} \text{ C} \cdot \text{cm}^{-2}$), the change of Σ upon a reduction of 5 orders of magnitude of P is the same, namely an increase of 43%.

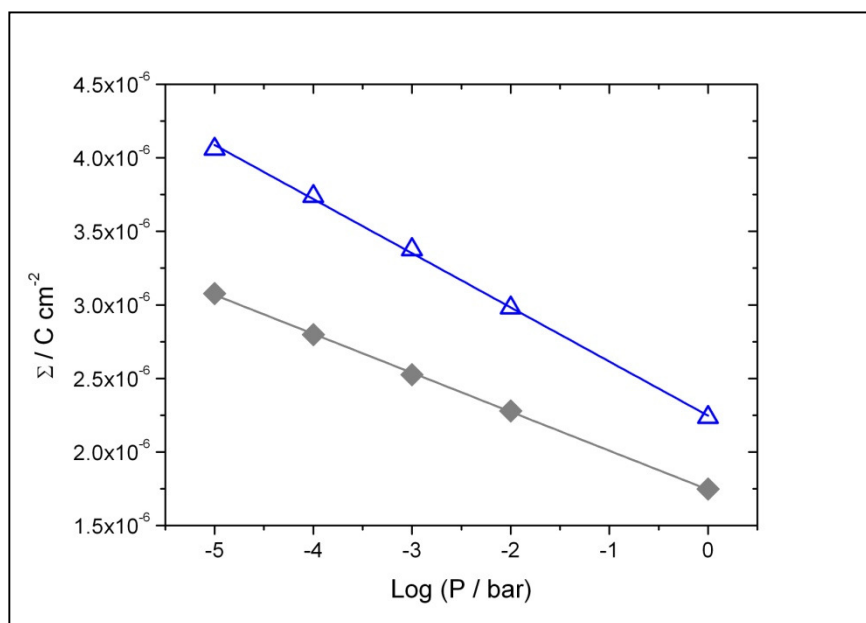


Figure 36 P dependence of the surface charge density Σ experimentally determined for both the microcrystalline (blue triangles) and nanocrystalline samples (grey diamonds). The values of the slopes are reported in Table VI.

Moreover, it is useful to consider the variation of Σ relative to the charge density $\partial\Sigma/(\Sigma \cdot \partial\text{Log } P)$. Note that

$$\frac{\partial\Sigma}{\Sigma \cdot \partial\text{Log}(p\text{O}_2)} = \frac{\partial\text{Log}\Sigma}{\partial\text{Log}(p\text{O}_2)} = s. \quad 4.18$$

which – if we assign this change of Σ to the variation of the $V_{\text{O}}^{\bullet\bullet}$ concentration in the GB core – represent a power law that is rather typical for bulk defect chemistry.

Remarkably, although the starting values of Σ are different, $1.74 \cdot 10^{-6}$ vs. $2.23 \cdot 10^{-6} \text{ C} \cdot \text{cm}^{-2}$ for the nanocrystalline and the microcrystalline sample respectively, $\partial\text{Log}\Sigma/\partial\text{Log } P$ is a constant with a value which is the same (about -0.05 , see Figure 37) for both samples.

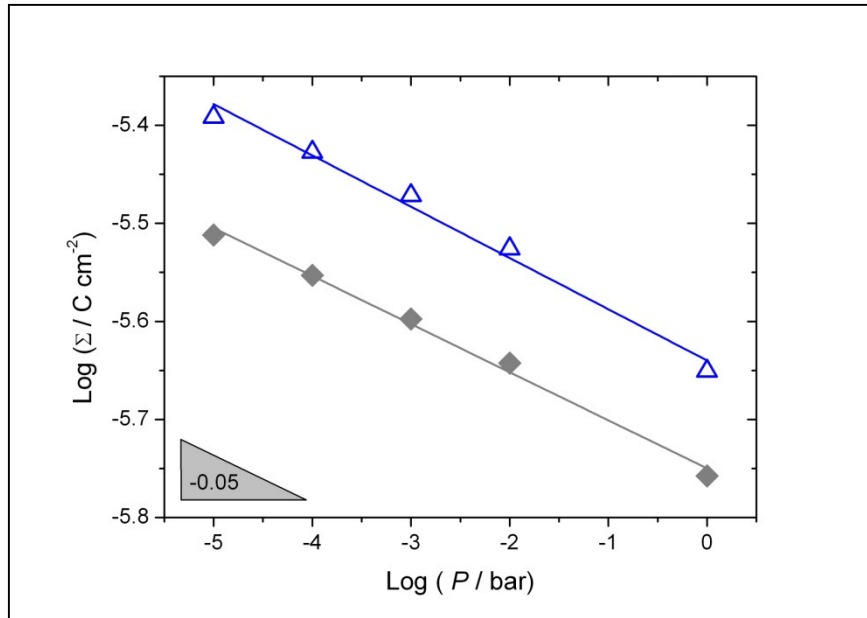


Figure 37 Logarithmic plot of Σ versus P . (Grey diamonds) nanocrystalline sample; (blue triangles) microcrystalline sample.

If one now takes into consideration the n-type conduction regime, $\partial\log\sigma_{GB}^{\parallel}/\partial\log P$ was experimentally determined to be equal to -0.28 for both the nanocrystalline (as well as the microcrystalline) materials. The deviation from -0.25 (see 4.17) is an evidence that $(\partial\Sigma/\partial\text{Log}P) < 0$, since we can exclude Σ to be negative as in the n-type regime the overall conductivity of the sample is determined by the parallel grain boundaries.[‡] This means that Σ decreases while increasing P .

[‡] If Σ were negative, the GBs would be blocking.

From the experimental data, the term $2\bar{\Sigma} \cdot (\partial\Sigma / \partial \text{Log}P) = -7.0 \cdot 10^{-14} \text{ C}^2 \cdot \text{cm}^{-4} \cdot \text{bar}^{-1}$ can be calculated. If we now take the same value of $\partial\Sigma / \partial \text{Log}P$ of the p-type regime, $\bar{\Sigma} = -1.62 \cdot 10^{-7} \text{ C} \cdot \text{cm}^{-2}$ results, which is one order of magnitude lower than under oxidizing conditions. This is obviously not possible as $\bar{\Sigma} \geq 3 \cdot 10^{-6} \text{ C} \cdot \text{cm}^{-2}$. Therefore, the oxygen partial pressure dependence of $\bar{\Sigma}$ in the n-type case is negative but less steep than in the p-type situation. This might suggest that with decreasing P the extraction of oxygen ions from the GB core become progressively less favourable.

Section conclusions:

In this part, a systematic investigation of the variation of the grain boundary core charge density Σ as a function of the oxygen partial pressure has been carried out. Such an analysis is based on the general space charge model, which enables to correlate the results of the conductivity measurements (impedance spectroscopy) with Σ . The results indicate that, irrespective of the average grain size, Σ decreases with increasing P , which corroborate the hypothesis that the excess positive charge of the GB core results from the presence of oxygen vacancies, which are filled when P increases.

In addition, it is found that compared to the microcrystalline sample, in the nanocrystalline SrTiO₃, (i) the charge density is lower but (ii) $\partial \text{Log}\Sigma / \partial \text{Log}(p\text{O}_2)$ is the same for both systems and equal to $-0.05 \text{ C} \cdot \text{cm}^{-2} \cdot \text{bar}^{-1}$. This suggests that the stoichiometry of the GB core is different between micro and the nanocrystalline material. Remarkably, it has been found that the percentage change of the oxygen vacancies concentration in the GB core is the same independently of the grain size.^[166]

4.4 Grain boundary defect chemistry of Fe-doped SrTiO₃

In the light of the results reported in the previous sections, the investigation of the electrical conduction properties in the mesoscopic regime also for doped SrTiO₃ (with possibly even smaller grain size) has become extremely attractive. In this chapter the results on the acceptor (Fe) doped material are reported.[§] Since the dopant distribution can play a fundamental role in the determination of the final properties of the material, two ways of doping have been employed in this context. The first consisted of the conventional homogenous doping, in which Fe was added in stoichiometric amount during the synthesis process and substitutes Ti on the B-site of the perovskite. In this way, one obtains a homogenous distribution of the dopant throughout the whole grain. However, doping can also be used in order to intentionally modify the local situation at the grain boundaries. This situation will be referred as *grain boundary (GB) decoration*. In this case, the goal was to tailor the GB properties of the material, which control the overall charge transport at the nanoscale through a charge carriers rearrangement in the space charge layer. If for example the charge core becomes negatively charged, then one would expect an enrichment of positive charges in the space charge region, with a consequent increase of the ionic conductivity when the material is in the mesoscopic regime.

Only a few experimental studies have explicitly addressed this aspect so far. In SrTiO₃ the addition of niobium at the GBs allowed to tailor the microstructure of the final sintered ceramic,^[167] but lead to a decrease of the p-type conductivity in oxidizing conditions.^[105] In another nanostructured mixed conducting oxide, i.e. cerium dioxide, it has been shown that the segregation of transition metals at the GBs (induced via long-term annealing at high temperatures) resulted in the reduction of GB resistivities,^[168] whereas the addition of boron at the GBs via liquid phase sintering in nanocrystalline CeO₂ increased the GB electronic conductivity.^[169] Moreover, the presence of acceptors (Ni²⁺ and Gd³⁺) at the grain boundaries (as well as their diffusion towards the grain interior) generated a drop of the electronic conductivity, which was ascribed to a decrease of the space charge potential.^[170] The grain boundary decoration has been also performed systematically for CeO₂ and the results are reported in the appendix of this

[§] Please note that here the Fe content is not due to impurities, but Fe was deliberately added during the synthesis process.

work. In that case, it was observed that the dopant partially diffused during the traditional sintering (800°C for 30 minutes) towards the centre of the grain. As a consequence of such a diffusion process (which at relatively low temperatures involved a thin region adjacent to the grain boundaries), a highly doped zone adjacent to the GBs was created, which acted as a preferential pathway for the ionic transport.

The solvothermal synthesis of the homogeneously doped powder was described in chapter 4.1, whereas the grain boundary decoration was achieved by adding the undoped nanocrystalline powder to a solution in which $\text{Fe}(\text{NO}_3)_3 \cdot 9\text{H}_2\text{O}$ (purity = 99.99%, Aldrich) was dissolved, followed by drying in the rotary evaporator and calcination at 450°C for 5 hours. In this way, Fe (3at%) was not homogeneously dispersed within the whole grain, but located only on the surface, with the aim of locally doping the GBs of the sintered sample. The powders were sintered via SPS at 750°C for five minutes, while applying a pressure 350 MPa.

Four compositions were considered in this context for the nanocrystalline samples, i.e. (i) undoped prepared via solvothermal synthesis which is used as reference, (ii) 0.6at% homogenous, (iii) 3at% homogenous, (iv) 3at% decorated.

The conductivity measurements performed via impedance spectroscopy were implemented with X-ray absorption fine structure (EXAFS), in order to verify (i) whether Fe entered the perovskite structure upon homogenous doping and (ii) what is the Fe environment in the case of the grain boundaries decoration. The latter experiments provided pieces of information which are crucial for understanding the electrical conduction properties of this nanocrystalline material.

The results of the EXAFS analysis are summarized in Table VIII, Table IX and Table X. The experimental EXAFS data referring to the Fe K-edge of the homogeneously doped sample were modelled assuming that Fe atoms substitute Ti atoms in the perovskite B-site. As illustrated in Figure 38a-b, the modelled structure reproduces well the experimental data, confirming the complete insertion of the Fe^{3+} cations in the B-site of the perovskite structure, confirming the results of the XRD analysis on the powders reported in section 4.1. It is worth noting that (i) as it is expected from tabulated ionic radii, the Fe-O and Fe-Sr distances (Table IX) are slightly longer than the corresponding Ti-O and Ti-Sr distances (Table VIII) and (ii) on the other hand, the Fe-Ti distance (Table IX) is about 0.04 Å shorter than the Ti-Ti distance (Table VIII). All the disorder factors around Fe^{3+} are comparable in magnitude

with those around Ti^{4+} , due to the good size matching between host and dopant cations, and demonstrating the smooth insertion of the dopant.

Table VIII Results of the EXAFS analysis on the Ti K-edge for undoped and doped samples (powders and sintered pellets): σ^2 is the disorder factor while R is the interatomic distance. Uncertainty is given on the last digit.

Ti K-edge	6 x Ti-O		8 x Ti-Sr		6 x Ti-Ti	
	R [Å]	σ^2 [10^{-3}Å^2]	R [Å]	σ^2 [10^{-3}Å^2]	R [Å]	σ^2 [10^{-3}Å^2]
Undoped Powder	1.96	7.6	3.36	7.8	3.94	2.6
Undoped Sintered	1.96	7.3	3.36	7.6	3.94	2.0
Fe 3% Hom Powder	1.95	8.2	3.36	8.1	3.94	1.7
Fe 3% Hom Sintered	1.96	7.8	3.37	8.1	3.93	1.6
Fe 3% Dec Powder	1.96	6.9	3.37	7.5	3.92	1.6
Fe 3% Dec Sintered	1.96	6.5	3.37	7.5	3.92	1.7

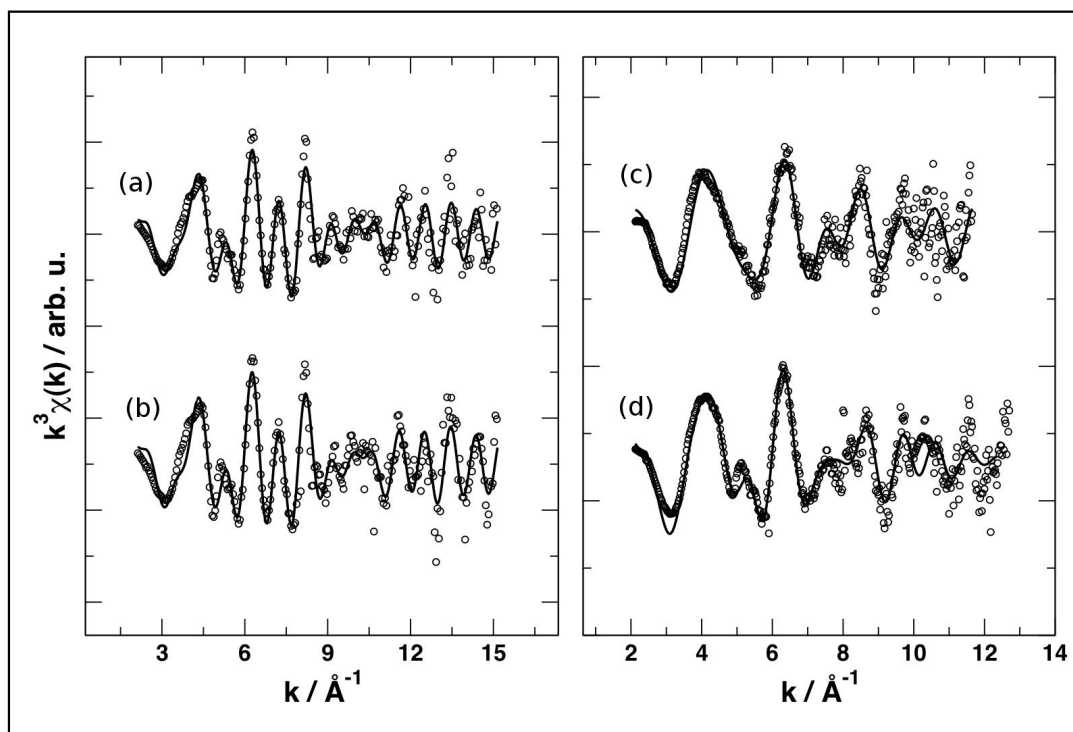
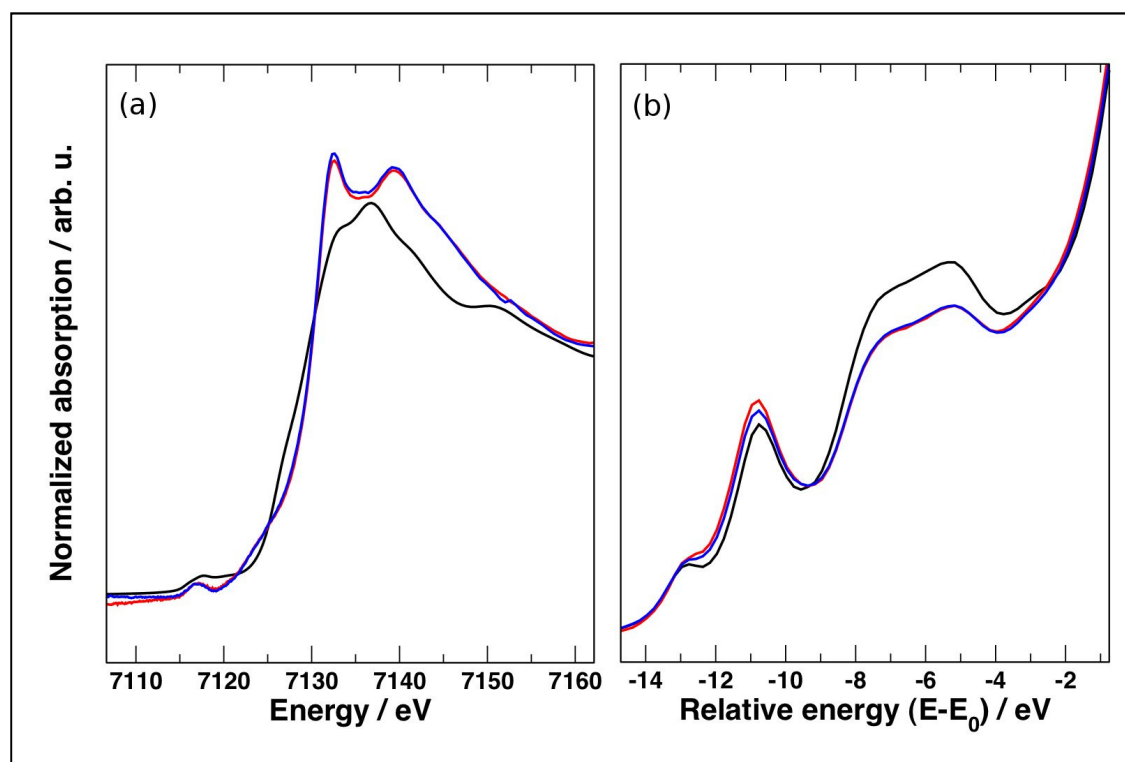


Figure 38 EXAFS data (circles) and best fitting (line) on the Fe K-edge. (a) homogeneously 3 at% Fe-doped SrTiO_3 powder; (b) homogeneously 3 at% Fe-doped SrTiO_3 sintered pellet. (c) decorated 3 at% Fe-doped SrTiO_3 powder; (d) decorated 3 at% Fe-doped SrTiO_3 sintered pellet.

Table IX Results of the EXAFS analysis on the Fe K-edge for doped samples (powder and sintered pellet): σ^2 is the disorder factor while R is the interatomic distance. Uncertainty is given on the last digit.

Fe K-edge	6 x Fe-O		8 x Fe-Sr		6 x Fe-Ti	
	R [Å]	σ^2 [10^{-3} Å ²]	R [Å]	σ^2 [10^{-3} Å ²]	R [Å]	σ^2 [10^{-3} Å ²]
Fe 3% Hom Powder	1.99	8.4	3.40	9.3	3.90	5.8
Fe 3% Hom Sintered	1.99	7.4	3.40	8.4	3.90	6.0

**Figure 39** Normalized XANES spectra on the Fe K-edge. (a) Fe₂O₃ (black), homogeneously 3 at% Fe-doped SrTiO₃ powder (red) and sintered pellet (blue). (b) Enlargement of the pre-edge region in the XANES spectra on the Ti K-edge of undoped SrTiO₃ (black), homogeneously 3 at% Fe-doped SrTiO₃ powder (red) and sintered pellet (blue).

An independent confirmation of the insertion of Fe in the SrTiO₃ lattice comes from the analysis of the X-ray absorption near edge structure (XANES) of the doped samples, which differ sharply from Fe₂O₃ used here as reference (Figure 39a). The dopant insertion has also a small effect on the pre-edge features of the Ti K-edge, as a result of the distortion of the TiO₆ units neighbouring the dopant sites (see Figure 39b).

Regarding the Fe-decorated sample, the XANES features of the Fe K-edge show very close resemblance between the Fe-decorated SrTiO₃ powder and Fe₂O₃ (see

Figure 40a). The Fe-decorated sintered pellet, while still being substantially similar to Fe_2O_3 , also shows features that are typical of Fe^{3+} in the perovskite B-site (for instance, the peak at 7132 eV, and the inflexion point shift to higher energies). These are shown in Figure 40b by comparison with the Fe-doped SrTiO_3 pellet whose Fe dopant atoms reside in the perovskite B-site.

Therefore, one can conclude that during the sintering process of the decorated powders, a fraction of the Fe atoms diffuses partially inside the grain interior (bulk), while the remaining atoms are remain outside the grains coordinated similarly to Fe_2O_3 .

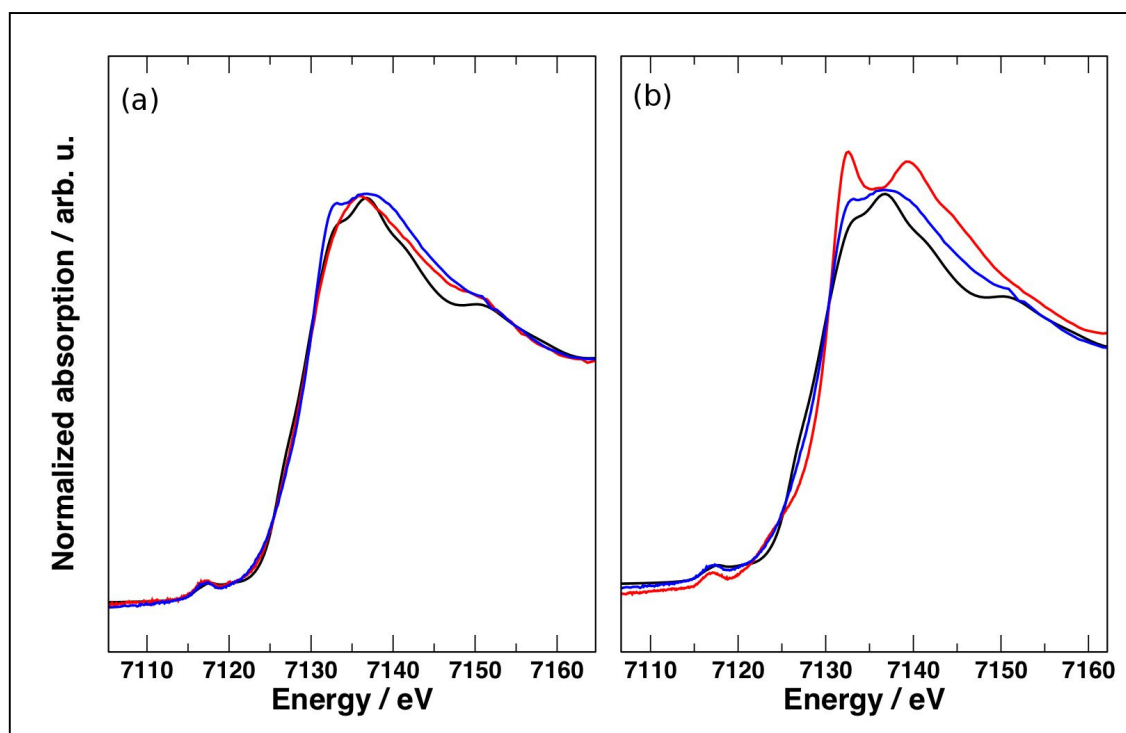


Figure 40 Normalized XANES spectra collected on the Fe K-edge. (a) reference Fe_2O_3 (black), Fe-decorated SrTiO_3 powder (red), Fe-decorated SrTiO_3 sintered pellet (blue). (b) reference Fe_2O_3 (black), Fe-doped SrTiO_3 sintered pellet (red), Fe-decorated SrTiO_3 sintered pellet (blue).

The results of the XANES analysis on the Fe K-edge are confirmed by EXAFS: remarkably, the data of the Fe-decorated sintered pellet cannot be modelled by simply considering Fe dopant atoms placed in the B-site of the SrTiO_3 lattice, as it is also evident from the differences in the raw EXAFS data between homogeneously doped and decorated samples, shown in Figure 38. For the Fe-decorated powder, they are satisfactorily reproduced by a local environment that resembles Fe_2O_3 . Despite the limited signal-to-noise ratio, it is possible to recognize unequivocally the Fe-Fe

contributions, appearing at much shorter distances than a possible Fe-Ti contribution (see Figure 41a).

In the Fe-decorated sintered pellet, the Fe-Fe signals typical of Fe₂O₃ are still very important, but additional contributions due to Fe-Sr and Fe-Ti correlations are visible in the Fourier-Transform plot up to 4 Å (Figure 41b). It is worth noting here that due to the coexistence of two different local environments (which are averaged during the collection of the experimental signal), the number of fitting parameters is larger than for the fitting of the experimental data shown previously. This implies that, in this case, the results reported in Table X should be considered as semiquantitative, with a rather large uncertainty. Nevertheless, the magnitude of the Fe-Sr and Fe-Ti signals allows for a rough estimation of the Fe atomic fraction still present as Fe₂O₃ to be about 50% of the total iron amount.

Table X Results of the EXAFS analysis on the Fe K-edge. Multiplicity of Fe-Fe distances was weighed by 0.5 in sintered sample, to account for local environment averaging between atoms in the SrTiO₃ perovskite lattice and segregated atoms.

Fe K-edge	3 at% Fe-decorated powder		3 at% Fe-decorated sintered	
	R [Å]	σ^2 [10 ⁻³ Å ²]	R [Å]	σ^2 [10 ⁻³ Å ²]
6 x Fe-O	1.99	10	1.99	13
1 x Fe-Fe	2.91	3	2.97	5
3 x Fe-Fe	3.05	9	3.05	9
3 x Fe-Fe	3.39	15	3.18	18
4 x Fe-Sr	--	--	3.30	20
3 x Fe-Ti	--	--	3.92	12

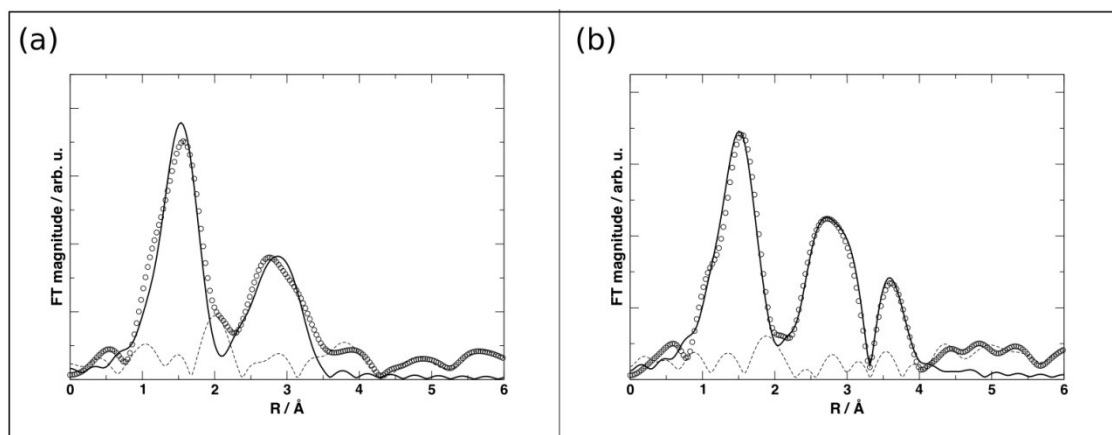


Figure 41 (a) Fourier transform (FT) EXAFS data (circles), best fit (thick line) and residual (dashes) of (a) Fe-decorated SrTiO₃ powder. (b) of Fe-decorated SrTiO₃ sintered pellet.

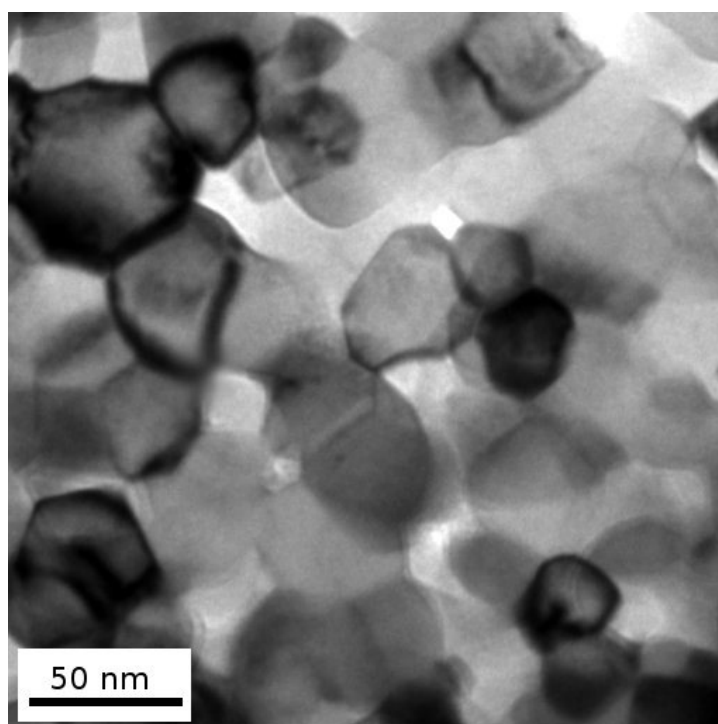


Figure 42 TEM micrograph of the nanocrystalline 3at% Fe homogenous sample. The grain size is approximately 30 nm.

A TEM study was also performed in order to investigate the microstructure of the 3at% Fe-doped SrTiO₃. It was observed that the final grain size (d_g) is approximately 30 nm.

A systematic EDX study was performed on the homogeneously 3 at% doped sample in order to investigate the iron distribution throughout. For this purpose, EDX spectra were recorded from an area of $2 \times 3 \text{ nm}^2$ of the GBs and in the centre of the adjacent grains.

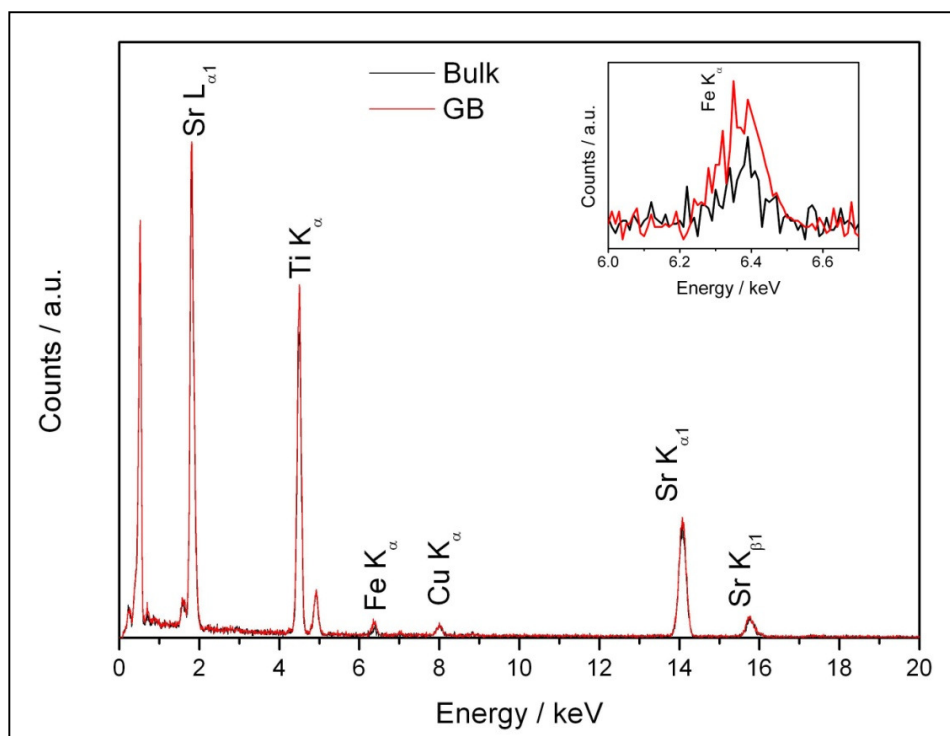


Figure 43 EDX spectra acquired at a grain boundary (red) and in the center of the adjacent grain (black). The Cu K_α peak is due to the sample holder. The spectra have been acquired over a window of 2 x 3 nm².

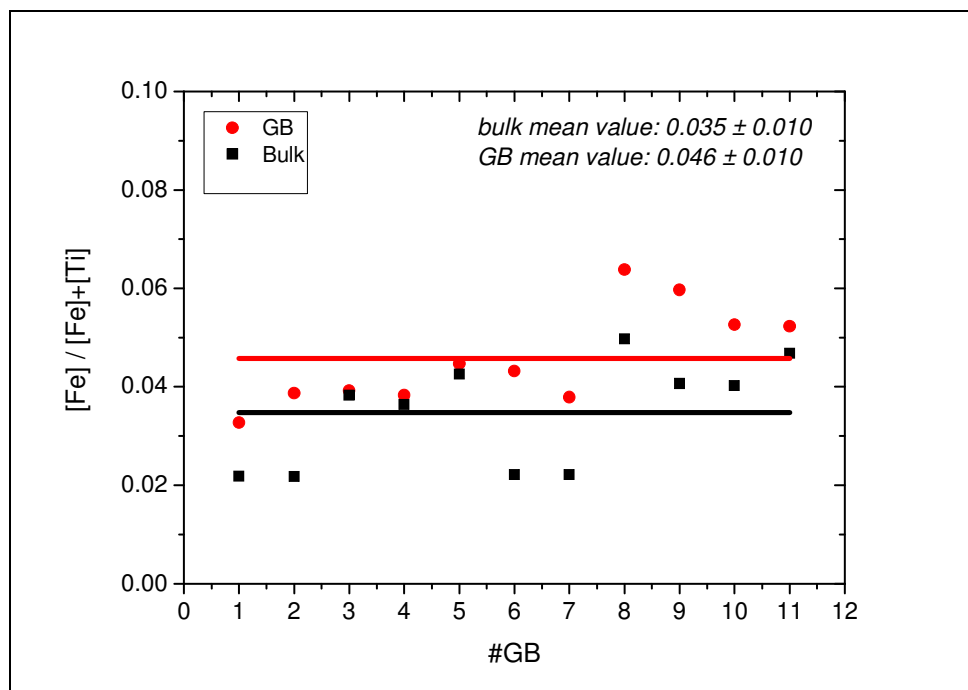


Figure 44 [Fe]/[Fe]+[Ti] ratio content in the bulk as well as in the grain boundaries determined by EDX spectra. The average ratio in the grain interior as well as in the GBs is presented by red and black lines respectively. The error is the standard deviation of the values. Note that in all the GBs considered the Fe concentration is higher compared to the adjacent grain.

Almost in all measurements the Fe signal emerged from the GBs was more significant than the corresponding one from the grain interior. This is shown quantitatively in Figure 44, where the GBs exhibit clearly higher $[\text{Fe}]/([\text{Fe}] + [\text{Ti}])$ ratio than the grains. This may indicate a certain segregation of Fe in the region close to the grain boundaries, which was already observed by Chiang *et al.* in Fe-doped SrTiO_3 .^[72] It is also worth noting that the Fe concentration determined by EDX spectra is lower than (i) the nominal value and (ii) the values obtained from the analysis of the EXAFS data.

In the following, the electrochemical characterization of Fe-doped SrTiO_3 , carried out via means of impedance spectroscopy is elucidated in details. The spectrum of the 0.6at% Fe-doped sample after the annealing process are reported in Figure 45 as example of IS on microcrystalline material, in which both bulk and GB semicircles are present.

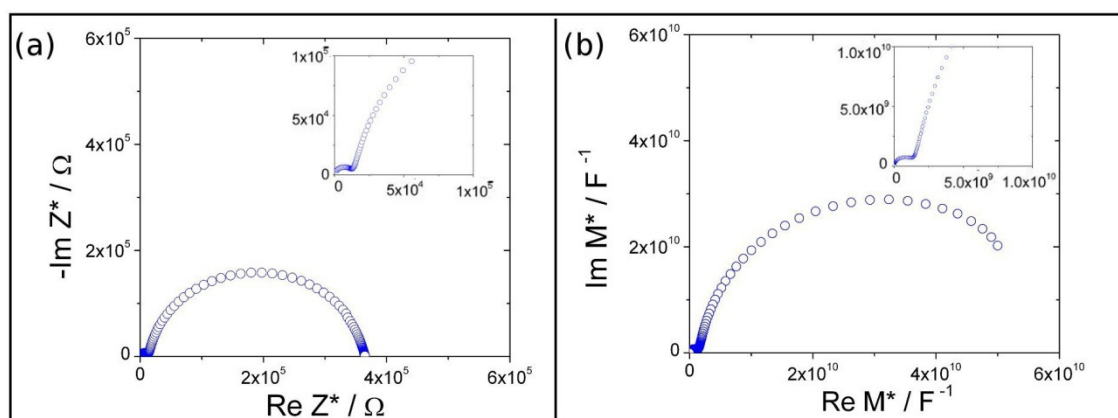


Figure 45 Impedance (Z^*) and modulus (M^*) spectra of the 0.6at% Fe-doped SrTiO_3 sample after annealing in air at 1400°C for 5 hours. The spectra have been acquired at 465°C and at $P = 1$ bar. Two semicircles are clearly distinguished in both the Z^* - and M^* -plots. The spectra were fitted using 2 RQ elements.

On the other hand, in the spectra acquired from the nanocrystalline samples (Figure 46), the bulk contribution disappears. When two semicircles are observed in the Z^* -plot of the nanometric samples, an equivalent circuit consisting of 2 RQ elements is used for the fitting. While the high frequency contribution is assigned to the GBs, the low frequency one can be ascribed to the electrode, in light of the following reasons: (i) the first contribution (high frequency) cannot arise from the bulk because σ is too low

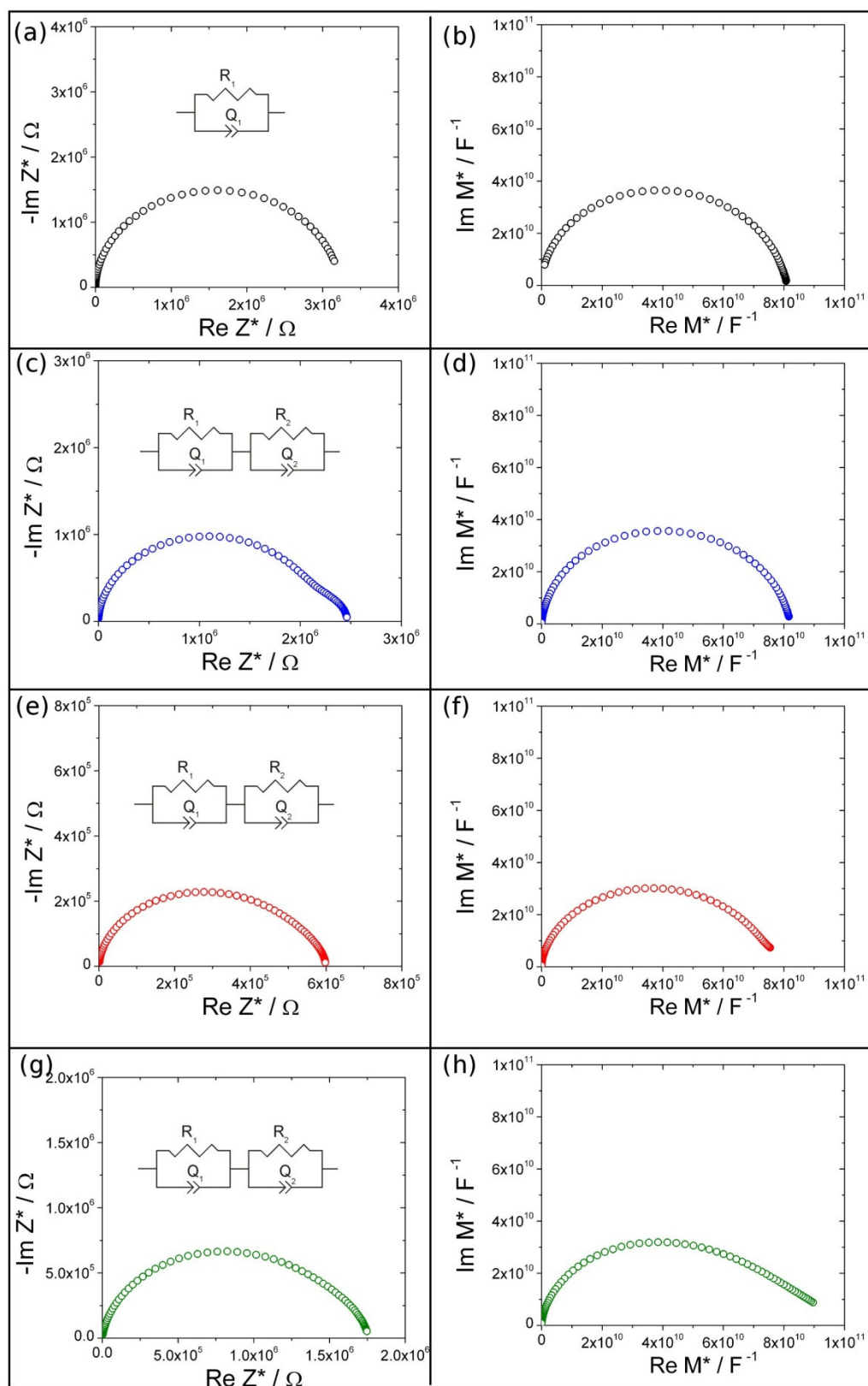


Figure 46 Impedance (Z^*) and modulus (M^*) spectra of nanocrystalline SrTiO_3 acquired at 465°C and $P = 1$ bar. (a) and (b) undoped SrTiO_3 ; (c) and (d) 0.6at% Fe homogeneously doped; (e) and (f) 3at% homogeneously doped; (g) and (h) 3at % Fe decorated. The equivalent circuit used for the fitting is represented for each sample.

and the corresponding ΔE is too high (it is typical of GBs, see Table XI)**; (ii) the capacitance value of the low frequency arc is large and in the modulus plot this contribution disappears.^[148,149] A similar response of the Pt electrode was observed also in SrTiO₃ single crystals (see the spectra reported in Figure 15) and previously by Jurado *et al.*^[171] As mentioned in chapter 4.2, the disappearance of the bulk contribution in both Z^* and M^* -plot in the p-type regime (characterized by blocking boundaries) is an evidence of a mesoscopic situation, in which the space charge layers overlap within the grain.

The results are elucidated considering separately the homogeneously doped samples and the decorated ones.

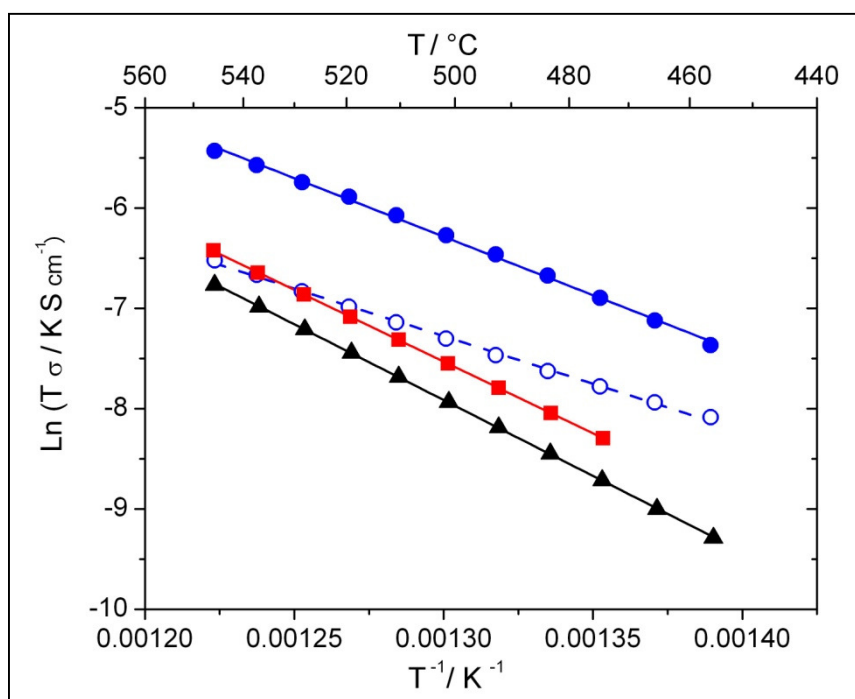


Figure 47 Arrhenius plot of the conductivity in the temperature range between 550 and 450°C. The symbols are assigned as follows: (**black open triangles**) nanocrystalline undoped SrTiO₃; (**red solid squares**) nanocrystalline 0.6at% homogeneously doped SrTiO₃; (**blue solid circles**) nanocrystalline 3at% homogeneously doped SrTiO₃; (**blue open circles**) nanocrystalline 3at% decorated SrTiO₃.

** Typical activation energies for the bulk of slightly acceptor doped in SrTiO₃ have been determined to be around 1 eV.^[38,73,162] However, ΔE_{bulk} significantly decreases when the Fe content is enhanced.^[171]

Table XI Values of the activation energies determined in pure O₂ and of the P dependence at 544°C of undoped and Fe-doped SrTiO₃.

dopant		ΔE in O ₂ [eV]	slope p	slope n
undoped		1.30	0.23	-0.25
0.6%Fe micro	Bulk	1.05	0.18	
	GB	1.53	0.25	
0.6%Fe nano		1.23	0.25	-0.24
3%Fe nano homogenous		1.05	0.25	-0.25
3%Fe nano decorated		0.81	0.16	-0.20

Homogeneously doped compositions

If one first considers the nanocrystalline undoped material as reference, it turns out that despite the different powder preparation, it behaves very similarly to the materials whose properties are reported in section 4.2 and in previous studies.^[73] As a matter of fact, the acceptor impurity content (mainly Al and B) determined via ICP–OES is approximately 0.01 at% (Table V) and λ^* is, therefore, larger than half of the grain size. The P dependence and the activation energies, reported in Table XI, are in perfect agreement with the values reported in ref. [163]. The value of the space charge potential in pure oxygen can be determined according to Eq. 4.2,^{††} yielding $\Delta\phi_0 = 0.45$ eV, which is considerably lower than for the microcrystalline samples (~ 0.70 eV) calculated in chapter 4.2 and also reported in ref.s [64,73]. According to the definition of surface charge density in the Mott-Schottky approximation (Eq. 2.48), $\Sigma = 2.6 \cdot 10^{-6}$ C/cm² was obtained, which corresponds to a $V_o^{\bullet\bullet}$ surface concentration of $8.1 \cdot 10^{12}$ cm⁻² (assuming a core thickness equal to a single atomic layer).

^{††} The bulk conductivity used in this case is the theoretical bulk conductivity determined according to ref. [39] considering an impurity content of 0.01at%.

For the undoped composition one can at first ignore the m term of Eq. 4.11 and determine $\partial\Delta\phi_0/\partial\text{Log}(pO_2)=0.003\text{ V/bar}$. This result disagrees with the trend reported in section 4.3 for the undoped material, in which it was observed that $\Delta\phi_0$ (and hence the charge density Σ) increases while decreasing P due to the increase of V_o^{**} concentration in the GB core. This means that the absence of redox active species cannot be neglected even in a nominally pure system. Moreover, it must be considered that the role of boron (which is the main impurity according to ICP-OES) in mixed conducting oxides can be more complex and can affect the GB properties.^[169]

Let us now consider the Fe-doped samples. It is worth remembering here that Fe exhibits a mixture of oxidation states of +III and +IV and that the concentration of Fe^{3+} increases while decreasing P .^[39,93-97] Furthermore, due to the presence of a positive space charge potential, one expects an enrichment of Fe_{Ti}' within the space charge region according to Eq. 2.35. Nonetheless, the concentration of Fe_{Ti}' cannot exceed the total concentration of Fe, which is fixed by the amount of dopant added during the sample preparation.

In the case of the 0.6 at% homogenous sample the disappearance of the bulk contribution can be easily explained by the overlapping of the space charge layers. Notably, if one considers that even when all Fe is in the +III valence state, λ^* is approximately 15 nm and the condition $2\lambda^* \geq d_g$ ($L \sim 30$ nm according to the TEM analysis) is satisfied causing the mesoscopic case to occur.

For the 3at% Fe-SrTiO₃, one should note that despite the large Fe content, at high P values ($1-10^{-5}$ bar), the condition $2\lambda^* > d_g$ is still fulfilled according to Eq. 2.17. The situation changes significantly in reducing atmosphere, in which $[Fe_{Ti}'] \approx [Fe_{tot}']$ ^[96] and $\lambda^* = 6$ nm. At low P , since when the material is n-type conductor, now the highly n-type conductive GBs short-circuit the grain interior similarly to what was already observed in n-type nanocrystalline CeO₂.^[18,169] In addition to these considerations, it is worth noting that the Fe segregation detected via the TEM-EDX analysis reduces the amount of Fe_{Ti}' in the bulk and, consequently increases λ^* .

If one now considers the conductivity data depicted in Figure 48, as expected from Eq.s 2.14 and 2.17, an increased Fe content results in an enhanced p-type and a decreased n-type conductivity. Interestingly, as summarized in Table XI, for both the 0.6at% and 3at% Fe-SrTiO₃, the P dependence of the measured conductivity is equal to 0.25 in the high P range (p-type conductivity). In light of Eq.s 4.10 and 4.14, these results imply two different scenarios: either (i) m as well as Σ and, consequently, $\Delta\phi_0$ are P invariant or (ii) since the m -term and the $\Delta\phi_0$ -term in Eq. 4.10 have opposite sign, both m and $\Delta\phi_0$ increases (or decrease) upon a change of P .

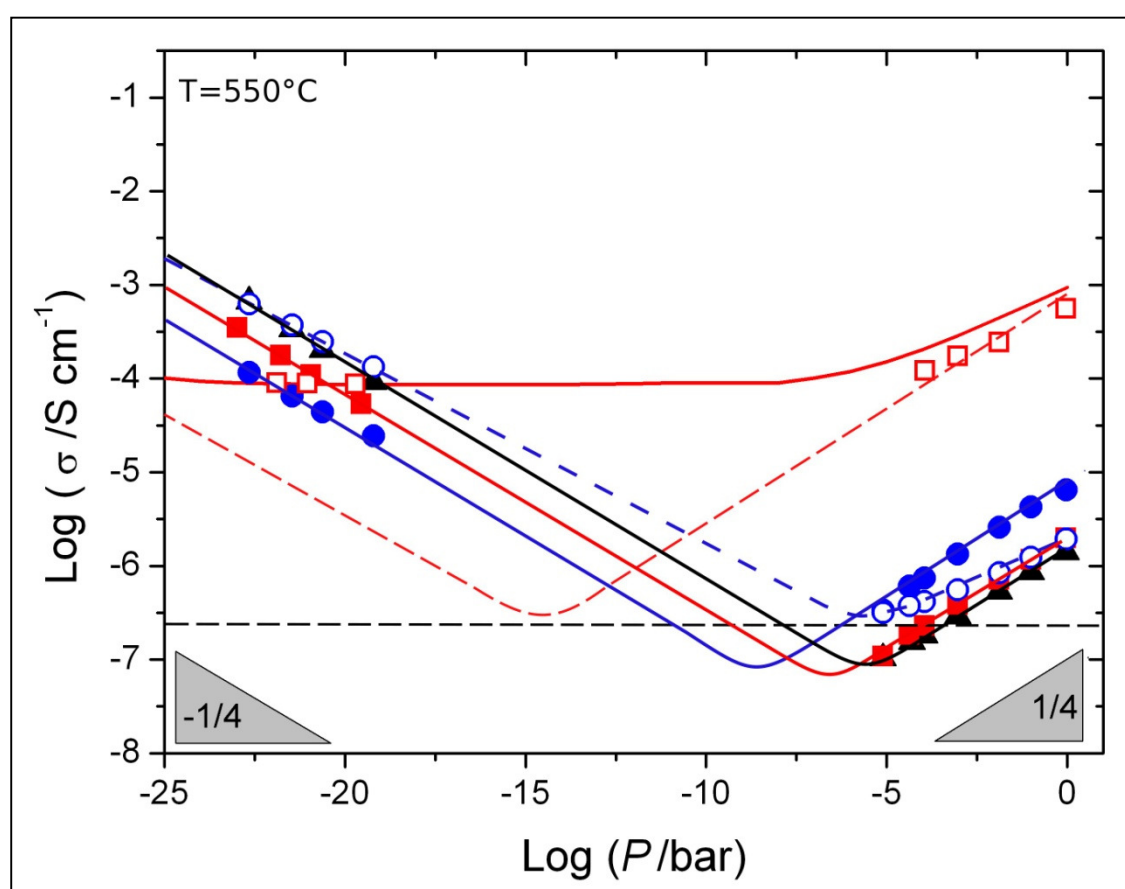


Figure 48 P -dependence of the conductivity of the nanocrystalline Fe-doped SrTiO₃ ($T = 544^\circ\text{C}$). The symbols are assigned as follows: (**black open triangles**) nanocrystalline undoped SrTiO₃; (**red open squares**) bulk of the annealed 0.6at% homogeneously doped SrTiO₃; (**red solid squares**) nanocrystalline 0.6at% homogeneously doped SrTiO₃; (**blue solid circles**) nanocrystalline 3at% homogeneously doped SrTiO₃; (**blue open circles**) nanocrystalline 3at% decorated SrTiO₃. The **red solid line** and **red dashed line** refer respectively to the total and to the electronic bulk conductivity of the annealed 0.6at% Fe-doped. The **black dashed line** refers to the theoretical conductivity at the minimum (Eq. 2.60).

In the first case, m being constant with decreasing P means that the Fe cations must be all ionized already in pure oxygen. This implies (as shown above) $\lambda^* = 6$ nm

for 3at% Fe-SrTiO₃, indicating that we should detect not only the GB contribution in the impedance spectra but also the bulk semicircle. As this is clearly not the case, this hypothesis can be discarded.

As a matter of fact, in light of Eq. 2.17, one expects m to increase with decreasing P . In order to verify this (and the other considerations made above), we heat-treated the 0.6at% Fe-doped sample in air at 1400°C for 4 hours with the purpose of letting the grains coarsen.

Upon annealing, one recognizes two distinct contributions in both the Z^* and M^* plots, corresponding to the bulk and the grain boundaries (see Figure 45). The bulk conductivity is however significantly lower than expected for that Fe content. This discrepancy cannot be fully explained by recent studies indicating that the $V_O^{\bullet\bullet}$ mobility values published by Denk *et al.* are overestimated by a factor 2 or 3. [66,68] The remaining significant difference points towards a possible segregation of dopant during annealing.

Nevertheless, under oxidizing conditions, the P dependence of the bulk conductivity is 0.18. According to Eq. 4.3, the discrepancy from 0.25 has to be ascribed to the Fe ionization reaction and one can estimate $(\partial \text{Log } m / \partial \text{Log } P)_{\text{bulk}} = -0.14$.

On the other side, the P dependence of the GB conductivity is equal to 0.25, in excellent agreement with the data obtained from both nanocrystalline samples. As for the coarsened sample the conductivity measurements give information about both bulk and GB contributions for different values of P , $\Delta\phi_0$ can be calculated according to Eq. 2.54. The values obtained (e.g. $\Delta\phi_0 = 0.65$ V at $P = 1$ bar) are typical for polycrystalline SrTiO₃. [64,73,161]

One now can determine $(\partial \Delta\phi_0 / \partial \text{Log } P) = -0.021$ (see Figure 49); the negative sign implies that the potential increases when P decreases. From this and by considering Eq. 4.10, the value of $(\partial \text{Log } m / \partial \text{Log } P)_{\text{GB}} = -0.18$ is obtained, which is perceptibly more negative than the value obtained for the bulk. In other words: the P dependence of m is steeper at the grain boundaries than in the bulk. This finding supports the hypothesis of Fe segregation during coarsening.

In the case of the nanocrystalline sample the space charge potential at $P = 1$ bar was determined from the activation energy of the conductivity according to Eq. 2.58

(blocking boundaries), using the same temperature dependence of $\Delta\phi_0$ as for the microcrystalline sample, yielding $\Delta\phi_0 = 0.35\text{ V}$. One can also estimate $\Delta\phi_0$ assuming that the charge carrier concentration profiles are flat – Eq. 4.2 – and in this case one obtains $\Delta\phi_0 = 0.40\text{ V}$. The fact that the latter value does not deviate significantly from 0.35 V demonstrates that the flat concentration is a reasonable approximation even for higher dopant contents. The difference between this value and the value of $\Delta\phi_0$ for the undoped sample is very close to the difference of the activation energies of the two materials. The values of $\Delta\phi_0$ determined at different oxygen partial pressures are plotted in Figure 49 also for the nanocrystalline sample. Here, the key result is however represented by the reduction of $\Delta\phi_0$ upon downsizing SrTiO_3 , which is consistent with the studies on undoped SrTiO_3 reported in section 4.2.

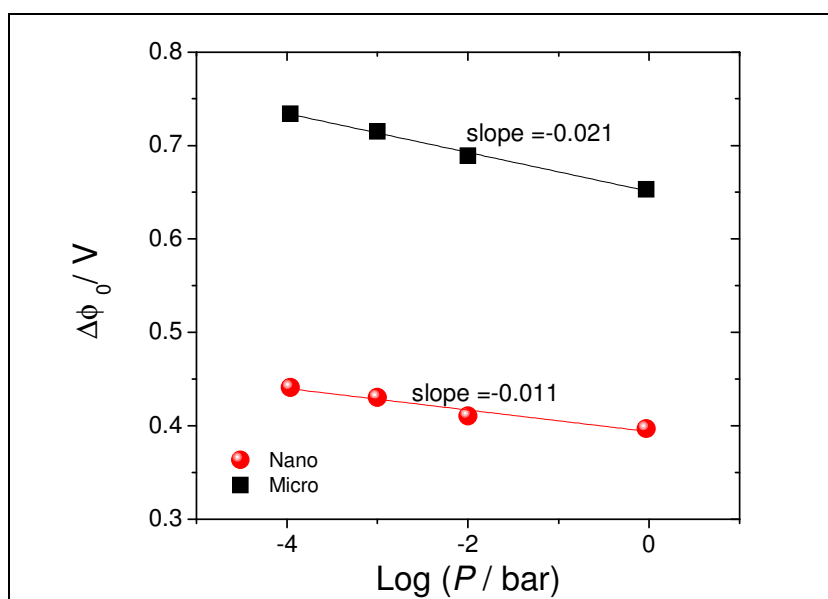


Figure 49 P -dependence of the space charge potential in nanocrystalline and microcrystalline 0.6at% Fe- SrTiO_3 . The **black squares** refer to the microcrystalline material, whereas the **red spheres** to the nanocrystalline one.

As pointed out in section 4.3, a more precise analysis uses the interfacial charge density Σ at the GBs, which can be determined according to Eq. 2.48 (Mott-Schottky approximation). In the diagram shown in Figure 50, one can observe that Σ is reduced in the nanocrystalline material. At $P = 1\text{ bar}$ it is equal to $5.62 \cdot 10^{-6}\text{ C} \cdot \text{cm}^{-2}$ in the nanocrystalline sample and $7.21 \cdot 10^{-6}\text{ C} \cdot \text{cm}^{-2}$ for the microcrystalline one. Assuming that the GBs are charged due to the excess of oxygen vacancies the difference of Σ

between nano- and micro-crystalline samples indicates a lower surface concentration of approximately 20% ($5 \cdot 10^{12} \text{ cm}^{-2}$) in the former.

Remarkably, as in the case of undoped SrTiO_3 Σ increases while reducing P , with the nanocrystalline material characterized by a lower value of Σ (Figure 50). At this point, it is again interesting to plot $\partial \text{Log } \Sigma$ vs. $\partial \text{Log } P$ according to Eq. 4.18 (Figure 51). As already observed for the undoped material, $\partial \text{Log } \Sigma / \partial \text{Log } P$ results to be the same for both the microcrystalline and the nanocrystalline samples (-0.08). Notably, this value is slightly more negative than the one obtained for the undoped material.

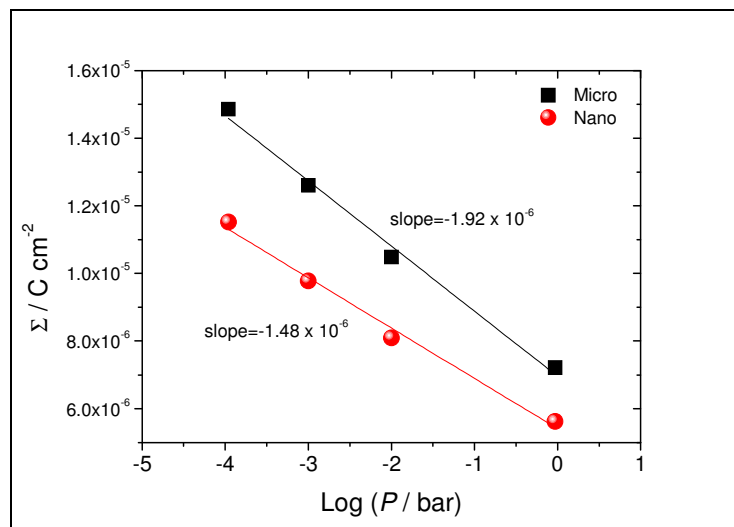


Figure 50 P -dependence of the surface charge density. (**black squares**) microcrystalline material; (**red spheres**) nanocrystalline sample.

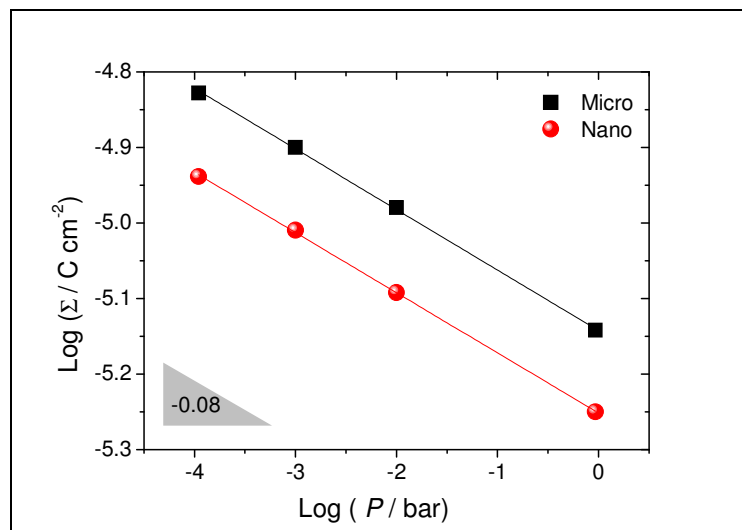


Figure 51 logarithmic plot of Σ versus the oxygen partial pressure dependence. The symbols are assigned as follows: (**black squares**) microcrystalline material; (**red spheres**) nanocrystalline sample.

Comparing the conductivity values of the homogeneously doped nanocrystalline samples (Figure 48), it is obvious that increasing the Fe content, the p-type conductivity increases whereas the n-type conductivity decreases, with a consequent shift of the conductivity minimum towards lower values of oxygen partial pressure. In particular switching from 0.6at% to 3at% the increase is approximately by a factor 3. This is in agreement with the defect chemistry, as acceptor defects (Fe_{Ti}') are mainly compensated by $V_O^{\bullet\bullet}$,^[96] which are related to the electron holes h^\bullet by Eq. 2.14. Therefore, an increase of the Fe content would lead to an increase of the hole concentration and consequently of the p-type conductivity also in the mesoscopic regime.

In addition, since the variation of m with the P does not vary significantly between 0.6at% and 3at% the constancy of the P -dependence of the conductivity indicates that also the variation of Σ is independent of the Fe concentration.

If one now considers the activation energies of the nanocrystalline homogeneously doped samples (Figure 47 and Table XIII), it turns out that while increasing the Fe content, the activation energy decreases. The trend can be explained by a reduction of the space charge potential with the addition of dopant according to Eq. 2.58. A similar behaviour was observed also in acceptor (yttrium) doped CeO_2 .^[172]

Nanocrystalline GB decorated material

As mentioned above, the EXAFS and XANES analyses indicated that in the nanocrystalline $SrTiO_3$ decorated with 3at% Fe only a fraction of the acceptors diffuses inside the grain interior (bulk), while approximately the half of the Fe atoms remain at the boundaries exhibiting a local environment with a coordination similar to the one in Fe_2O_3 .

As shown in Figure 46g, the impedance spectra are characterized by two semicircles that are assigned (according to the capacitance values) to the grain boundaries (mid frequencies range) and to the electrode contribution (low frequencies range). The conductivity measurements allow us to exclude that one of the contributions of the IS spectra is due to a possible Fe_2O_3 at the GBs. Notably, Fe_2O_3 is known to be a n-type semiconductor at temperatures below $800^\circ C$,^[173,174] and neither

the high frequency contribution in the IS spectra nor the low frequency semicircle exhibited such conduction properties.

In order to treat quantitatively the conductivity data, let us first assume that all Fe atoms remain in the GB core replacing Ti;^{‡‡} this corresponds to a negative charge, whose surface density is $\Sigma_{Fe} = -1.73 \cdot 10^{-6} \text{ C/cm}^2$ at $P = 1 \text{ bar}$ and $\Sigma_{Fe} = -1.18 \cdot 10^{-5} \text{ C/cm}^2$ at $P = 10^{-5} \text{ bar}$. We can compare these values with the value of Σ obtained for undoped SrTiO₃ ($m = 0.01 \text{ at\%}$).^{§§} The negative charge arising from Fe_{Ti}^{\prime} would partially compensate the one of the core due to $V_O^{\bullet\bullet}$ resulting, at $P = 1 \text{ bar}$, in a net surface charge density of $\Sigma = +8.7 \cdot 10^{-7} \text{ C/cm}^2$, whereas, at $P = 10^{-5} \text{ bar}$, the negative charge would exceed the positive charge of the oxygen vacancies and thus $\Sigma = -9.2 \cdot 10^{-6} \text{ C/cm}^2$.

The resulting space charge potential (calculated from Σ and for $m = 0.01 \text{ at\%}$) would be $\Delta\phi_0 = 0.004 \text{ V}$ at $P = 1 \text{ bar}$ and $\Delta\phi_0 = -0.01 \text{ V}$ at $P = 10^{-5} \text{ bar}$. It is worth noting that the absolute value of the negative space charge potential would be expected to increase with decreasing P . At low oxygen partial pressure, when Fe is completely ionized^[96] one expects $\Sigma = -4.0 \cdot 10^{-5} \text{ C/cm}^2$, generating a space charge potential of -0.30 V . It is important to note that for such a value of $\Delta\phi_0$ a significant reduction of n-type conductivity would occur, which is however not observed in the experimental data.

Therefore one can rule out the space charge potential to be negative.

A further argument which excludes the possibility of $\Delta\phi_0 < 0$, is the position of the conductivity minimum, which can be determined according to Eq. 4.1 (under the assumption that all Fe ions remain outside the grains).

Therefore, for an impurity content of 0.01 at\% , $\Delta\phi_0 = -0.30 \text{ V}$ would lead to $P_{\min} \sim 10^{-18} \text{ bar}$, which is in contradiction with the experimental data (see Figure 48).

^{‡‡} We can exclude Fe to be in the GB core as interstitial. This would drastically raise the space charge potential and consequently provoke a strong depression of the p-type conductivity.

^{§§} For a nominally pure SrTiO₃ ($m = 0.01 \text{ at\%}$) we can determine Σ by considering a Mott-Schottky case and $\Delta\phi_0 = 0.45 \text{ eV}$ as determined previously. This yields $\Sigma = 2.6 \cdot 10^{-6} \text{ C/cm}^2$, from which we can estimate the concentration of the excess positive charge ($V_O^{\bullet\bullet}$) to be equal to $8.17 \cdot 10^{12} \text{ cm}^{-2}$.

In the light of these considerations based on the results of the impedance spectroscopy measurements, we can validate the EXAFS results which observed that about half of the overall iron atoms added through the decoration procedure remain outside the grains. Rather, a fraction of them (~50%) diffuses into the grain (as indicated independently by EXAFS and XANES) creating a core-shell situation, as illustrated in Figure 52. Similar results have been also observed for decorated nanocrystalline CeO₂ (see the details in the appendix): the core remains essentially undoped ($m = 0.01\text{at}\%$), while a thin shell results to be heavily acceptor doped. It is worth noting here that the diffusion of 50% of the iron would correspond to a dopant content of 15at% in a shell of 1 nm.

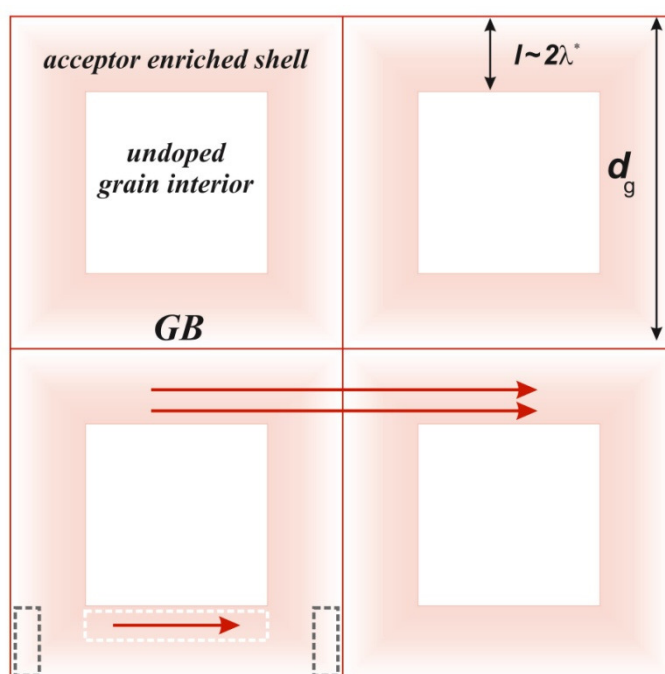


Figure 52 2D schematic rendering of the conduction pathways (red arrows) for the decorated sample, according to the brick layer model. Here only 2 of the 4 GBs contributing to the hole transport can be clearly recognized (the 2 parallel to the plane of the sheet are not visible). The grey dashed boxes represent the most blocking parts of the shell while the white dashed lines frame the most conducting parts of the shell.

As only a single contribution is observed in the impedance spectra (and the potential is positive), the shell is in the mesoscopic situation and yet short-circuit the less conductive undoped bulk.

It is interesting to note that, in pure O₂, the conductivity of the 0.6 at% homogeneously doped nanocrystalline sample is identical to the conductivity of the

decorated specimen. If we assume a flat concentration profile within the shell, we can write (Brick layer model)

$$\frac{4l}{d_g} \left(e u_p p_{bulk}^{dec} \right) e^{-\frac{e\Delta\phi_0^{dec}}{kT}} = \sigma_m^{hom} \quad 4.19$$

where l is the thickness of the shell, d_g the average grain size, u_p is the hole mobility, p_{bulk}^{dec} is the bulk concentration of the holes in the shell, $\Delta\phi_0^{dec}$ is the space charge potential of the decorated sample and σ_m^{hom} the measured conductivity of the 0.6 at% homogeneously doped sample. From Eq. 4.19, and by taking $l = 1$ nm, $d_g = 30$ nm and $\Delta\phi_0^{dec}$ equal to the potential in the undoped nanocrystalline sample (0.45 eV – this represents the upper limit of $\Delta\phi_0^{dec}$, as, due to the presence of iron ions in the GB core, we expect $\Delta\phi_0^{dec}$ to be actually reduced) we obtain $p_{bulk}^{dec} = 6.3 \cdot 10^{17} \text{ cm}^{-3}$, which corresponds to $m = [Fe_{tot}] = 3.36 \cdot 10^{20} \text{ cm}^{-3}$ (~2 at%) and $[Fe_{tot}] = 1.34 \cdot 10^{21} \text{ cm}^{-3}$ (~8 at%), respectively. This value represent the lower limit of m (as here we took the upper limit of $\Delta\phi_0^{dec}$) within the shell.

The lower limit of $\Delta\phi_0^{dec}$ can be estimated by assuming that all Fe diffused in the shell. In this case, $[Fe_{tot}] = 2.52 \cdot 10^{21} \text{ cm}^{-3}$ (~15 at%) and $m = [Fe_{tot}] = 2.52 \cdot 10^{21} \text{ cm}^{-3}$ (~4 at%) at $P = 1$ bar and, according to Eq. 4.19, $\Delta\phi_0^{dec} = 0.42$ V.

Let us now consider the value of the activation energy of the GB conductivity (determined at $P = 1$ bar), which is equal to 0.81 eV and hence considerably lower than the other samples and also than the GB values available in previous studies on slightly acceptor doped SrTiO_3 .^[60,66,73,161] Interestingly, Jurado *et al.* observed that the bulk activation energy decreases drastically with increasing the Fe content down to even 0.46 eV for 15at% Fe.^[162,171] Therefore, since the bulk activation energy can reach such low values when highly doped, we can expect the activation energy of 0.81 eV to correspond to the contribution of a highly doped shell in the mesoscopic situation (with positive potential). Further evidence comes from the determination of the space charge potential.

Notably, as already in the case of the GB conductivity (Eq. 2.57) the activation energy of the measured conductivity in the mesoscopic regime σ_m is given by:

$$\Delta E_m = -\frac{\partial \ln \sigma_m}{\partial (1/kT)}. \quad 4.20$$

Combining Eq.s 4.2 and 4.20 (flat profile approximation) the following expression results:

$$\Delta E_m = \Delta E_{bulk} + e\Delta\phi_0 + \frac{e}{kT} \frac{\partial e\Delta\phi_0}{\partial (1/kT)}. \quad 4.21$$

Now, we can determine the last term of Eq. 4.21 for the microcrystalline material, and considering ΔE_{bulk} from ref. [171] $\Delta\phi_0^{dec} = 0.46\text{V}$ is obtained, which is very close to the lower limit of $\Delta\phi_0^{dec}$ determined above according to Eq. 4.19.

Moreover, it is worth emphasizing that the conduction properties of the decorated SrTiO₃ are then fully determined by the conduction in the highly doped shell, but the space charge potential remains almost invariant, despite the presence of Fe in the GB core.

Another important aspect that it is worth considering is the P dependence of the conductivity of the decorated sample. In marked contrast to the other samples (homogeneously doped compositions) investigated in this study, $\partial\sigma^{dec}/\partial\text{Log } P$ is much lower and equal to 0.16 in the p-type regime and -0.20 in the n-type regime. According the model developed by Denk *et al.*^[39] (Eq.s 2.14 and 2.17), for heavily Fe doped compositions the term $\partial\text{Log } m/\partial\text{Log } pO_2$ does not change significantly with the composition: e.g. from 3at% to 30at% (which would be the content if all Fe diffuses in a shell 1 nm thick) the slope changes from -0.14 to -0.16 . This means that irrespective of the actual Fe content in the shell, we can estimate $(\partial \Delta\phi_0^{dec}/\partial\text{Log } pO_2)$ to be equal to -0.002 . This is in line but somewhat lower than what was previously reported in section 4.2 and in ref. [163].

Interestingly, the analysis of the data collected in the n-type regime (in which the electrical transport is controlled by the highly conducting parallel boundaries) reveals that the experimental P dependence of σ_m^{dec} is -0.20 . Knowing that, at low P the Fe ionization can be neglected, from Eq. 4.11 and 4.17 one obtains a positive P dependence of $\Delta\phi_0^{dec}$. This result that at first might seem surprising (and in

contradiction with what observed in the p-type regime) can be explained if one consider that under strongly reducing conditions (i) all Fe is ionized and (ii) the high electron concentration can induce the association $V_o^{\bullet\bullet} + e' \rightleftharpoons V_o^\bullet$ (or even $V_o^{\bullet\bullet} + 2e' \rightleftharpoons V_o^x$). Thus starting from very low oxygen partial pressure values (e.g. 10^{-24} bar), with increasing P and the electron-vacancies defects dissociate (this corresponds to a positive $\partial\Delta\phi_0^{dec} / \partial\text{Log}(pO_2)$). The P dependence of $\Delta\phi_0^{dec}$ becomes negative when $V_o^{\bullet\bullet}$ (all dissociated from the electrons) starts to get filled by the oxygen (from the environment) and iron gets oxidized (note that the for 2at% Fe, the oxidation at 544°C is relevant for $P > 10^{-15}$ bar)

Further interesting pieces of information can be extracted from the value of the conductivity at the minimum, at which the conductivity (σ_{min}^{dec}) corresponds to $2F\sqrt{K_B u_n u_p}$ (being F the Faraday constant). From Figure 48 it emerges that the value of σ_{min}^{dec} is half an order of magnitude higher than the conductivity of the undoped material at the minimum (σ_{min}^{Und}). Therefore, under the assumption that the charge carrier mobilities do not change in the two materials, the difference can only be ascribed to K_B which is related to the band gap of the material. Notably, such a difference of σ_{min} can be related to a reduction of the band gap of 0.24 eV (e.g. from 3.3 eV^[39] to approximately 3 eV) in the decorated sample. A decrease of the band gap energy, while significantly increasing the Fe content has been already observed by Rothschild *et al.*^[50]. In our case this is in agreement with the assumption of a high Fe concentration in the shell adjacent to the GBs.

Section conclusions:

In this section, the electrical conduction properties of iron doped SrTiO₃ have been discussed. As in the undoped material huge size effects appear when the material is downsized to the nanoscale, namely significant drops in the p-type conductivity and increases in the n-type conductivity.

Considerations on the core charge density revealed an increase of the oxygen vacancy concentration in the GB core while reducing the P . All the experimental results could be nicely explained in light of the general space charge model. It was observed that increasing Fe content the space charge potential decreases.

Furthermore, it has been shown that the spatial distribution of the dopant (homogeneously doped vs. decorated samples) can crucially affect the space charge properties and therefore the electrical transport. Notably, in the GB decorated sample, a core-shell situation is established within the grains. The outer shell, which is in the mesoscopic regime, acts a preferential pathway for the hole transport and short-circuits the low conductive bulk. However, the presence of iron also in the GB core leads to an increase of the space charge potential compared to the homogeneously doped material.^[175,176]

4.5 Electrical conduction properties of nanocrystalline donor doped SrTiO₃

The last part of this study regards the investigation of nanocrystalline donor doped SrTiO₃. As shown in section 2.1.2 donor doping turns the material into a n-type conductor, in which the electrons are the dominating charge carriers. This feature makes this material particularly suitable for anodes in SOFCs, thanks to the high electronic conductivity, even though the electrocatalytic activity for fuel oxidation has still to be improved (see e.g. ref.s [102,177-181] in which the effect of different dopants, namely lanthanum, yttrium, niobium and tantalum, has been investigated).

In particular, if one considers the oxygen non-stoichiometry via the P dependence of the conductivity at high temperatures, three regimes can be recognized (Figure 9): (i) at high oxygen partial pressure, donors are compensated by intrinsic acceptors in form of strontium vacancies (V_{Sr}''), yielding to a n-type conductivity characterized by a P dependence of $-1/4$ (Eq. 2.28); (ii) in the middle range of P , $n = [D^\bullet]$ holds and the conductivity is independent of P (Eq. 2.26); (iii) at very low P the oxygen vacancy $V_O^{\bullet\bullet}$ concentration becomes so high that it is compensated by the electrons, giving rise to the intrinsic electronic conductivity with P dependence of $-1/6$ (Eq. 2.25). However, the sintering atmosphere may influence the defect compensation and, thus, the defect chemistry.^[87,182]

It is worth noting here that previous publications on donor doped SrTiO₃ pointed out that also in this case the GB core is positively charged. Evidence for this was given for example by Chiang *et al.*, who did not observe any donor segregation at the GBs, in contrast to the case of acceptor doping.^[72] De Souza, pointed out that the system is still characterized by high GBs resistivities (although in presence of a positive space charge potential one would expect high n-type conductivity in the space charge region), and he ascribes this to the “selective oxidation of the bulk phase in the vicinity of the GBs”.^[68] On the other hand, a negative space charge potential is the reason of the creation of the positive temperature coefficient (PTC) effect in donor doped BaTiO₃.^[183-189] The reason of this consists of the formation of acceptor states in the GB core. However, their origin is still not well understood and Preis *et al.*^[185] suggested either segregation of the acceptor co-dopants into the core or the formation of cation

vacancies (V_{Sr}'' or V_{Ti}'''') during sintering owing to the oxidation processes at the GB regions (i.e. $O_{2(g)} + 2e' \rightleftharpoons 2O_O^x + V_{Sr}''$). Diffusion studies on donor doped titanates similar to SrTiO₃ (BaTiO₃ and Pb(Zr_xTi_{1-x})O₃) pointed out the increase of the oxygen diffusion at the grain boundaries which could be ascribed to an enrichment of V_O^{**} in the space charge region.^[190,191]

Surprisingly, the conduction properties of donor doped SrTiO₃ have been studied only at high temperature^[41,100,101] and experiments as well as a defect chemistry model for low temperatures (< 800°C) are clearly missing. In light of these considerations and in view of the studies on undoped and acceptor doped SrTiO₃, the investigation of nanocrystalline Nb-SrTiO₃ becomes very attractive, since it offers the possibility to analyse two unexplored issues at the same time: the conduction properties of donor doped SrTiO₃ (i) at the nanoscale and (ii) at low temperatures.

Bearing in mind that only few studies on the grain boundary properties of donor doped SrTiO₃ have been carried out, but, on the other hand, there are a lot of data available in literature on donor doped BaTiO₃ (especially in the contest of positive temperature coefficient PTC resistors^[183-189]) it is worth referring also to the latter to support our analysis.

The Nb-doped SrTiO₃ nanopowders were prepared and characterized as described in section 4.1. They were then spark plasma sintered in inert atmosphere (Argon), at 750°C for 5 minutes, applying a pressure of 350 MPa. The final density is approximately 80% of the theoretical one. However, since we cannot avoid the presence of oxygen in the sintering chamber, it has to be borne in mind that the sintering atmosphere is strongly reducing.

Also in this context, transmission electron microscopy was employed to analyse the microstructure of the sintered pellets and, combined with EDX, the distribution of the niobium throughout the grains. The TEM micrographs of the sintered pellet showed a final grain size smaller than 30 nm (Figure 53), indicating a slight grain growth during the densification process if one compares the particle size reported in Figure 26d. The EDX analysis has been performed at the GB and in the adjacent grain on fourteen different positions. The spectra acquired at the GBs and in the grain interior confirmed the presence of Nb in the material and let us exclude a possible segregation

of the dopant at the GBs, as also observed by Chiang *et al.*^[72] Notably, the intensity of the Nb L-edge is the same in both cases (Figure 54), confirming the same Nb concentration throughout the all grain.

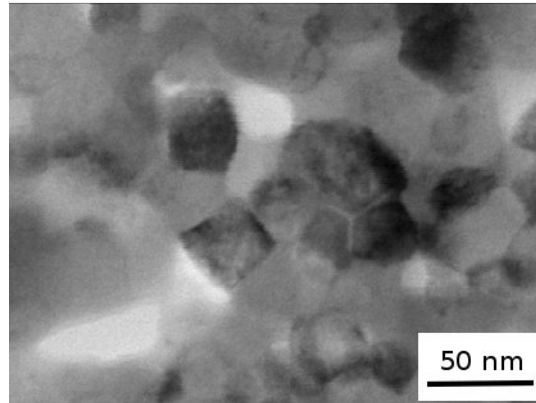


Figure 53 TEM micrograph of the sintered 3at% Nb-SrTiO₃ sample

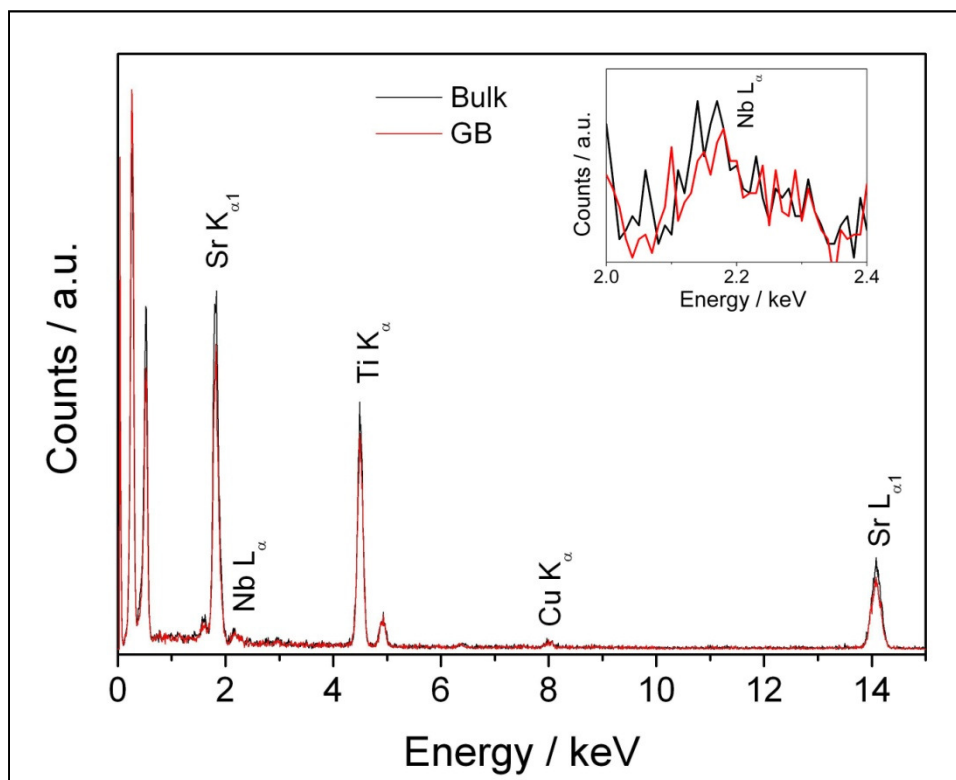


Figure 54 EDX spectra taken at the GBs and in the grain interior. If one considers the Nb L-edge, the intensity of the peak does not change, yielding to the conclusion that the Nb content does not vary. The Cu K_α is due to the sample holder.

In addition, X-ray photoelectron spectroscopy (XPS) was also employed to check the presence of Nb in the materials. As can be observed in Figure 55, the peak of the 3d orbital of niobium appears at 200 eV, confirming in this way the presence of Nb in the sample. No impurities were detected.

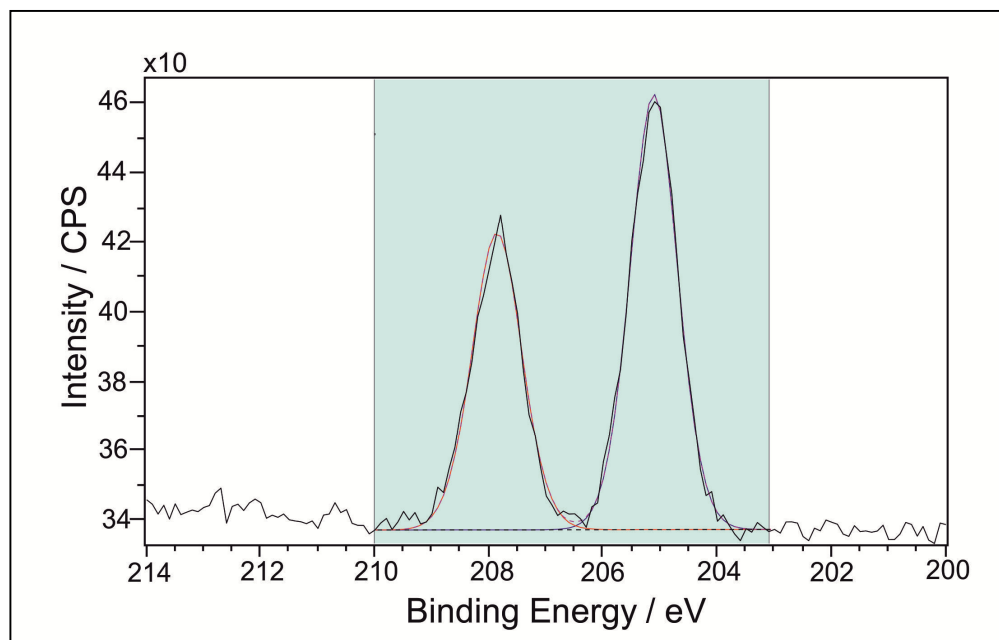


Figure 55 XPS spectrum on the Nb edge. The sharp peak indicates the presence of Nb in the material.

The conduction properties of the sintered pellets have been characterized via means of electrochemical impedance spectroscopy. The impedance (Z^*) and dielectric modulus (M^*) spectra ($T=550^\circ\text{C}$ at $P = 1$ bar) of the as-SPSed nanocrystalline Nb-doped SrTiO_3 analyzed in this study are reported in Figure 56. The spectra are characterized by only one semicircle in both the Z^* - and the M^* -plot. From the T -dependence of the conductivity at $P = 1$ bar the values of the activation energies were determined in the temperature range $550\text{-}450^\circ\text{C}$ and they are equal to 1.33 eV for the 0.6at% Nb and 1.38 for the 3at% Nb (for the latter see the solid red circle in Figure 57). It is worth noting here that the activation energy of the undoped material prepared in the same conditions is 1.30 eV (Table XI). These values let us assign this contribution to the GBs, in analogy with the results obtained on nanocrystalline SrTiO_3 which are reported in this study.

The P -dependence of the conductivity is reported in Figure 58. It can be observed that for Nb-doped SrTiO_3 , in the high P regime, the conductivity decreases while decreasing P ($\sigma \propto P^{1/4}$). According to the defect chemistry of SrTiO_3 and similar

perovskites (e.g. BaTiO₃) this is evidence that the dominant charge carriers are electron holes and the conductivity is, therefore, p-type.^[36,39,41,85,98] This is, however, a new and unexpected feature in donor doped SrTiO₃.

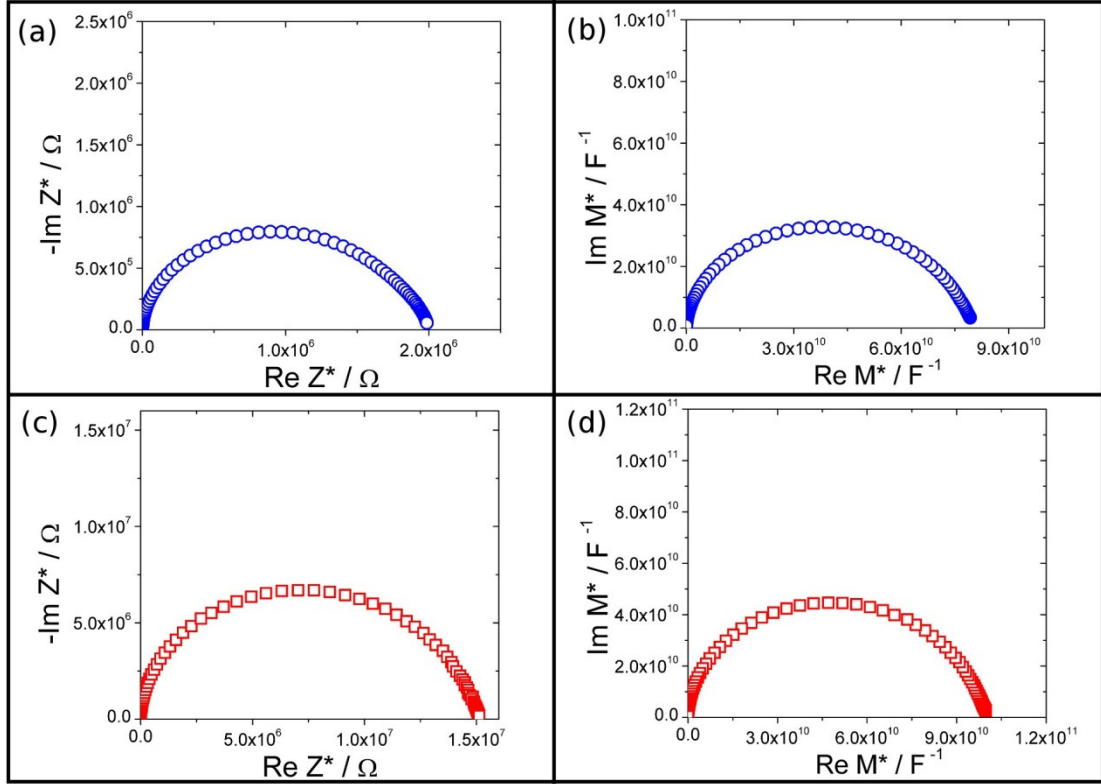


Figure 56 Impedance (Z^*) and dielectric modulus (M^*) spectra of nanocrystalline (a) and (b) 0.6%Nb-doped SrTiO₃ and (c) and (d) 3at%Nb-SrTiO₃ acquired at 550°C and $P = 1$ bar.

Interestingly, the conductivity minimum of the 3at% Nb-doped sample could be experimentally observed at $P = 10^{-2}$ bar. At this point the conductivity mechanism switches from p-type to n-type and this is also confirmed by a strong change in the activation energy ($\Delta E = 1.83$ eV at $P = 10^{-5}$ bar).

In reducing conditions the nanomaterials are all n-type with a P -dependence of $-1/4$, which is evidence of n-type conductivity according to Eq. 2.28. If one now observes the isotherms depicted in Figure 58 it turns out that, as expected (see Figure 9), increasing the Nb content the p-type conductivity decreases on increasing the Nb content, whereas the n-type conductivity increases. This generates a shift of the conductivity minimum towards higher values of oxygen partial pressure, while increasing $[Nb_{Ti}^{\bullet}]$.

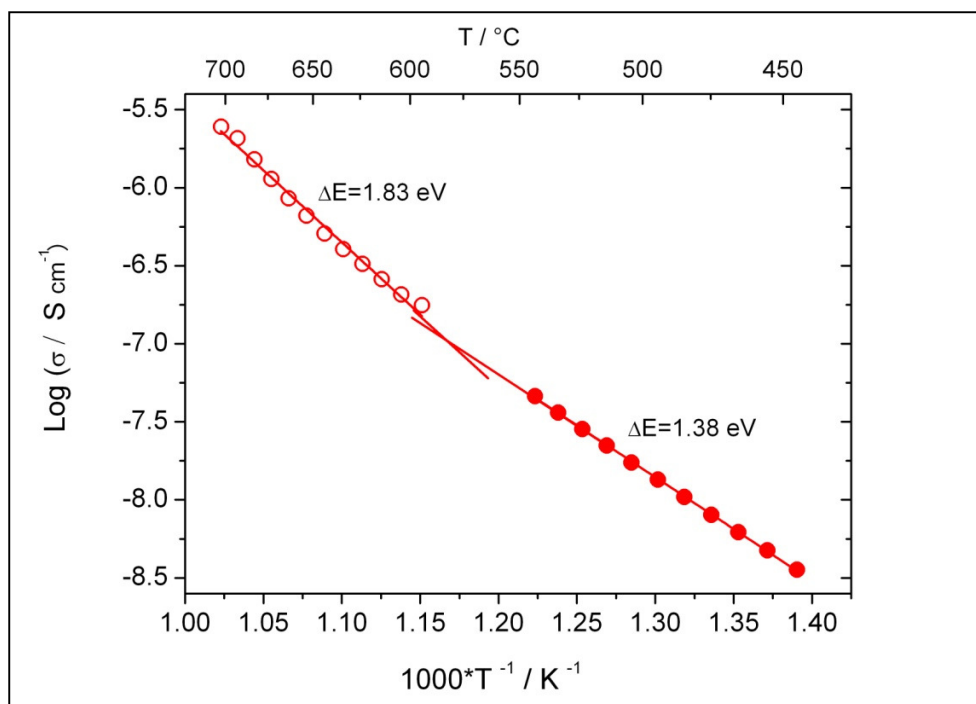


Figure 57 T-dependence of the conductivity for the 3at% Nb-SrTiO₃ at $P = 1$ bar. The sample was first equilibrated at 550°C and then the conductivity was measured in the range 550-450°C (**solid circles**). After that, the sample was annealed at 700°C for several hours and the conductivity was measured in the range 700-600°C (**open circles**).

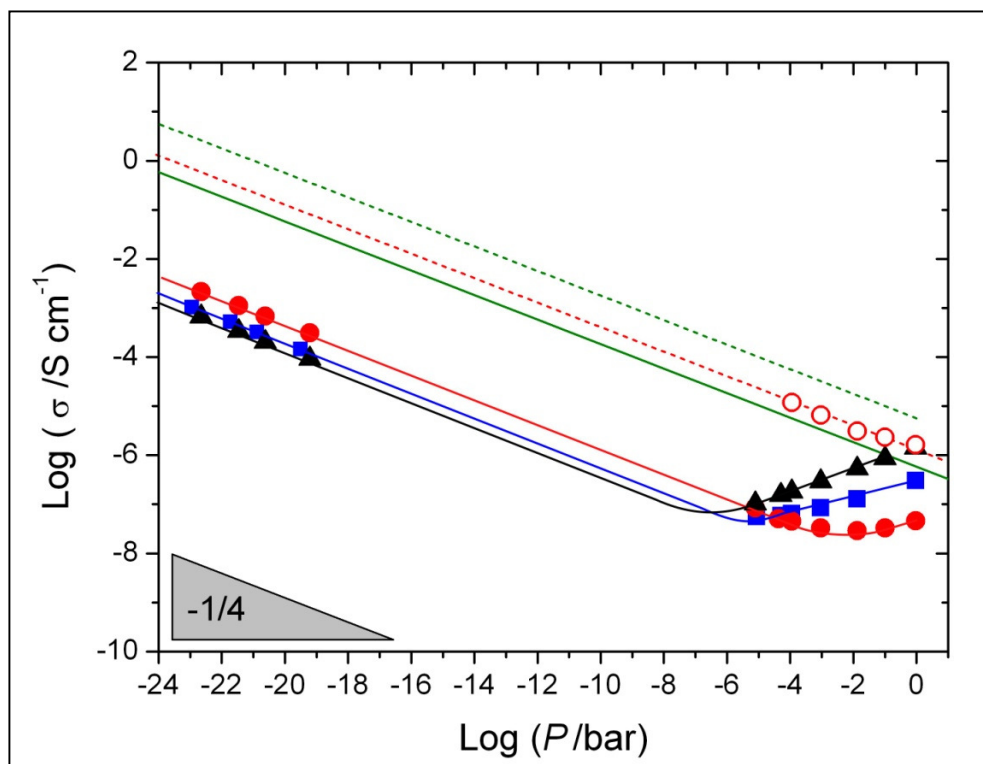


Figure 58 P -dependence of the conductivity. The symbols are assigned as follows: (**black triangles**) undoped SrTiO₃ at 550°C; (**blue squares**) 0.6at% Nb-doped SrTiO₃ at 550°C; (**solid red circles**) 3at% Nb-doped SrTiO₃ at 550°C; (**open red circles**) 3at% Nb-doped SrTiO₃ at 700°C; The green lines refer to the theoretical conductivity of 3at% Nb-doped STO according to Moos *et al.*^[41] using the electron mobilities of Denk *et al.*^[39] at 550°C (solid) and at 700°C (dotted).

In particular at $P = 1$ bar the difference in the p-type conductivity between the 0.6at% and the 3at% is a factor 5, which corresponds to the difference in the Nb content.^{***} The comparison with the nanocrystalline undoped sample would point towards the fact that donors are compensated by electrons ($n = [Nb_{Ti}^{\bullet}]$), due to the strong reducing sintering conditions.

A key point here is to understand the reasons of the disappearance of the bulk contribution. It is known that the overlapping of the space charge layers causes the annihilation of the bulk, giving origin to the mesoscopic regime. Here, the grain size is approximately 30 nm according to the TEM micrographs. The space charge layer width λ^* , determined according to the Mott-Schottky model, is then 12 nm for the 0.6at% Nb-SrTiO₃ and 6 nm for the 3at% one. This would explain the mesoscopic regime only for the material with a lower Nb content. Being able to exclude Nb segregation towards the GBs according to the TEM-EDX investigation which could increase the space charge layer width and excluding that Nb leaves the material during the sintering process,^{†††} the reason of the disappearance of the bulk contribution must lie elsewhere. It must be borne in mind that the single crystal conductivity, which corresponds the bulk contribution in a polycrystalline material, is very high.^[185,192] As reference, the conductivity of a 0.6at% Nb-doped single crystal was measured at room temperature obtaining $\sigma_{bulk} = 10 \text{ S/cm}$ in agreement with data reported in ref. [81]. Therefore, the bulk contribution cannot be resolved at high temperatures in the impedance (Z^*) spectra of nanocrystalline sample, which exhibit a total conductivity in the order of 10^{-8} S/cm (the corresponding resistance is approximately 10^6 Ohm – see Figure 56a).

This is also the case of donor doped BaTiO₃, characterized by the positive resistance coefficient (PTC) effect, in which the bulk contribution cannot be resolved by means of impedance spectroscopy above the Curie temperature, when the GB resistivity increases of several orders of magnitude.^[189-190]

^{***} It is worth noting here that 0.6at% La-doped SrTiO₃ showed the same behaviour of the 0.6at% Nb-doped material.

^{†††} ICP-OES confirmed the presence of 3at% Nb in the nanopowders after calcination.

Let us now consider the M^* -plot. Under the assumption of the brick layer model^[15] and considering the same dielectric constant in the bulk and in the space charge region

$$\frac{C_{GB}}{C_{bulk}} = \frac{(d_g - 2\lambda^*)}{2\lambda^*} \quad 4.22$$

results.

Considering now a space charge layer width $\lambda^* = 6\text{ nm}$ and a grain size d_g of approximately 30 nm, one would expect a similar capacitance for the bulk and the GBs. However, the bulk is characterized by relaxation time constant which is orders of magnitude lower than the GB one, due to the low resistance. This makes impossible to resolve the bulk contribution also in the M^* -plot.

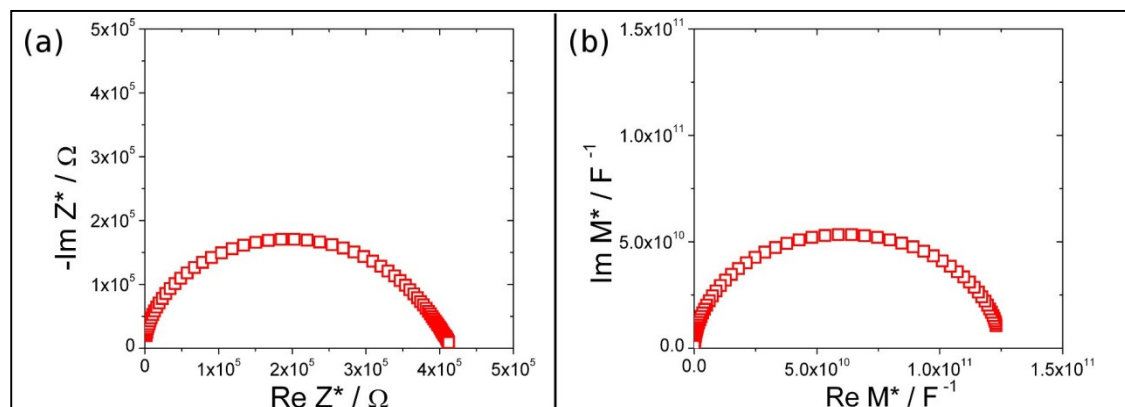


Figure 59 Impedance (a) and dielectric modulus (b) spectra 3at%Nb-STO after annealing for several hours at 700°C and $P = 1$ bar.

In order to have more information about the GB behaviour, the 3at% nanocrystalline sample was annealed in O_2 at 700°C for several hours. In this case, the spectra are still characterized by single arcs (Figure 59). If one now carefully observes the temperature dependence of the total conductivity in the temperature range 700-600°C reported in Figure 57 (open red dots), it turns out that this contribution corresponds to the contribution observed in the as-SPSed sample. The single arc is characterized by an activation energy of 1.83 eV, which is the same of the as-SPSed sample between 550 and 450°C at 10^{-5} bar (1.83 eV), when the material turns out to be n-type conductor. It is worth noting here, that this value is typical for donor-doped $SrTiO_3$ as well as for $BaTiO_3$.^[193-195] A similar variation of the activation energies with temperature was observed by Hou *et al.* in donor doped $BaTiO_3$.^[189] In our case, this

can be easily explained by a switch of the conduction mechanism of the GBs p-type to n-type at about 600°C.

Moreover, since we know from the P -dependence of the conductivity that this contribution is also n-type at 700°C with a P -dependence of $-1/4$ (see open red circles in Figure 58), we can conclude that also in the annealed sample we observed only the grain boundary contribution.

As in the case of the acceptor doped material,^[42] also in the donor doped one the conductivity minimum shifts towards higher values of P , while increasing the temperature of the isotherm.

It has to be mentioned that the conductivity at 700°C is lower than the one that can be extrapolated from the data reported by Balachandran and Erer for polycrystalline La-doped SrTiO₃ for higher temperatures, taking into account the activation energy ($\sigma_{tot} = 6 \cdot 10^{-6} S/cm$ at 700°C).^[101] The theoretical conductivity at 700°C according to the defect chemistry model of Moos *et al.*^[41], determined using the electron mobility of Denk *et al.*,^[39] is depicted in Figure 58 (dashed green line). It can be observed that the experimental values are lower than the theoretical ones. The discrepancy becomes much stronger at 550°C (compare the red solid line with the green solid one in Figure 58). This can be ascribed to the fact that the defect chemistry model by Moos *et al.*^[41] does not hold at low temperatures.

Notably, these findings give the possibility to understand the role of the grain boundaries in donor doped SrTiO₃. It is clear here that the fact that the resistances of the grain boundaries are orders of magnitude higher than the bulk one in the case of n-type material points towards a blocking effect at the grain boundaries. As mentioned at the beginning of this section the origin of this effect has not yet been clarified. However, the observation of p-type conductivity under oxidizing conditions would suggest an enrichment of electron holes and a depletion of electrons in the space charge region, which has to be ascribed to the presence of a negative space charge potential. It is worth noting that in presence of a negative space charge potential, in the p-type regime the conduction would be dominated by the highly conductive boundaries, which would short-circuit the bulk. The origin of such potential could be due to a segregation of acceptor states at the GBs.

Section conclusions:

In this section, nanocrystalline donor (Nb) doped SrTiO₃ was investigated. The nanopowders were synthesized according to the solvothermal method and densified via spark plasma sintering. The electrical properties determined by means of impedance spectroscopy revealed only the GB contribution. Here, the disappearance of the highly conductive bulk contribution has to be ascribed to a lack of resolution.

Unexpected p-type conductivity was observed at 550°C in the high oxygen partial pressure regime, which is a new feature for donor doped SrTiO₃. The typical n-type conductivity was re-established via a reduction of the oxygen partial pressure and/or an increase of temperature. However, grain boundaries are blocking for the electron transport and this, together with the enrichment of electron holes in the space charge region, confirmed by observed the p-type conductivity, suggests the presence of a negative space charge potential in donor doped SrTiO₃.^[196]

Conclusions

The present thesis deals with the investigation of the grain boundary electrical properties of strontium titanate in terms of charge carrier defect chemistry. The results have been understood in the light of the space charge model, which explains the charge redistribution in the region adjacent to the grain boundaries, as a consequence of the excess of positive charge in the grain boundary core.

Special attention is paid to nanocrystalline materials in which the grain boundaries are so close to each other that they dominate the overall conduction properties of the material, giving origin to novel conductors.

SrTiO₃ (undoped and homogeneously doped) was considered a model system for the electroceramic oxides in general and for the family of perovskites in particular, in view of the defect chemistry model developed in the past decades for the macroscopic situation, which allowed a better understanding of the properties at the nanoscale.

The nanocrystalline powders were synthesized according to three different procedures, namely co-precipitation, combustion and solvothermal and then sintered at relatively low temperatures via spark plasma sintering in order to limit the grain growth.

In this way dense pellets were obtained, whose electrical properties strongly deviated from the well known (in terms of transport and defect chemistry) macroscopic behaviour. The most striking results consisted in the reduction of the p-type conductivity and of the consequent increase of the n-type conductivity of several orders

of magnitude, together with an even stronger depression of the ionic conductivity. Moreover, the conductivity minimum shifted of 12 decades toward higher values of oxygen partial pressure. This behaviour can be nicely explained as in the mesoscopic regime the space charge layer (in which the charge carriers are redistributed due to the positive charge of the grain boundary core) overlapped and controlled the transport properties of the material, annihilating the bulk.

The charge density of the grain boundary core Σ was also considered and it was observed to decrease on increasing the oxygen partial pressure. This observation is consistent with the assumption that the charge of the GB core is due to an excess of oxygen vacancies, whose concentration increase as oxygen leaves when the environment becomes more reducing. The P -dependence of Σ is however significantly lower than the one of the charge carriers in the bulk.

Similar size effects have been also observed in acceptor doped SrTiO₃ with high Fe contents. Also in this case the materials are fully mesoscopic leading to an increase of p-type conductivity and a decrease of n-type conductivity. It was also observed that the activation energy of the GB conductivity, which is related to the space charge potential, decreased with increased of Fe content.

However, the grain boundary properties can be tuned by addition of the dopant only at the grain boundaries. In this case a core-shell situation is established, in which the highly conductive shell dominated the conduction properties. However, spark plasma sintering limited the diffusion of Fe from the GBs into the shell and the Fe left in the GB core increases the space charge potential of the decorated material compared to the homogeneously doped sample. It can be concluded that the spatial distribution of the dopant plays a role in the determination of the overall properties of the material, especially in the mesoscopic regime, in which the GBs predominate over the bulk. The same approach have shown interesting results also in nanocrystalline cerium oxide, which are reported in the appendix of this thesis.

In addition also nanocrystalline donor doped SrTiO₃ was investigated for the first time. Unexpected p-type conductivity was observed at 550°C in the high oxygen partial pressure regime. Furthermore, the grain boundaries exhibit a blocking effect to the electron transport when the material becomes n-type conductor. These findings would suggest the presence of a negative space charge potential in donor doped SrTiO₃,

which generates the enrichment of holes and the depletion of electrons within the space charge region.

In conclusion, these fundamental investigations on the electrical properties of the grain boundaries of a model system, such SrTiO₃, demonstrated the impact that the grain size has on the overall properties of the materials and confirmed the possibility of further adjusting the transport properties by controlling grain size and charge of grain boundaries.

Appendix

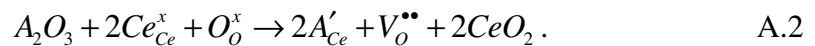
A.1 Effect of grain boundary decoration on the electrical conduction of nanocrystalline CeO₂

The approach of the GB decoration with the final goal of obtaining an enhancement of the ionic conductivity was also employed for cerium dioxide (CeO₂), which is another extensively studied mixed ionic and electronic conducting oxide. Thanks to the high ionic conductivity at intermediate temperatures if acceptor doped, CeO₂ finds several important applications, e.g. it is widely used as electrolyte for solid oxide fuel cells (SOFCs).^[17,197]

Its mixed conductivity is due to oxygen non-stoichiometry, when CeO₂ is reduced to CeO_{2-x}. One may describe the reduction of ceria by the defect reaction 2.7 as in the case of SrTiO₃, which leads to:^[198,199]

$$n \propto P^{-1/6} . \quad \text{A.1}$$

When CeO₂ is doped with trivalent cations which act as acceptors A'_{Ce} , the formation of oxygen vacancies is induced to maintain the electroneutrality:



In this case, the oxygen vacancy concentration is increased and oxygen vacancies $V_O^{\bullet\bullet}$ become the predominant conduction defects in the material.*

* It is worth noting here that nominally pure CeO₂ is usually slightly acceptor doped, as the main intrinsic impurities are lower-valence cations.

Consequently acceptor doped CeO₂ does not show any P -dependence of the conductivity in oxidizing conditions, since the oxygen vacancy concentration is constant, as it is fixed by the dopant content and much higher than the electron concentration:

$$[A'_{Ce}] = 2v \gg n. \quad \text{A.3}$$

Similarly to other conducting oxides (e.g. ZrO₂, SrTiO₃) the GBs significantly influence the ionic transport properties of this material since the GB core is positively charged, which induces a depletion of the positively charged oxygen vacancies ($V_O^{\bullet\bullet}$) in the space charge layer,^[172] and hence a reduction of the total ionic conductivity.^[19-20] At the same time, due to the positive potential, excess electrons are accumulated in the SCL, giving origin to increased n-type conductivity. As observed in SrTiO₃, such effects are amplified in nanocrystalline materials.^[18,20-26]

The goal of this part of the study consists in systematically modifying the GB electrical properties of undoped nanocrystalline CeO₂, by selectively doping the grain boundaries (*GB decoration*) with trivalent cations (Y, Yb, Bi)[†] characterized by different ionic radii. The spatial distribution of the dopant upon sintering (either at the GB core or diffused within the grain) should play a crucial role for a full understanding of the conduction mechanism in the final decorated materials. The concept is similar to what already discussed in section 4.4 for Fe-doped SrTiO₃.

Therefore, a combined impedance spectroscopy and microstructural study was carried out. In particular, to complement X-ray diffraction and investigate the dopant distribution, Extended X-ray Absorption Fine Structure (EXAFS) have been employed. This technique probes the local environment of a given element and allows to determine the final position of the dopant initially located at the grain surface before sintering. For comparison, ceria was also homogeneously doped with the same cations, in order to have a reference for the decorated samples.

Nanocrystalline cerium oxide was doped yttrium, ytterbium and bismuth. The dopant concentration chosen was 6at%. The nanopowders were prepared in two different ways in order to obtain a different distribution of the dopant: (i) in the

[†] Although there are some trivalent cations which give higher ionic conductivity (i.e. Gd and Sm), the choice of the dopants was made in order to ensure reliable EXAFS measurements within the energy range of the beamline at the Synchrotron Elettra, Trieste (Italy).

homogenous samples the dopant was homogeneously distributed throughout the grain, whereas (ii) in the *decorated* samples the dopant was added only on the surface of the grain of the powders, with the purpose of modifying the grain boundary properties of the final material.

The electrical conduction properties of the sintered pellets were measured via impedance spectroscopy, with oxygen partial pressure P ranging from 1 bar to 10^{-4} bar. The samples were equilibrated at the desired P for 20 hours before acquiring the final spectrum. The activation energy of the conductivity was determined from the impedance spectra acquired every 10°C between 500°C and 400°C at $P = 1$ bar and at $P = 10^{-4}$ bar.

The results of the chemical analyses performed via ICP-OES revealed that for all compositions, the dopant (acceptor) content is slightly lower than the nominal value and ranges from 4.64 at% (homogeneously doped Y:CeO₂) to 5.77 at% (decorated Y:CeO₂).

The XRD patterns acquired from the powders before sintering and from the sintered pellets are depicted in Figure 60. No second phase can be detected in all samples. The results of the Rietveld refinement performed on the patterns are summarized in Table XII.

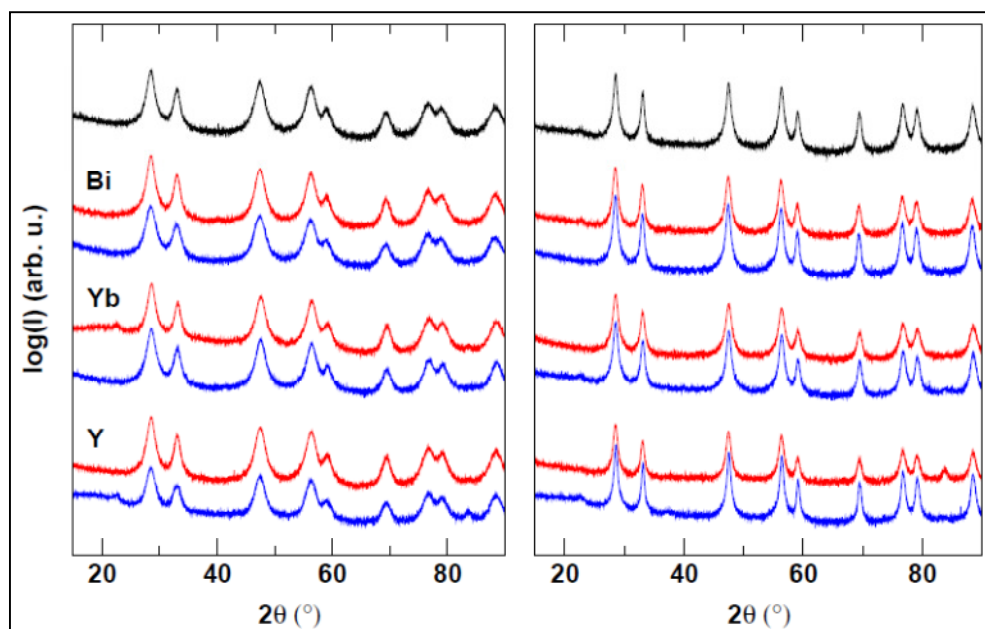


Figure 60 Left panel: XRD patterns of the powders before sintering. Right panel: XRD patterns of the sintered samples. The colours are assigned as follows: blue for homogeneously doped, red for decorated and black for undoped CeO₂. The peaks appearing in some case at about 25° and at 85° are artefacts due to the sample holder. Reproduced from ref. [200] with permission of The Electrochemical Society.

Table XII Results of the Rietveld refinement on the XRD data: unit cell parameter a , strain, grain size d_g and residual $R(F^2)$. The uncertainty is reported in parentheses for unit cell parameter; the uncertainty for size and strain is around 10%. The labels h and d refer to the homogeneously doped and the decorated samples, respectively whereas the abbreviation *sint* allows for distinguishing the sintered samples from the uncompact powders.

Sample	a [Å]	Strain [%]	Grain size d_g [nm]	$R(F^2)$ [%]
<i>Undoped CeO₂</i>	5.4093(3)	1.7	11	3.4
<i>Yb:CeO₂ h</i>	5.403(1)	1	8	3.2
<i>Yb:CeO₂ d</i>	5.406(1)	1.9	13	3.1
<i>Y:CeO₂ h</i>	5.404(1)	0.1	6	6.2
<i>Y:CeO₂ d</i>	5.406(1)	1.3	10	4.6
<i>Bi:CeO₂ h</i>	5.4256(4)	0.8	6	3.7
<i>Bi:CeO₂ d</i>	5.410(1)	2.2	14	2.6
<i>Undoped CeO₂ sint</i>	5.4081(6)	1.8	18	3.9
<i>Yb:CeO₂ h sint</i>	5.4046(4)	0.1	15	1.8
<i>Yb:CeO₂ d sint</i>	5.4036(6)	0.6	16	3.1
<i>Y:CeO₂ h sint</i>	5.4160(2)	1.1	23	2.6
<i>Y:CeO₂ d sint</i>	5.4081(3)	0.1	13	5.4
<i>Bi:CeO₂ h sint</i>	5.4201(1)	0.1	18	2.9
<i>Bi:CeO₂ d sint</i>	5.4129(5)	0.6	18	2.7

This analysis provides important pieces of information from the XRD data. Firstly, the shift of the lattice parameter with respect to pure CeO₂ can be interpreted as an indication of dopant insertion inside the bulk of the fluorite lattice. In this respect, the lattice parameters roughly follow the ionic radii, i.e. (Bi³⁺) > (Y³⁺) > (Ce⁴⁺) > (Yb³⁺), at least for the sintered homogeneously doped samples. It is worth noting that neither powders, nor sintered decorated samples, strictly follow this trend, due to the fact that the dopant distribution is not perfectly homogeneous inside the coherently-scattering domains probed by XRD. The average grain size of the sintered samples lies in the nanometric range, spanning from 13 to 23 nm. While Yb:CeO₂ and Bi:CeO₂ do not exhibit significant size differences between doped and decorated specimens (15 vs. 16 nm for the former and 18 vs. 18 nm for the latter), Y:CeO₂ displays the strongest variation (23 vs. 13 nm). In general, strain magnitude is lower in sintered and homogeneously doped samples, and it is higher in powders and decorated samples.

EXAFS analysis confirmed that there is no segregation of poorly crystallized phases at the grain boundaries.[‡] On the other hand, there is a clear difference in the dopant distributions between decorated and doped sintered samples. This is supported by the analysis of both the Ce and the dopant environments. The homogeneously doped samples showed consistently higher disorder factors in the Ce⁴⁺ environment, meaning that dopant ions are spread more evenly in the grain interior, perturbing the environment of a greater number of Ce sites. On the contrary, the dopant environment shows a lower disorder in the homogeneously doped sintered samples, since dopant atoms are homogeneously placed in a single environment, without local accumulation.

The electrochemical characterization by impedance spectroscopy revealed intriguing effects of the GB decoration on the electrical conduction properties of CeO₂. The impedance spectra acquired in oxygen of the sintered samples are reported in Figure 61 and the values of the activation energies determined from the temperature dependence of the conductivity are summarized in Table XIII.

Homogeneously doped samples

At first undoped CeO₂ was considered as reference. A characteristic spectrum is shown in Figure 61g. it is composed by only one semicircle and for the fitting a single RQ circuit was used.

The single contribution was assigned to the GBs by taking into account the values of the activation energy and the capacitance, from which the value of the dielectric constant $\epsilon = 45$ was calculated. The P -dependence of the conductivity (see black triangles in Figure 62) showed a negative exponent equal to $-1/6$, indicating n-type conductivity. The results for the undoped nanocrystalline CeO₂ are in very good agreement with ref.s [18,169].

On the other hand, the spectra of the Y and Yb homogeneously doped CeO₂ are characterized by a single arc with positive intercept in the high frequency range on the real axis (Figure 61a, c). The equivalent circuit used for the fitting was composed by a resistance placed in series with a RC element. The additional resistance was assigned to the bulk contribution, R_{bulk} , in accordance with its corresponding activation energy ΔE being in the range of the characteristic value of the migration enthalpy of $V_o^{\bullet\bullet}$ in

[‡] The detailed analysis of the EXAFS results is reported in ref. [175].

CeO₂.^[17,168,201] The spectra of the homogenously Bi-doped were fitted with two RQ circuits in series, which were assigned to the bulk and GB contribution.

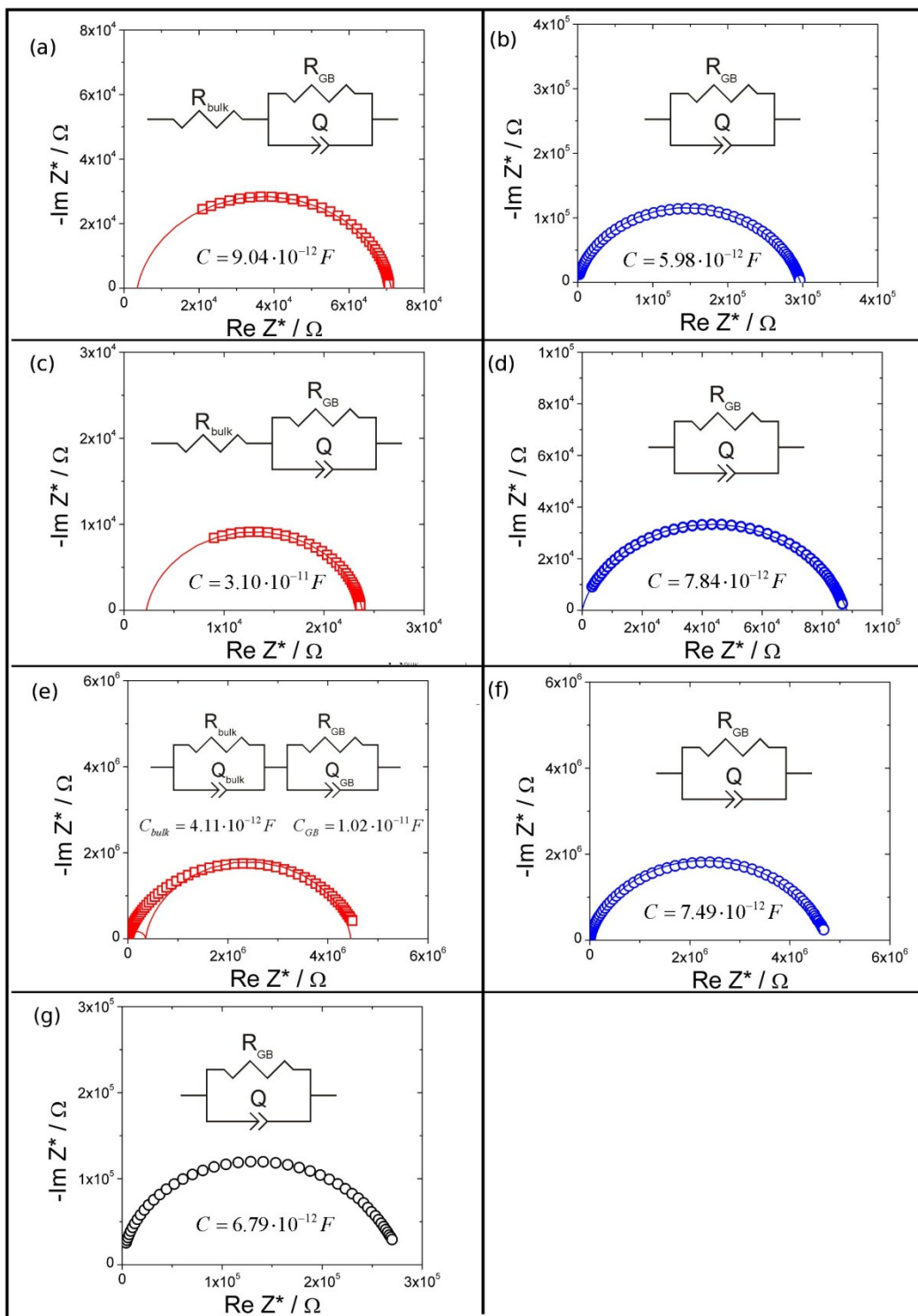


Figure 61 Impedance spectra acquired at 400°C and $P = 1$ bar. Note that only spectrum (g) was taken at 500°C. The red data points refer to the homogenous samples, the blue to the decorated. (a) and (b) refers to Yb:CeO₂; (c) and (d) to Y:CeO₂; (e) and (f) to Bi:CeO₂; (g) to the undoped CeO₂. The equivalent circuits used to fit the spectra are shown in each panel. Reproduced from ref. [200] with permission of The Electrochemical Society.

As expected for the significant doping content, in the homogenously doped CeO₂, neither the bulk nor the GB conductivity exhibits any P -dependence (see Figure 62a and Figure 62b), indicating the electric conduction to be determined by V_o^{**} transport.

Table XIII Activation energies of the electrical conductivity determined at $P = 1$ bar. No bulk contribution is observed either in the undoped material or in the decorated samples.

Sample	Bulk [eV]	GB [eV]
<i>Undoped CeO₂</i>	---	1.20
<i>Yb:CeO₂</i>	<i>Homogenous</i>	0.63
	<i>Decorated</i>	---
<i>Y:CeO₂</i>	<i>Homogenous</i>	0.50
	<i>Decorated</i>	---
<i>Bi:CeO₂</i>	<i>Homogenous</i>	0.88
	<i>Decorated</i>	---

For Y:CeO₂ and Yb:CeO₂ the bulk conductivity σ_{bulk}^{hom} agrees perfectly with the theoretical conductivity of 6at% acceptor doped CeO₂, calculated using the oxygen vacancies mobility values from ref. [24]. The minor differences in the bulk conductivities between Y and Yb doped samples might be ascribed to different V_o^{**} mobilities, which is well known to vary perceptibly with the dopant cation, as already observed by Eguchi *et al.*^[202] The second contribution, represented by the low frequency arc in the impedance spectra is assigned to the GBs. The ΔE value is typical for the GBs of heavily doped CeO₂,^[27] but, except Bi:CeO₂, somewhat lower than the one of the undoped material.

The situation is slightly different for Bi:CeO₂. The bulk conductivity is much lower than the theoretical value, which may indicate either a lower oxygen vacancy mobility or an effective dopant concentration lower than expected (e.g. due to a change of valence of the Bi cation). Also the ΔE are higher compared to the Y and Yb homogenous samples and ΔE_{bulk} is in agreement with the values previously reported in ref. [203].

Under the assumption of a Mott-Schottky situation, the grain boundary conductivity $\sigma_{GB}^{\perp, hom}$ can be derived by taking into consideration the relaxation time constants τ_{bulk} and τ_{gb} according to Eq. 2.56. [172]

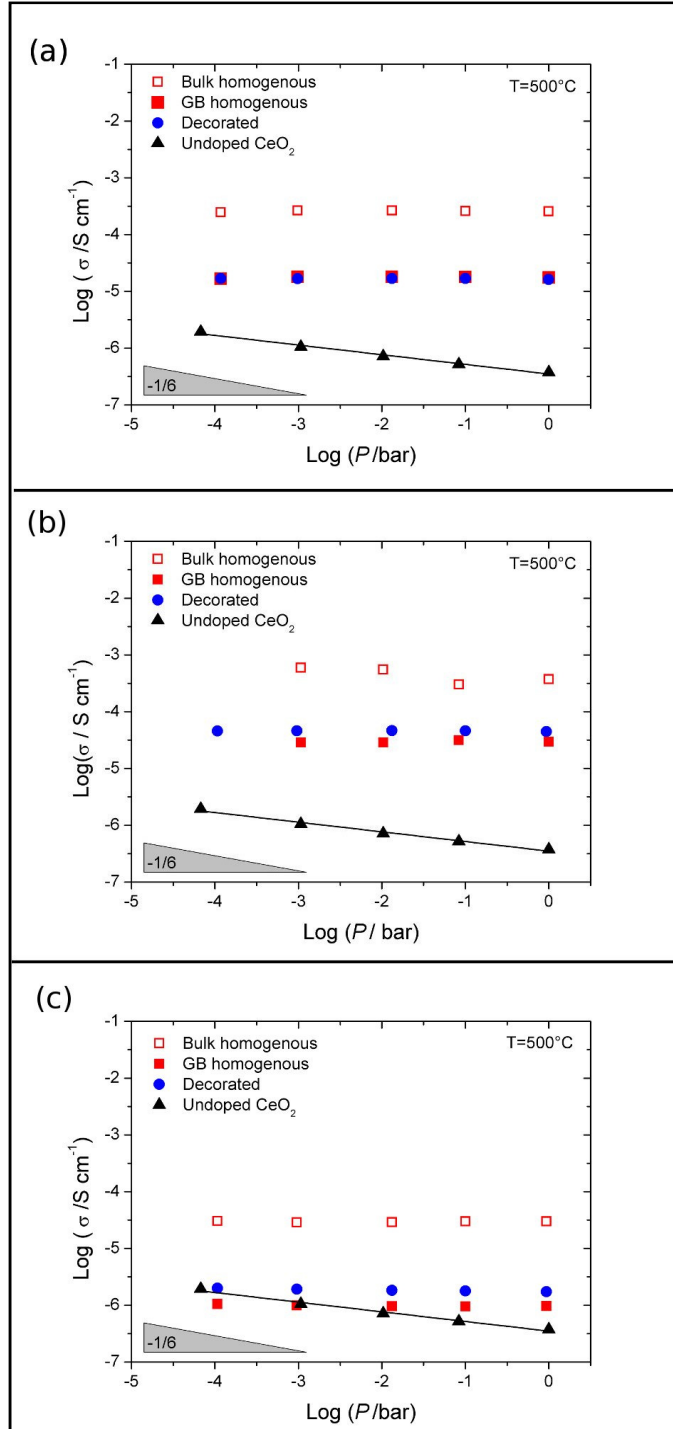


Figure 62 P dependence of the conductivity measured at 500°C; (a) Yb:CeO₂; (b) Y:CeO₂; (c) Bi:CeO₂. These samples were sintered at 800°C for 30 min. Note that for the homogeneous sample the GB conductivity is $\bar{\sigma}_{GB}^{\perp}$ determined according to Eq. 2.54, whereas the conductivity of the decorated samples is σ_m^{dec} . Reproduced from ref. [200] with permission of The Electrochemical Society.

Although the bulk capacitance cannot be determined from the fitting, C_{bulk} , and hence τ_{bulk}^{hom} , can be estimated assuming $\epsilon_{bulk} = 25$, which is a typical value of the dielectric constant for acceptor doped CeO_2 .^[18-19]

In the Mott-Schottky approximation (homogeneously doped samples and immobile cations), the space charge potential $\Delta\phi_0$ can be determined by solving numerically Eq. 2.54, yielding for the Yb-doped samples $\Delta\phi_0 = 0.17$ V for the Yb-doped samples and $\Delta\phi_0 = 0.17$ V for the Y-doped one $\Delta\phi_0 = 0.17$ V whereas for the Bi-doped sample $\Delta\phi_0 = 0.21$. These values are all rather low compared to the ones already determined for acceptor doped CeO_2 , which were found to be around 0.30 V.^[18-19] As explained for $SrTiO_3$, $\Delta\phi_0$ being dependent on the bulk composition, is not a good parameter for comparing different samples. A better parameter is the excess charge Σ at the grain boundary core, given by Eq. 2.48 for the Mott-Schottky case.

Decorated samples

In the case of the decorated samples (sintered at 800°C for 30 min) the impedance spectra are characterized by only one semicircle. As shown in Figure 62, the conductivity is independent of the P indicating that it is ionic. The dielectric constant ϵ_m^{dec} calculated from the measured capacitance values is 45. It is also worth noting that, for the decorated samples, the fitting parameter α (Eq. 3.5) is systematically lower than for the GB contribution of the homogeneously doped specimens (0.80 vs. 0.95, respectively). This is a consequence of different GB properties between the two sets of samples and specifically it might be due to an inhomogeneous dopant distribution in the decorated samples.

The measured conductivity and dielectric constant of the decorated samples σ_m^{dec} , ϵ_m^{dec} were calculated directly from the geometry of the sample and thus represent the effective overall conductivity and the effective overall dielectric constant of the material. In spite of the differences between Y, Yb and Bi decorated samples, the following results are remarkable: (i) the activation energies of σ_m^{dec} and $\sigma_{m,GB}^{\perp,hom}$ are practically identical (see Table XIII), (ii) for σ_m^{dec} and $\sigma_{GB}^{\perp,hom}$ even the absolute values are quite close (see Figure 62) and (iii) $\epsilon_m^{dec} \approx \epsilon_{bulk}$.

Furthermore, the values of ΔE^{dec} of the decorated samples are identical to those of the GB activation energy of the homogeneous samples ΔE_{GB}^{hom} (see Table XIII) and the measured value of conductivity of the decorated ceria σ_m^{dec} is very close to the local (averaged) grain boundary conductivity for the homogeneously doped samples $\bar{\sigma}_{GB}^{\perp,hom}$ calculated according to Eq. 2.56.

This excludes the possibility of the creation of a negative space charge potential, which would make the GB response disappear, because this is in contradiction with the experimental findings (activation energy values).

The second possibility is that the space charge potential is positive but the material is in the mesoscopic regime, in which the bulk response must disappear due to the overlapping of the space charge layers (as already observed in nanocrystalline SrTiO₃). However, σ_m^{dec} corresponds to an acceptor concentration of about 0.6 at%, which gives origin to $2\lambda^* \approx 5 \text{ nm}$ [§]. This is clearly not consistent with a mesoscopic situation ($2\lambda^* > d_g$).

Rather the results find their explanation by considering a more complex dopant distribution. As the EXAFS data indicate that most acceptors have indeed entered the fluorite structure a significant amount of such trivalent cations diffused during sintering. Notably, the diffusion depth l must be limited, i.e. $2l < d_g$, because otherwise two contributions would appear in the impedance spectra.

Thus, the grains of the decorated samples are characterized by a core-shell configuration, in which the grain interior remains undoped, while the thin shell is heavily doped. It is important to note that the grain interior does not contribute to the ionic conduction simply because the impurity (acceptor) concentration is very low.

This means that the ionic transport occurs through the short-circuiting shells. This is supported also by the value of the relative dielectric constant ($\epsilon_m^{dec} = 30$) obtained from these spectra, which is characteristic of the bulk.^{**} It is important to note that the presence of a single contribution in the Nyquist plots indicate that the shell is in

[§] The extent λ^* of the space charge layer can be determined according to eqn. 2.45. Note that, for an acceptor concentration of 0.6%, $\epsilon_{bulk} = 25$ and $\Delta\phi_0 = 0.15 \text{ V}$, one obtains $2\lambda^* \sim 5 \text{ nm}$, which is clearly smaller than the average grain size of the nanocrystalline samples considered here (see Table XII).

^{**} When the boundaries are the preferential pathways for the charge carriers migration, the corresponding capacitance value is the one of the bulk as shown in ref. [18].

the mesoscopic situation ($l \leq 2\lambda^{*,dec}$). In view of the small value of l , the shell is mesoscopic or at least close to the mesoscopic regime.

The coincidence of the absolute values for σ_m^{dec} and $\sigma_{GB}^{\perp,hom}$ is explained if one considers the case of a flat V_o^{**} profile, in which the concentration $[V_o^{**}]$ is given by the boundary value, and deconvolutes the conduction pathways according to the brick layer model. Now knowing that $\Delta E^{dec} = \Delta E_{GB}^{hom}$ and considering constant the excess charge in the GB core ($\Sigma^{dec} \approx \Sigma^{hom}$),

$$\sigma_m^{dec} = 0.7 \sigma_{GB}^{\perp,hom}. \quad A.4$$

results.^[200]

It is also clear that these inhomogeneities (relative to the V_o^{**} profiles) cannot be very pronounced as otherwise one needs to reckon with the appearance of a second shell-related impedance arc and to an increase of ϵ_m^{dec} over ϵ_{bulk} . Hence one can conclude that the decorated samples are characterized by an inhomogeneous dopant distribution consisting of a heavily doped shell, which on the one hand encloses an insulating core and on the other hand forms a (almost) mesoscopic depletion zone, the charge of which is compensated by the positive grain boundary charge (probably oxygen vacancies).

Section conclusions:

Homogeneously doped and decorated ceria (with 6 at% of Y, Yb and Bi) have been investigated. Microstructural (EXAFS) as well as electrical conductivity (impedance spectroscopy) measurements have been performed. The decorated samples were obtained by the addition of acceptor cations on the surface of the starting undoped ceria nanopowder. Notably, the decorated ceria exhibits only one electrical conductivity contribution, which is invariant with the oxygen partial pressure and thus ionic. The presence of the single ionic contribution is explained by taking into account a slight diffusion of acceptors towards the grain interior during sintering. As a consequence of such a diffusion process (which at 800°C involves a thin region adjacent the grain boundaries), a highly doped zone is created, which acts as a preferential pathway for the ionic transport. Remarkably, the heavily doped shell is in the mesoscopic regime.^[200]

A.2 Derivation of Eq. 4.10 and Eq. 4.14

$$Z_{GB}^{\perp} = \frac{\lambda^*}{|z_2| e u_2} \cdot \frac{1}{\left(2c_{2,0} \ln \frac{c_{2,\infty}}{c_{2,0}}\right)} \quad (\text{from ref. [25]})$$

$$Z_{GB}^{\perp} = \frac{\lambda^*}{e u_p} \cdot \frac{1}{\left(2p_0 \ln \frac{p_{\infty}}{p_0}\right)}$$

$$\sigma_{GB}^{\perp} = \frac{e u_p}{\left(\frac{2\varepsilon_0 \varepsilon_r \cdot \Delta\phi}{em}\right)^{1/2}} \cdot \left(2 \cdot \left(K_{ox} \frac{m}{2} P^{1/2}\right)^{1/2} \cdot e^{-\frac{\Delta\phi e}{kT}} \cdot \frac{\Delta\phi e}{kT}\right)$$

$$\text{Log} \sigma_{GB}^{\perp} = \text{Log} \left(\frac{2e^{3/2} u_p K_{ox}^{1/2}}{(2\varepsilon_0 \varepsilon_r)^{1/2}} \right) + \text{Log} m + \text{Log} P^{1/4} + \text{Log} \left(e^{-\frac{\Delta\phi e}{kT}} \right) + \text{Log} \left(\frac{\Delta\phi^{1/2} e}{kT} \right)$$

$$\frac{\partial \text{Log} \sigma_{GB}^{\perp}}{\partial \text{Log} P} = \frac{1}{4} + \frac{\partial \text{Log} m}{\partial \text{Log} P} - \frac{1}{2.303} \frac{\partial \left(\frac{\Delta\phi e}{kT} \right)}{\partial \text{Log} P} + \frac{1}{2} \frac{e}{kT} \frac{\partial \text{Log} (\Delta\phi)}{\partial \text{Log} P}$$

$$\Sigma = \sqrt{8\varepsilon_0 \varepsilon_r em \Delta\phi} \rightarrow \Delta\phi = \frac{\Sigma^2}{8\varepsilon_0 \varepsilon_r em}$$

$$\frac{\partial \text{Log} \sigma_{GB}^{\perp}}{\partial \text{Log} P} = \frac{1}{4} + \frac{\partial \text{Log} m}{\partial \text{Log} P} + \frac{1}{2} \frac{\partial \text{Log} \left(\frac{\Delta\phi e}{kT} \right)}{\partial \text{Log} P} - \frac{1}{2.303} \frac{\partial \left(\frac{\Delta\phi e}{kT} \right)}{\partial \text{Log} P}$$

$$\begin{aligned} \frac{\partial \text{Log} \sigma_{GB}^{\perp}}{\partial \text{Log} P} = & \frac{1}{4} + \frac{\partial \text{Log} m}{\partial \text{Log} P} + \frac{1}{2} \left(2 \cdot \frac{\partial \text{Log} \Sigma}{\partial \log P} - \frac{\partial \text{Log} m}{\partial \text{Log} P} \right) + \\ & - \frac{1}{2.303} \cdot \frac{1}{8\varepsilon_0 \varepsilon_r kT} \cdot \left[\left(\frac{\partial \Sigma}{\partial \log P} \cdot \frac{2\Sigma}{m} \right) - \left(\frac{\partial m}{\partial \text{Log} P} \cdot \left(\frac{\Sigma}{m} \right)^2 \right) \right] \end{aligned}$$

$$\frac{\partial \text{Log} \sigma_{GB}^{\perp}}{\partial \text{Log} P} \approx \frac{1}{4} + \frac{\partial \text{Log} m}{\partial \text{Log} P} - \frac{1}{18.4\varepsilon_0 \varepsilon_r kT} \cdot \left[\left(\frac{\partial \Sigma}{\partial \log P} \cdot \frac{2\Sigma}{m} \right) - \left(\frac{\partial m}{\partial \text{Log} P} \cdot \left(\frac{\Sigma}{m} \right)^2 \right) \right]$$

References

- [1] Maier, J., *Ionic-Conduction In-Space Charge Regions*, Progress In Solid State Chemistry **23** (1995) 171.
- [2] Maier, J., *Thermodynamic aspects and morphology of nano-structured ion conductors - Aspects of nano-ionics Part I*, Solid State Ionics **154** (2002) 291.
- [3] Maier, J., *Nano-sized mixed conductors (Aspects of nano-ionics. Part III)*, Solid State Ionics **148** (2002) 367.
- [4] Maier, J., *Defect chemistry and ion transport in nanostructured materials - Part II. Aspects of nanoionics*, Solid State Ionics **157** (2003) 327.
- [5] Maier, J., *Nano-ionics: Trivial and non-trivial size effects on ion conduction in solids*, Zeitschrift für Physikalische Chemie **217** (2003) 415.
- [6] Maier, J., *Ionic transport in nano-sized systems*, Solid State Ionics **175** (2004) 7.
- [7] Maier, J., *Nanoionics: ion transport and electrochemical storage in confined systems*, Nature Materials **4** (2005) 805.
- [8] Maier, J., *Physical Chemistry of Ionic Materials*. 2005, John Wiley & Sons, Ltd.
- [9] Maier, J., *Mass storage in space charge regions of nano-sized systems (Nano-ionics. Part V)*, Faraday Discussions **134** (2007) 51.
- [10] Maier, J., *Nanoionics: ionic charge carriers in small systems*, Physical Chemistry Chemical Physics **11** (2009) 3011.
- [11] Tuller, H.L., *Ionic conduction in nanocrystalline materials*, Solid State Ionics **131** (2000) 143.
- [12] Kröger, F.A. and H.J. Vink, *Relations between the Concentrations of Imperfections in Crystalline Solids*, Solid State Physics-Advances in Research and Applications **3** (1956) 307.
- [13] Maier, J., *Ionic and electronic carriers in solids: physical and chemical views of the equilibrium situation*, Solid State Ionics **143** (2001) 17.
- [14] Maier, J., *Defect chemistry at interfaces*, Solid State Ionics **70-71** (1994) 43.

- [15] Maier, J., *On the Conductivity of Polycrystalline Materials*, Berichte der Bunsen-Gesellschaft Phys. Chem **90** (1986) 26.
- [16] Maier, J., S. Prill, and B. Reichert, *Space charge effects in polycrystalline, micropolycrystalline and thin film samples: Application to AgCl and AgBr*, Solid State Ionics **28-30** (1988) 1465.
- [17] Tuller, H.L. and A.S. Nowick, *Doped Ceria as a Solid Oxide Electrolyte*, Journal of the Electrochemical Society **122** (1975) 255.
- [18] Kim, S. and J. Maier, *On the conductivity mechanism of nanocrystalline ceria*, Journal of the Electrochemical Society **149** (2002) J73.
- [19] Göbel, M.C., G. Gregori, X.X. Guo, and J. Maier, *Boundary effects on the electrical conductivity of pure and doped cerium oxide thin films*, Physical Chemistry Chemical Physics **12** (2010) 14351.
- [20] Chiang, Y.M., E.B. Lavik, I. Kosacki, H.L. Tuller, and J.Y. Ying, *Defect and transport properties of nanocrystalline CeO_{2-x}*, Applied Physics Letters **69** (1996) 185.
- [21] Chiang, Y.M., E.B. Lavik, I. Kosacki, H.L. Tuller, and J.Y. Ying, *Nonstoichiometry and electrical conductivity of nanocrystalline CeO_{2-x}*, Journal of Electroceramics **1** (1997) 7.
- [22] Hwang, J.H. and T.O. Mason, *Defect chemistry and transport properties of nanocrystalline cerium oxide*, Zeitschrift für Physikalische Chemie-International Journal of Research in Physical Chemistry & Chemical Physics **207** (1998) 21.
- [23] Tschöpe, A. and R. Birringer, *Grain size dependence of electrical conductivity in polycrystalline cerium oxide*, Journal of Electroceramics **7** (2001) 169.
- [24] Tschöpe, A., E. Sommer, and R. Birringer, *Grain size-dependent electrical conductivity of polycrystalline cerium oxide: I. Experiments*, Solid State Ionics **139** (2001) 255.
- [25] Tschöpe, A., *Grain size-dependent electrical conductivity of polycrystalline cerium oxide II: Space charge model*, Solid State Ionics **139** (2001) 267.
- [26] Kim, S., J. Fleig, and J. Maier, *Space charge conduction: Simple analytical solutions for ionic and mixed conductors and application to nanocrystalline ceria*, Physical Chemistry Chemical Physics **5** (2003) 2268.
- [27] Göbel, M.C., G. Gregori, and J. Maier, *Mixed conductivity in nanocrystalline highly acceptor doped cerium oxide thin films under oxidizing conditions*, Physical Chemistry Chemical Physics **13** (2011) 10940.
- [28] Sata, N., K. Eberman, K. Eberl, and J. Maier, *Mesoscopic fast ion conduction in nanometre-scale planar heterostructures*, Nature **408** (2000) 946.
- [29] Guo, X.X., I. Matei, J.S. Lee, and J. Maier, *Ion conduction across nanosized CaF₂/BaF₂ multilayer heterostructures*, Applied Physics Letters **91** (2007) 103102.
- [30] Guo, X.X., I. Matei, J. Jamnik, J.S. Lee, and J. Maier, *Defect chemical modeling of mesoscopic ion conduction in nanosized CaF₂/BaF₂ multilayer heterostructures*, Physical Review B **76** (2007) 125429.

- [31] Guo, X.X. and J. Maier, *Ionic Conducting Two-Dimensional Heterostructures*, *Advanced Materials* **21** (2009) 2619.
- [32] Jamnik, J. and J. Maier, *Nanocrystallinity effects in lithium battery materials - Aspects of nano-ionics. Part IV*, *Physical Chemistry Chemical Physics* **5** (2003) 5215.
- [33] Zhukovskii, Y.F., P. Balaya, E.A. Kotomin, and J. Maier, *Evidence for interfacial-storage anomaly in nanocomposites for lithium batteries from first-principles simulations*, *Physical Review Letters* **96** (2006).
- [34] Tuller, H.L. and S.R. Bishop, *Point Defects in Oxides: Tailoring Materials Through Defect Engineering*, *Annual Review of Materials Research* **41** (2011) 369.
- [35] Maier, J., *Space-charge regions in solid 2-phase systems and their conduction contribution .1. Conductance enhancement in the system Ionic Conductor-Inert Phase and application on AgCl-Al₂O₃ and AgCl-SiO₂*, *Journal of Physics and Chemistry of Solids* **46** (1985) 309.
- [36] Chan, N.H., R.K. Sharma, and D.M. Smyth, *Non-Stoichiometry in SrTiO₃*, *Journal of the Electrochemical Society* **128** (1981) 1762.
- [37] Balachandran, U. and N.G. Eror, *Electrical Conductivity in Strontium-Titanate*, *Journal of Solid State Chemistry* **39** (1981) 351.
- [38] Waser, R., *Bulk Conductivity and Defect Chemistry of Acceptor-Doped Strontium Titanate in the Quenched State*, *Journal of the American Ceramic Society* **74** (1991) 1934.
- [39] Denk, I., W. Munch, and J. Maier, *Partial conductivities in SrTiO₃: Bulk polarization experiments, oxygen concentration cell measurements, and defect-chemical modeling*, *Journal of the American Ceramic Society* **78** (1995) 3265.
- [40] Noll, F., W. Munch, I. Denk, and J. Maier, *SrTiO₃ as a prototype of a mixed conductor. Conductivities, oxygen diffusion and boundary effects*, *Solid State Ionics* **86-8** (1996) 711.
- [41] Moos, R. and K.H. Härdtl, *Defect chemistry of donor-doped and undoped strontium titanate ceramics between 1000°C and 1400°C*, *Journal of the American Ceramic Society* **80** (1997) 2549.
- [42] De Souza, R.A., J. Fleig, R. Merkle, and J. Maier, *SrTiO₃: a model electroceramic*, *Zeitschrift für Metallkunde* **94** (2003) 218.
- [43] Yamaoka, N., M. Masuyama, and M. Fukui, *SrTiO₃-base boundary-layer capacitor having varistor characteristics*, *American Ceramic Society Bulletin* **62** (1983) 698.
- [44] Brett, D.J.L., A. Atkinson, N.P. Brandon, and S.J. Skinner, *Intermediate temperature solid oxide fuel cells*, *Chemical Society Reviews* **37** (2008) 1568.
- [45] Ormerod, R.M., *Solid oxide fuel cells*, *Chemical Society Reviews* **32** (2003) 17.
- [46] Burnside, S., J.E. Moser, K. Brooks, M. Gratzel, and D. Cahen, *Nanocrystalline mesoporous strontium titanate as photoelectrode material for photosensitized solar devices: Increasing photovoltage through flatband potential engineering*, *Journal of Physical Chemistry B* **103** (1999) 9328.

- [47] Bandara, J. and H.C. Weerasinghe, *Enhancement of photovoltage of dye-sensitized solid-state solar cells by introducing high-band-gap oxide layers*, Solar Energy Materials and Solar Cells **88** (2005) 341.
- [48] Rothschild, A. and H.L. Tuller, *Gas sensors: New materials and processing approaches*, Journal of Electroceramics **17** (2006) 1005.
- [49] Fergus, J.W., *Perovskite oxides for semiconductor-based gas sensors*, Sensors and Actuators B-Chemical **123** (2007) 1169.
- [50] Rothschild, A., W. Menesklou, H.L. Tuller, and E. Ivers-Tiffée, *Electronic structure, defect chemistry, and transport properties of $SrTi_{1-x}Fe_xO_{3-y}$ solid solutions*, Chemistry of Materials **18** (2006) 3651.
- [51] Ivers-Tiffée, E., K.H. Härdtl, W. Menesklou, and J. Riegel, *Principles of solid state oxygen sensors for lean combustion gas control*, Electrochimica Acta **47** (2001) 807.
- [52] Guo, X., *Oxide-based gas sensors*, in *Lecture Notes of the 41st Spring School 2010*, Schriften des FZ Jülich.
- [53] Muta, H., K. Kurosaki, and S. Yamanaka, *Thermoelectric properties of rare earth doped $SrTiO_3$* , Journal of Alloys and Compounds **350** (2003) 292.
- [54] Ohta, S., *et al.*, *Large thermoelectric performance of heavily Nb-doped $SrTiO_3$ epitaxial film at high temperature*, Applied Physics Letters **87** (2005) 092108.
- [55] Liu, J., *et al.*, *Enhancement of thermoelectric efficiency in oxygen-deficient $Sr_{1-x}La_xTiO_{3-\delta}$ ceramics*, Applied Physics Letters **95** (2009) 162110.
- [56] Poudel, B., *et al.*, *High-thermoelectric performance of nanostructured bismuth antimony telluride bulk alloys*, Science **320** (2008) 634.
- [57] Gregori, G., S. Heinze, P. Lupetin, H.-U. Habermeier, and J. Maier, *Seebeck coefficient and electrical conductivity of mesoscopic nanocrystalline $SrTiO_3$* , Journal of Materials Science, *submitted*.
- [58] Vollman, M. and R. Waser, *Grain-Boundary Defect Chemistry of Acceptor-Doped Titanates - Space-Charge Layer Width*, Journal of the American Ceramic Society **77** (1994) 235.
- [59] Waser, R., *Electronic properties of grain boundaries in $SrTiO_3$ and $BaTiO_3$ ceramics*, Solid State Ionics **75** (1995) 89.
- [60] Denk, I., J. Claus, and J. Maier, *Electrochemical investigations of $SrTiO_3$ boundaries*, Journal of the Electrochemical Society **144** (1997) 3526.
- [61] Hagenbeck, R. and R. Waser, *Influence of temperature and interface charge on the grain-boundary conductivity in acceptor-doped $SrTiO_3$ ceramics*, Journal of Applied Physics **83** (1998) 2083.
- [62] McIntyre, P.C., *Equilibrium point defect and electronic carrier distributions near interfaces in acceptor-doped strontium titanate*, Journal of the American Ceramic Society **83** (2000) 1129.
- [63] Fleig, J., S. Rodewald, and J. Maier, *Microcontact impedance measurements of individual highly resistive grain boundaries: General aspects and application to acceptor-doped $SrTiO_3$* , Journal of Applied Physics **87** (2000) 2372.

- [64] Rodewald, S., J. Fleig, and J. Maier, *Microcontact impedance spectroscopy at single grain boundaries in Fe-doped SrTiO₃ polycrystals*, Journal of the American Ceramic Society **84** (2001) 521.
- [65] Guo, X., J. Fleig, and J. Maier, *Determination of electronic and ionic partial conductivities of a grain boundary: method and application to acceptor-doped SrTiO₃*, Solid State Ionics **154** (2002) 563.
- [66] De Souza, R.A., *et al.*, *Electrical and structural characterization of a low-angle tilt grain boundary in iron-doped strontium titanate*, Journal of the American Ceramic Society **86** (2003) 922.
- [67] De Souza, R.A. and J. Maier, *Capacitance of single crystal and low-angle tilt bicrystals of Fe-doped SrTiO₃*, Faraday Discussions **134** (2007) 235.
- [68] De Souza, R.A., *The formation of equilibrium space-charge zones at grain boundaries in the perovskite oxide SrTiO₃*, Physical Chemistry Chemical Physics **11** (2009) 9939.
- [69] Browning, N.D., *et al.*, *The influence of atomic structure on the formation of electrical barriers at grain boundaries in SrTiO₃*, Applied Physics Letters **74** (1999) 2638.
- [70] Jia, C.L. and K. Urban, *Atomic-resolution measurement of oxygen concentration in oxide materials*, Science **303** (2004) 2001.
- [71] von Alfthan, S., *et al.*, *The Structure of Grain Boundaries in Strontium Titanate: Theory, Simulation, and Electron Microscopy*, in *Annual Review Of Materials Research, Vol 40*, p. 557.
- [72] Chiang, Y.M. and T. Takagi, *Grain-Boundary Chemistry of Barium-Titanate and Strontium-Titanate .1. High-Temperature Equilibrium Space-Charge*, Journal of the American Ceramic Society **73** (1990) 3278.
- [73] Balaya, P., J. Jamnik, J. Fleig, and J. Maier, *Mesosopic electrical conduction in nanocrystalline SrTiO₃*, Applied Physics Letters **88** (2006) 062109.
- [74] Balaya, P., *et al.*, *Synthesis and characterization of nanocrystalline SrTiO₃*, Journal of the American Ceramic Society **89** (2006) 2804.
- [75] Balaya, P., J. Jamnik, J. Fleig, and J. Maier, *Mesosopic hole conduction in nanocrystalline SrTiO₃ - A detailed analysis by impedance spectroscopy*, Journal of the Electrochemical Society **154** (2007) P69.
- [76] Maier, J., *Kröger-Vink diagrams for boundary regions*, Solid State Ionics **32-3** (1989) 727.
- [77] Kingery, W.D., H.K. Bowen, and D.R. Uhlmann, *Introduction to ceramics, 2nd edition*. 1976.
- [78] Karczewski, J., B. Riegel, M. Gazda, P. Jasinski, and B. Kusz, *Electrical and structural properties of Nb-doped SrTiO₃ ceramics*, Journal of Electroceramics **24** 326.
- [79] Petrov, P.K., Z.G. Ivanov, and S.S. Gevorgyan, *X-ray study of SrTiO₃ thin films in multilayer structures*, Materials Science and Engineering A-Structural Materials Properties Microstructure And Processing **288** (2000) 231.

- [80] Scheel, H.J., *Crystal-Growth and Characterization of SrTiO₃*, Zeitschrift für Kristallographie **143** (1976) 417.
- [81] Moos, R. and K.H. Härdtl, *Electronic transport properties of Sr_{1-x}La_xTiO₃ ceramics*, Journal of Applied Physics **80** (1996) 393.
- [82] Blennow, P., A. Hagen, K.K. Hansen, L.R. Wallenberg, and M. Mogensen, *Defect and electrical transport properties of Nb-doped SrTiO₃*, Solid State Ionics **179** (2008) 2047.
- [83] Shannon, R.D., *Revised Effective Ionic-Radii And Systematic Studies Of Interatomic Distances in Halides And Chalcogenides*, Acta Crystallographica Section A **32** (1976) 751.
- [84] Daniels, J., K.H. Härdtl, D. Hennings, and R. Wernicke, *Defect Chemistry And Electrical-Conductivity of Doped Barium-Titanate Ceramics*, Philips Research Reports **31** (1976) 487.
- [85] Chan, N.H., R.K. Sharma, and D.M. Smyth, *Nonstoichiometry in Undoped BaTiO₃*, Journal of the American Ceramic Society **64** (1981) 556.
- [86] Chan, N.H. and D.M. Smyth, *Defect chemistry of donor-doped BaTiO₃*, Journal of the American Ceramic Society **67** (1984) 285.
- [87] Chan, H.M., M.P. Harmer, and D.M. Smyth, *Compensating defects in highly donor-doped BaTiO₃*, Journal of the American Ceramic Society **69** (1986) 507.
- [88] Choi, G.M., H.L. Tuller, and D. Goldschmidt, *Electronic-Transport Behavior In Single-Crystalline Ba_{0.03}Sr_{0.97}TiO₃*, Physical Review B **34** (1986) 6972.
- [89] Choi, G.M. and H.L. Tuller, *Defect Structure and Electrical-Properties of Single-Crystal Ba_{0.03}Sr_{0.97}TiO₃*, Journal of the American Ceramic Society **71** (1988) 201.
- [90] Chiang, Y.M. and T. Takagi, *Grain-Boundary Chemistry of Barium-Titanate and Strontium-Titanate. 2. Origin of Electrical Barriers in Positive-Temperature-Coefficient Thermistors*, Journal of the American Ceramic Society **73** (1990) 3286.
- [91] Smyth, D.M., *The Defect Chemistry of Donor-Doped BaTiO₃: A Rebuttal*, Journal of Electroceramics **9** (2002) 179.
- [92] Hoffmann-Eifert, S., *Point defects - disorder, thermodynamics and kinetics*, in *Lecture Notes of the 41st Spring School 2010*, Schriften des FZ Jülich.
- [93] Waser, R., T. Bieger, and J. Maier, *Determination of acceptor concentrations and energy levels in oxides using an optoelectrochemical technique*, Solid State Communications **76** (1990) 1077.
- [94] Guo, X. and J. Maier, *On the Hebb-Wagner polarisation of SrTiO₃ doped with redox-active ions*, Solid State Ionics **130** (2000) 267.
- [95] Merkle, R. and J. Maier, *Defect association in acceptor-doped SrTiO₃: case study for Fe'_{Ti} -V_O²⁺ and Mn''_{Ti}-V_O²⁺* Physical Chemistry Chemical Physics **5** (2003) 2297.
- [96] Merkle, R. and J. Maier, *How is oxygen incorporated into oxides? A comprehensive kinetic study of a simple solid-state reaction with SrTiO₃ as a model material*, Angewandte Chemie-International Edition **47** (2008) 3874.

- [97] Lenser, C., *et al.*, *Spectroscopic study of the electric field induced valence change of Fe-defect centers in SrTiO₃*, *Physical Chemistry Chemical Physics* **13** (2011) 20779.
- [98] Daniels, J., *Defect Chemistry and Electrical-Conductivity of Doped Barium-Titanate Ceramics: 2. Defect Equilibria in Acceptor-Doped Barium-Titanate*, *Philips Research Reports* **31** (1976) 505.
- [99] Tuller, H.L., *Mixed conduction in nonstoichiometric oxides*, in *Nonstoichiometric oxides*, O. Toft Soerensen, Editor 1981, Academic Press, p. 271.
- [100] Daniels, J. and K.H. Härdtl, *Defect Chemistry And Electrical-Conductivity of Doped Barium-Titanate Ceramic: 1. Electrical-Conductivity at High-Temperatures of Donor-Doped Barium-Titanate Ceramics*, *Philips Research Reports* **31** (1976) 489.
- [101] Balachandran, U. and N.G. Eror, *Electrical Conductivity in Lanthanum-Doped Strontium-Titanate*, *Journal of the Electrochemical Society* **129** (1982) 1021.
- [102] Blennow, P., K.K. Hansen, L.R. Wallenberg, and M. Mogensen, *Electrochemical characterization and redox behavior of Nb-doped SrTiO₃*, *Solid State Ionics* **180** (2009) 63.
- [103] Maier, J., *Complex oxides: high temperature defect chemistry vs. low temperature defect chemistry*, *Physical Chemistry Chemical Physics* **5** (2003) 2164.
- [104] Maier, J., *Defect chemistry and conductivity effects in heterogeneous solid electrolytes* *Journal of the Electrochemical Society* **134** (1987) 1524.
- [105] Waser, R. and R. Hagenbeck, *Grain boundaries in dielectric and mixed conducting ceramics*, *Acta Materialia* **48** (2000) 797.
- [106] Guo, X. and R. Waser, *Electrical properties of the grain boundaries of oxygen ion conductors: Acceptor-doped zirconia and ceria*, *Progress In Materials Science* **51** (2006) 151.
- [107] Tuller, H.L., S.J. Litzelman, and W. Jung, *Micro-ionics: next generation power sources*, *Physical Chemistry Chemical Physics* **11** (2009) 3023.
- [108] Ikuhara, Y., P. Thavorniti, and T. Sakuma, *Solute segregation at grain boundaries in superplastic SiO₂-doped TZP*, *Acta Materialia* **45** (1997) 5275.
- [109] Wang, Z.C., *et al.*, *Atom-resolved imaging of ordered defect superstructures at individual grain boundaries*, *Nature* **479** (2011) 380.
- [110] Mott, N.F., *The theory of crystal rectifiers*, *Proceedings of The Royal Society of London Series A-Mathematical and Physical Sciences* **171** (1939) 27.
- [111] Schottky, W., *Zur Halbleitertheorie der Sperrschicht- und Spitzengleichrichter*, *Zeitschrift für Physik A Hadrons and Nuclei* **113** (1939) 367.
- [112] Vandijk, T. and A.J. Burggraaf, *Grain-Boundary Effects On Ionic-Conductivity In Ceramic Gd_xZr_{1-x}O_{2-(x-2)} Solid-Solutions*, *Physica Status Solidi A-Applied Research* **63** (1981) 229.

- [113] Fleig, J. and J. Maier, *The impedance of ceramics with highly resistive grain boundaries: Validity and limits of the brick layer model*, Journal of the European Ceramic Society **19** (1999) 693.
- [114] Abrantes, J.C.C., J.A. Labrincha, and J.R. Frade, *Applicability of the brick layer model to describe the grain boundary properties of strontium titanate ceramics*, Journal of the European Ceramic Society **20** (2000) 1603.
- [115] Guo, X. and J. Maier, *Grain boundary blocking effect in zirconia: A Schottky barrier analysis*, Journal of the Electrochemical Society **148** (2001) E121.
- [116] Frey, M.H. and D.A. Payne, *Synthesis and processing of barium titanate ceramics from alkoxide solutions and monolithic gels*, Chemistry of Materials **7** (1995) 123.
- [117] Beck, C., W. Hartl, and R. Hempelmann, *Size-controlled synthesis of nanocrystalline BaTiO₃ by a sol-gel type hydrolysis in microemulsion-provided nanoreactors*, Journal of Materials Research **13** (1998) 3174.
- [118] Pechini, M.P., *Method of Preparing Lead and Alkaline Earth Titanates and Niobates and Coatings Using the Same to Form Capacitor*, U.S. Patent No.3330697 (1967).
- [119] Kakihana, M., *Invited review "sol-gel" preparation of high temperature superconducting oxides*, Journal of Sol-Gel Science and Technology **6** (1996) 7.
- [120] Poth, J., R. Haberkorn, and H.P. Beck, *Combustion-synthesis of SrTiO₃ - Part I. Synthesis and properties of the ignition products*, Journal of the European Ceramic Society **20** (2000) 707.
- [121] Chen, D.R., X.L. Jiao, and M.S. Zhang, *Hydrothermal synthesis of strontium titanate powders with nanometer size derived from different precursors*, Journal of the European Ceramic Society **20** (2000) 1261.
- [122] Ciftci, E., M.N. Rahaman, and M. Shumsky, *Hydrothermal precipitation and characterization of nanocrystalline BaTiO₃ particles*, Journal of Materials Science **36** (2001) 4875.
- [123] Buscaglia, M.T., M. Bassoli, and V. Buscaglia, *Solid-state synthesis of ultrafine BaTiO₃ powders from nanocrystalline BaCO₃ and TiO₂*, Journal of the American Ceramic Society **88** (2005) 2374.
- [124] Bilecka, I., I. Djerdj, and M. Niederberger, *One-minute synthesis of crystalline binary and ternary metal oxide nanoparticles*, Chemical Communications (2008) 886.
- [125] Niederberger, M., G. Garnweitner, N. Pinna, and M. Antonietti, *Nonaqueous and halide-free route to Crystalline BaTiO₃, SrTiO₃, and (Ba,Sr)TiO₃ nanoparticles via a mechanism involving C-C bond formation*, Journal of the American Chemical Society **126** (2004) 9120.
- [126] Anselmi-Tamburini, U., *et al.*, *Spark plasma sintering and characterization of bulk nanostructured fully stabilized zirconia: Part I. Densification studies*, Journal of Materials Research **19** (2004) 3255.
- [127] Anselmi-Tamburini, U., *et al.*, *Spark plasma sintering and characterization of bulk nanostructured fully stabilized zirconia: Part II. Characterization studies*, Journal of Materials Research **19** (2004) 3263.

- [128] Munir, Z.A., U. Anselmi-Tamburini, and M. Ohyanagi, *The effect of electric field and pressure on the synthesis and consolidation of materials: A review of the spark plasma sintering method*, Journal of Materials Science **41** (2006) 763.
- [129] Chaim, R., M. Levin, A. Shlayer, and C. Estournes, *Sintering and densification of nanocrystalline ceramic oxide powders: a review*, Advances in Applied Ceramics **107** (2008) 159.
- [130] Lu, K., *Sintering of nanoceramics*, International Materials Reviews **53** (2008) 21.
- [131] Orrù, R., R. Licheri, A.M. Locci, A. Cincotti, and G. Cao, *Consolidation/synthesis of materials by electric current activated/assisted sintering*, Materials Science and Engineering: Reports **63** (2009) 127.
- [132] Garay, J.E., *Current-Activated, Pressure-Assisted Densification of Materials*, in *Annual Review Of Materials Research, Vol 40*. p. 445.
- [133] Hulbert, D.M., *et al.*, *The absence of plasma in "spark plasma sintering"*, Journal of Applied Physics **104** (2008).
- [134] Xie, G.Q., O. Ohashi, M.H. Song, K. Mitsuishi, and K. Furuya, *Reduction mechanism of surface oxide films and characterization of formations on pulse electric-current sintered Al-Mg alloy powders*, Applied Surface Science **241** (2005) 102.
- [135] Hennicke, J. and H.U. Kessel, *Field assisted sintering technology ("FAST"), for the consolidation of innovative materials*, Cfi-Ceramic Forum International **81** (2004) E14.
- [136] Chen, W., U. Anselmi-Tamburini, J.E. Garay, J.R. Groza, and Z.A. Munir, *Fundamental investigations on the spark plasma sintering/synthesis process - I. Effect of dc pulsing on reactivity*, Materials Science and Engineering A-Structural Materials Properties Microstructure and Processing **394** (2005) 132.
- [137] Anselmi-Tamburini, U., S. Gennari, J.E. Garay, and Z.A. Munir, *Fundamental investigations on the spark plasma sintering/synthesis process - II. Modeling of current and temperature distributions*, Materials Science and Engineering A-Structural Materials Properties Microstructure and Processing **394** (2005) 139.
- [138] Anselmi-Tamburini, U., J.E. Garay, and Z.A. Munir, *Fundamental investigations on the spark plasma sintering/synthesis process III. Current effect on reactivity*, Materials Science and Engineering A-Structural Materials Properties Microstructure and Processing **407** (2005) 24.
- [139] Ho, P.S. and T. Kwok, *Electromigration In Metals*, Reports On Progress In Physics **52** (1989) 301.
- [140] Yasunaga, H. and A. Natori, *Electromigration On Semiconductor Surfaces*, Surface Science Reports **15** (1992) 205.
- [141] Garay, J.E., U. Anselmi-Tamburini, and Z.A. Munir, *Enhanced growth of intermetallic phases in the Ni-Ti system by current effects*, Acta Materialia **51** (2003) 4487.
- [142] Garay, J.E., S.C. Glade, U. Anselmi-Tamburini, P. Asoka-Kumar, and Z.A. Munir, *Electric current enhanced defect mobility in Ni₃Ti intermetallics*, Applied Physics Letters **85** (2004) 573.

- [143] Zhao, J., J.E. Garay, U. Anselmi-Tamburini, and Z.A. Munir, *Directional electromigration-enhanced interdiffusion in the Cu-Ni system*, Journal of Applied Physics **102** (2007).
- [144] Olevsky, E.A., S. Kandukuri, and L. Froyen, *Consolidation enhancement in spark-plasma sintering: Impact of high heating rates*, Journal Of Applied Physics **102** (2007).
- [145] Anselmi-Tamburini, U., J.E. Garay, and Z.A. Munir, *Fast low-temperature consolidation of bulk nanometric ceramic materials*, Scripta Materialia **54** (2006) 823.
- [146] Macdonald, J.R., *Impedance Spectroscopy: Theory, Experiment, and Applications, Second Edition*. 2005, John Wiley & Sons, Inc.
- [147] Bauerle, J.E., *Study of Solid Electrolyte Polarization by a Complex Admittance Method*, Journal of Physics and Chemistry of Solids **30** (1969) 2657.
- [148] Hodge, I.M., M.D. Ingram, and A.R. West, *A new method for analysing the a.c. behaviour of polycrystalline solid electrolytes*, Journal of Electroanalytical Chemistry and Interfacial Electrochemistry **58** (1975) 429.
- [149] Hodge, I.M., M.D. Ingram, and A.R. West, *Impedance and modulus spectroscopy of polycrystalline solid electrolytes*, Journal of Electroanalytical Chemistry and Interfacial Electrochemistry **74** (1976) 125.
- [150] Fleig, J., *The grain boundary impedance of random microstructures: numerical simulations and implications for the analysis of experimental data*, Solid State Ionics **150** (2002) 181.
- [151] Abrantes, J.C.C., J.A. Labrincha, and J.R. Frade, *Representations of impedance spectra of ceramics - Part I. Simulated study cases*, Materials Research Bulletin **35** (2000) 955.
- [152] Abrantes, J.C.C., J.A. Labrincha, and J.R. Frade, *Representations of impedance spectra of ceramics - Part II. Spectra of polycrystalline SrTiO₃*, Materials Research Bulletin **35** (2000) 965.
- [153] Larson, A. and R.B. Von Dreele, *GSAS - General structure analysis system*, Los Alamos National Laboratory Report LAUR 86-748, (1986) see also (<http://www.ncnr.nist.gov/xtal/software/gsas.html>).
- [154] Ankudinov, A.L., B. Ravel, J.J. Rehr, and S.D. Conradson, *Real-space multiple-scattering calculation and interpretation of x-ray-absorption near-edge structure*, Physical Review B **58** (1998) 7565.
- [155] Klementev, K.V., *Extraction of the fine structure from x-ray absorption spectra*, Journal of Physics D-Applied Physics **34** (2001) 209.
- [156] Hennings, D.F.K., C. Metzmaier, and B.S. Schreinemacher, *Defect Chemistry and Microstructure of Hydrothermal Barium Titanate*, Journal of the American Ceramic Society **84** (2001) 179.
- [157] Cho, W.-S. and E. Hamada, *Synthesis of ultrafine BaTiO₃ particles from polymeric precursor: their structure and surface property*, Journal of Alloys and Compounds **266** (1998) 118.

- [158] Vinothini, V., P. Singh, and M. Balasubramanian, *Synthesis of barium titanate nanopowder using polymeric precursor method*, *Ceramics International* **32** (2006) 99.
- [159] Lazarevic, Z.Z., *et al.*, *The characterization of the barium titanate ceramic powders prepared by the Pechini type reaction route and mechanically assisted synthesis*, *Journal of the European Ceramic Society* **30** 623.
- [160] Pinna, N. and M. Niederberger, *Surfactant-free nonaqueous synthesis of metal oxide nanostructures*, *Angewandte Chemie-International Edition* **47** (2008) 5292.
- [161] Lupetin, P., G. Gregori, and J. Maier, *Mesoscopic Charge Carriers Chemistry in Nanocrystalline SrTiO₃*, *Angewandte Chemie International Edition* **49** (2010) 10123.
- [162] Jurado, J.R., M.T. Colomer, and J.R. Frade, *Electrical characterization of Sr_{0.97}Ti_{1-x}Fe_xO_{3-δ} by complex impedance spectroscopy: I, materials with low iron contents*, *Journal of the American Ceramic Society* **83** (2000) 2715.
- [163] Zhang, Z.L., *et al.*, *Comparative studies of microstructure and impedance of small-angle symmetrical and asymmetrical grain boundaries in SrTiO₃*, *Acta Materialia* **53** (2005) 5007.
- [164] Kotomin, E.A., V. Alexandrov, D. Gryaznov, R.A. Evarestov, and J. Maier, *Confinement effects for ionic carriers in SrTiO₃ ultrathin films: first-principles calculations of oxygen vacancies*, *Physical Chemistry Chemical Physics* **13** 923.
- [165] Subbarao, E.C. and H.S. Maiti, *Solid Electrolytes With Oxygen Ion Conduction*, *Solid State Ionics* **11** (1984) 317.
- [166] Gregori, G., P. Lupetin, and J. Maier, *Variations of the grain boundary core charge density in nanocrystalline SrTiO₃*, in preparation (2012).
- [167] Schneider-Störmann, L., M. Vollmann, and R. Waser, *Grain-boundary decorated titanate ceramics: Preparation and processing*, *Solid State Ionics* **75** (1995) 123.
- [168] Avila-Paredes, H.J. and S. Kim, *The effect of segregated transition metal ions on the grain boundary resistivity of gadolinium doped ceria: Alteration of the space charge potential*, *Solid State Ionics* **177** (2006) 3075.
- [169] Gregori, G., B. Rahmati, W. Sigle, P.A. van Aken, and J. Maier, *Electric conduction properties of boron-doped ceria*, *Solid State Ionics* **192** (2011) 65.
- [170] Litzelman, S.J., *et al.*, *Heterogeneously doped nanocrystalline ceria films by grain boundary diffusion: Impact on transport properties*, *Journal of Electroceramics* **22** (2009) 405.
- [171] Jurado, J.R., M.T. Colomer, and J.R. Frade, *Impedance spectroscopy of Sr_{0.97}Ti_{1-x}Fe_xO_{3-δ} materials with moderate Fe-contents*, *Solid State Ionics* **143** (2001) 251.
- [172] Guo, X., W. Sigle, and J. Maier, *Blocking grain boundaries in yttria-doped and undoped ceria ceramics of high purity*, *Journal of the American Ceramic Society* **86** (2003) 77.

- [173] Liao, P.L., M.C. Toroker, and E.A. Carter, *Electron Transport in Pure and Doped Hematite*, Nano Letters **11** (2011) 1775.
- [174] Warnes, B.M., F.F. Aplan, and G. Simkovich, *Electrical conductivity and seebeck voltage of Fe₂O₃, pure and doped, as a function of temperature and oxygen pressure*, Solid State Ionics **12** (1984) 271.
- [175] Lupetin, P., *et al.*, *Nanocrystalline acceptor-doped SrTiO₃. Part I: synthesis and microstructural characterization*, in preparation (2012).
- [176] Lupetin, P., G. Gregori, and J. Maier, *Nanocrystalline acceptor-doped SrTiO₃. Part II: characterization of the electrical properties*, in preparation (2012).
- [177] Ruiz-Morales, J.C., *et al.*, *Disruption of extended defects in solid oxide fuel cell anodes for methane oxidation*, Nature **439** (2006) 568.
- [178] Fu, Q.X., F. Tietz, D. Sebold, S.W. Tao, and J.T.S. Irvine, *An efficient ceramic-based anode for solid oxide fuel cells*, Journal of Power Sources **171** (2007) 663.
- [179] Ma, Q., F. Tietz, A. Leonide, and E. Ivers-Tiffée, *Electrochemical performances of solid oxide fuel cells based on Y-substituted SrTiO₃ ceramic anode materials*, Journal of Power Sources **196** (2011) 7308.
- [180] Ma, Q.L., F. Tietz, and D. Stover, *Nonstoichiometric Y-substituted SrTiO₃ materials as anodes for solid oxide fuel cells*, Solid State Ionics **192** (2011) 535.
- [181] Smith, B.H., W.C. Holler, and M.D. Gross, *Electrical properties and redox stability of tantalum-doped strontium titanate for SOFC anodes*, Solid State Ionics **192** (2011) 383.
- [182] Fu, Q.X., S.B. Mi, E. Wessel, and F. Tietz, *Influence of sintering conditions on microstructure and electrical conductivity of yttrium-substituted SrTiO₃*, Journal of the European Ceramic Society **28** (2008) 811.
- [183] Heywang, W., *Bariumtitanat als Sperrschichtbleiter*, Solid-State Electronics **3** (1961) 51.
- [184] Michenaud, J.P. and C. Gillot, *About the interpretation of the PTC effect in Nb-doped BaTiO₃ ceramics*, Ferroelectrics **127** (1992) 41.
- [185] Preis, W., A. Bürgermeister, W. Sitte, and P. Supancic, *Bulk and grain boundary resistivities of donor-doped barium titanate ceramics*, Solid State Ionics **173** (2004) 69.
- [186] Preis, W. and W. Sitte, *Electronic conductivity and chemical diffusion in n-conducting barium titanate ceramics at high temperatures*, Solid State Ionics **177** (2006) 3093.
- [187] Preis, W. and W. Sitte, *Modelling of grain boundary resistivities of n-conducting BaTiO₃ ceramics*, Solid State Ionics **177** (2006) 2549.
- [188] Preis, W. and W. Sitte, *Modeling of transport properties of interfacially controlled electroceramics: Application to n-conducting barium titanate*, Journal of Electroceramics **27** (2011) 83.
- [189] Hou, J.B., Z.L. Zhang, W. Preis, W. Sitte, and G. Dehm, *Electrical properties and structure of grain boundaries in n-conducting BaTiO₃ ceramics*, Journal of the European Ceramic Society **31** (2011) 763.

- [190] Frömmling, T., *et al.*, *Oxygen tracer diffusion in donor doped barium titanate*, Journal of Applied Physics **110** (2011).
- [191] Frömmling, T., A. Schintlmeister, H. Hutter, and J. Fleig, *Oxide Ion Transport in Donor-Doped $Pb(Zr_xTi_{1-x}O_3)$: The Role of Grain Boundaries*, Journal of the American Ceramic Society **94** (2011) 1173.
- [192] Horikiri, F., *et al.*, *The influence of grain boundary on the conductivity of donor doped $SrTiO_3$* , Solid State Ionics **177** (2006) 2555.
- [193] Koschek, G. and E. Kubalek, *Grain boundary characteristics and their influence on the electrical-resistance of barium titanate ceramics*, Journal of the American Ceramic Society **68** (1985) 582.
- [194] Wu, T.-B. and J.-N. Lin, *Transition of Compensating Defect Mode in Niobium-Doped Barium Titanate*, Journal of the American Ceramic Society **77** (1994) 759.
- [195] Abrantes, J.C.C., A. Feighery, A.A.L. Ferreira, J.A. Labrincha, and J.R. Frade, *Impedance spectroscopy study of niobium-doped strontium titanate ceramics*, Journal Of The American Ceramic Society **85** (2002) 2745.
- [196] Lupetin, P., G. Gregori, and J. Maier, *Defect chemistry of nanocrystalline donor doped $SrTiO_3$* , in preparation (2012).
- [197] Steele, B.C.H., *Appraisal of $Ce_{1-y}Gd_yO_{2-y/2}$ electrolytes for IT-SOFC operation at 500°C*, Solid State Ionics **129** (2000) 95.
- [198] Tuller, H.L. and A.S. Nowick, *Defect Structure and Electrical-Properties of Nonstoichiometric CeO_2 Single-Crystals*, Journal of the Electrochemical Society **126** (1979) 209.
- [199] Mogensen, M., N.M. Sammes, and G.A. Tompsett, *Physical, chemical and electrochemical properties of pure and doped ceria*, Solid State Ionics **129** (2000) 63.
- [200] Lupetin, P., F. Giannici, G. Gregori, A. Martorana, and J. Maier, *Effect of grain boundary decoration on the electrical conduction of nanocrystalline CeO_2* , Journal of the Electrochemical Society **159** (2012) B417.
- [201] Wang, D.Y., D.S. Park, J. Griffith, and A.S. Nowick, *Oxygen-ion conductivity and defect interactions in yttria-doped ceria*, Solid State Ionics **2** (1981) 95.
- [202] Eguchi, K., T. Setoguchi, T. Inoue, and H. Arai, *Electrical-properties of ceria-based oxides and their application to solid oxide fuel-cells*, Solid State Ionics **52** (1992) 165.
- [203] Dikmen, S., P. Shuk, and M. Greenblatt, *Hydrothermal synthesis and properties of $Ce_{1-x}Bi_xO_{2-\delta}$ solid solutions*, Solid State Ionics **112** (1998) 299.

Acknowledgements

First of all, I express my deep gratitude to Professor Joachim Maier for having given me the possibility of doing my Ph.D. in his department. Working at such high level was for me extremely motivating and encouraged me to improve myself day by day and to give my best in all occasions. His suggestions and our discussions improved enormously the quality of this dissertation. All I learnt from him in the past three and half years is something that I will never forget and that will be fundamental for my future.

I would like to thank Prof. Joachim Bill and Prof. Emil Roduner for having accepted of being part of my Ph.D. exam committee.

As Ph.D. it was a pleasure to be supervised by Giuliano Gregori. To him I am indebted grateful for having believed in me and in my attitude from the first moment we met. Our daily discussions, his suggestions, his constant support were simply invaluable. His guidance as well as his ability to make me feel the right person in the right place is something that made my time at Max Planck Institute special.

I sincerely appreciated all the people who gave a contribution to make this work possible. I want to thank: Dr. Rotraut Merkle for the precious advices in many occasions; Prof. Palami Balaya (National University of Singapore) and Prof. Markus Niederberger (ETH Zürich) for the precious advices on the powder synthesis; Gabi Götz for thousands of XRD measurements; Dr. Francesco Giannici (University of Palermo) for the support in the EXAFS experiments and the relative data analysis; Dr. Benhaz Rahmati (MPI-IS) for TEM investigations; Dr. Mitsuharu Konuma for the acquisition of XPS spectra. Annette Fuchs, Uwe Traub, Udo Klock and Peter Senk are

thanked for their technical support. A special thank goes to Sofia Weiglein for her precious help.

I express my gratitude to my colleagues Dr. Mona Shirpour, Marcus Göbel and Kiran Adepalli for our fruitful discussions, which helped me to understand and solve many problems.

With my dear friends Alice, Federico, Elisa and Piero I shared not only my working time, but also my daily life with its ups and downs and all that this means. To them I just say: “Grazie di cuore”. I will never forget the time spent together.

To my beloved parents I am indebted grateful for their constant support, for having encouraged me to give my best in any occasion, for how they made me feel at home even if I was and I will be far from them. To them I dedicate this thesis, aware that without them nothing would have ever been possible.

Curriculum vitae

Name	Piero Lupetin
Date of birth	25.02.1983
Place of birth	Trieste, Italy
September 2008 –May 2012	Ph.D. Max Planck Institute for Solid State Research, Stuttgart, Germany Department of Prof. Dr. Joachim Maier, Title of the final dissertation: <i>“Charge carrier defect chemistry of nanoscopic SrTiO₃.”</i>
July 2008	Qualification exam for the Italian Board of Engineers
October 2005 – March 2008	M. Sc. in Materials Engineering University of Trieste, Italy Title of the final thesis: <i>“Critical analysis of the methods for the determination of the fracture toughness in Zirconia-based ceramics.”</i>
September 2002 – October 2005	B. Sc. in Materials Engineering University of Trieste, Italy Title of the final thesis: <i>“Piezospectroscopic study of thermal barrier coatings.”</i>
July 2002	High school diploma Liceo scientifico statale “G. Galilei”, Trieste, Italy